STUDYING EFFECTS OF ADHESIVE LAYER ON ELECTRICAL SIGNALS OF PIEZOELECTRIC TRANSDUCER BONDED WITH STRUCTURE

By

MD MAZHARUL ISLAM

Presented to the Faculty of the Graduate School of the University of Texas at Arlington in Partial Fulfillment of the Requirements for the Degree of

DOCTOR OF PHILOSOPHY

THE UNIVERSITY OF TEXAS AT ARLINGTON

May 2017

Partial of this work (Islam and Huang 2014, and Islam and Huang 2016) has been published in smart materials and structures under the Institute of Physics (IOP) publishing, which is available online. The work is republished here under the license agreement between Md Mazharul Islam and IOP publishing, provide by the copyright clearance center. The license numbers of the republished articles (Islam and Huang 2014), and (Islam and Huang 2016) are 4115930509594, and 4115930660522, respectively.

ACKNOWLEDGEMENTS

I am grateful to Almighty God for giving me the opportunity to finish my Ph.D. I am also thankful to Prof. Haiying Huang for her guidance to improve my research and writing skills. I would like to express my sincere gratitude to Prof. Haiying Huang for her financial support during my Ph.D. study.

Besides my advisors, I would like to thank the rest of my dissertation committee members: Prof. Kent Lawrence, Prof. Wen Chen, Prof. Bo P Wang, and Prof. Ashfaq Adnan, for their interests in my research.

I would like to thank my colleagues, Irshad Mohammad, Xiang Xu, and Farshad Zahedi, for their warming presences in the lab. I also thank my friend, Arif Iftakher, for mentoring me on electrical networks.

I would like to thank my manager at FIAT Chrysler LLC, Ken Singh, Group Lead, Jim Chen, and Tech lead, Wensheng Zhang, for letting me take vacations until I finish my dissertation. I also thank my colleague, Imran Hossain, for taking care of my projects during my vacations.

I would like to thank my maternal uncle, Mustafa Kamal Mollah, and his family for their generous support during my undergraduate entrance exam preparation. Without their supports, I might not be able to reach to the situation where I am today.

I would like to express my deepest gratitude to my beloved wife, Kamrun Naher Sumi, for her sacrifices and cooperation during my Ph.D. I also thank my daughter, Wasfia Mazhar Manha, for being a constant source of joy.

Finally, I would like to express my heartiest gratitude to my parents who inspired me to pursue Ph.D. I also thank all of my friends who have helped me throughout my career.

May, 2017

ABSTRACT

STUDYING EFFECTS OF ADHESIVE LAYER ON ELECTRICAL SIGNALS OF PIEZOELECTRIC TRANSDUCER BONDED WITH STRUCTURE

MD MAZHARUL ISLAM, Ph.D.

The University of Texas at Arlington, 2017

Supervising Professor: Dr. Haiying Huang

Piezoelectric wafer active sensors (PWAS) are the most attractive transducers for guided-wave or ultrasound based structural health monitoring (SHM) because of their light weight and compact size. In order to excite guided waves in a structure, the PWASs are usually bonded on the surface of the structure by adhesive materials. The electrical signal applied to the surface bonded PWAS is converted to mechanical deformation of the PWAS which in turn is transferred to the structure through the adhesive layer. Thus, understanding the effects of the adhesive layer on the electrical response of the PWAS enables us to optimize the mechanical coupling between the PWAS and the structure. The preliminary study of the adhesive layer effects using experiments revealed that the electrical signal of the PWAS is significantly influenced by the adhesive layer thickness. However, comprehensive understanding of the adhesive layer effects on the PWAS signals is not feasible through experiments because conducting parametric studies

experimentally are impractical. Therefore, studying the adhesive layer effects on the PWAS signals using Finite Element (FE) method has brought immense attentions to the researchers. However, FE based modeling is computationally very expensive as well as inaccurate especially at high frequency. Thus, FE based adhesive layer study is not feasible as well because PWAS based SHM techniques involve high frequency analysis. Even though researchers have developed analytical models for adhesive layer studies, detailed investigations of adhesive layer effects on the PWAS response is still not available in the literature due to the lack of an appropriate model that can completely capture the coupled electromechanical physics associated with the PWAS and the structure. Moreover, most of the available analytical models ignored the adhesive layer; a few of them that included a physics-based model to represent adhesive layer failed to demonstrate how the adhesive layer parameters, e.g. shear modulus, thickness etc. affect the PWAS signals; the majority of them considered either longitudinal mode or flexural mode of the structure. Therefore, an analytical model is sought that will incorporate a physics based adhesive layer model as well as all the possible vibration modes of the structure. We have established an analytical model by coupling the deformation of the PWAS with the structure through the distributed shear stress acting at the PWAS-adhesive and the adhesive-structure interfaces. To account for the loss in shear stress transfer from the PWAS-adhesive interface to the adhesive-structure interface, we have also introduced a new parameter named the shear transfer parameter. As a result, the physics-based adhesive layer model is a function of the shear transfer parameter, adhesive layer thickness, and shear modulus. The deformation of the structure includes both the longitudinal and the flexural vibration modes whereas only the longitudinal vibration of the PWAS is taken into account. We have established two distinct

analytical models intended for the two most popular SHM techniques: I. electromechanical impedance (EMI) based SHM (the associated model is called admittance model where a PWAS acts as both actuator and sensor); and II. guided wave (GW) based SHM (the associated model is called the pitch-catch model where a PWAS acts as an actuator and another PWAS away from the actuator acts as a sensor). In the EMI technique, the simulated admittance was matched with that of the measurement by manually adjusting the unknown adhesive layer shear modulus and thus, the unknown shear modulus of the adhesive layer was estimated through this inverse technique. On the other hand, based on the pitch-catch simulation model, an optimized adhesive thickness was predicted for a thin slender structure, and validated by measurements.

We have also studied the effects of adhesive layer degradation of lap joint structure, i.e. lap joint damage propagation on the electrical signal of PWAS bonded on the lap joint structure. Unlike other researchers who adopted amplitude change as an indication of damage, we implemented time-of-flight change as an indication of damage because the amplitude may change locally and do not show a monotonous trend with the damage propagation of lap joint structure. In this study, we combined the pulse-echo and pitch catch methods to predict, locate, and estimate the damage in lap joint structure. We used the pulse-echo signal to predict the damage propagation of the lap joint by comparing the time-of-flights between undamaged and damaged structures. Based on the pitch-catch signal, we also predicted the damage severity as well as estimate the damage length in the lap joint.

TABLE OF CONTENTS

ACKNOWLEDGEMENTS iii

ABSTRACT iv

TABLE OF CONTENTS vii

LIST OF FIGURES xi

LIST OF TABLES xvi

CHAPTER 1 INTRODUCTION 1

1.1 Literature review on EMI based SHM 1

1.2 Proposed EMI based analytical model 6

1.3 Literature review on pitch-catch based SHM 6

1.4 Proposed GW based pitch-catch analytical model 9

1.5 Combining the pitch-catch and pulse-echo methods to detect composite lap joint damage 9

1.6 Proposed S-parameters to detect severity of composite lap joint damage 12

1.7 Combining pitch-catch and pulse-echo methods to detect aluminum lap joint delamination 12

1.8 Proposed S-parameters to detect severity of aluminum lap joint delamination 16

1.9 Research goals and approaches 17

CHAPTER 2 EFFECTS OF ADHESIVE THICKNESS ON THE PWAS EMI SIGNATURE .. 19

2.1 Specimen configurations, transducer installation, and admittance measurements 19

2.2 Ultrasound mode identification 22

2.3 Multi-mode admittance analytical model of bonded PWAS 26

2.4 Analytical model validation 32

2.5 Multi-mode analytical model of bonded PWAS 32

2.5.1 Parametric studies on the adhesive effect 32

2.5.2 Matching simulated admittances with measurements 39

2.6 Conclusions 44

CHAPTER 3 EFFECTS OF ADHESIVE THICKNESS ON THE LAMB WAVE PITCH-CATCH SIGNAL USING BONDED PIEZOELECTRIC WAFER TRANSDUCER 45

3.1 Multi-mode pitch-catch analytical model 45

3.2 Parametric studies of adhesive thickness 50

3.3 Experimental Validation 55

3.4 Conclusions 61

CHAPTER 4 S-PARAMETERS FOR ULTRASOUND INSPECTION OF COMPOSITE LAP JOINTS 63

4.1 Experimentation 63

4.2 Damage detection using S21 parameter 64

4.3 Damage detection using S11 parameter 68

4.4 EMI-based damage detection 70

4.5 Conclusions 70

CHAPTER 5 DETECTING SEVERITY OF DELEMINATION IN A LAP JOINT USING S-PARAMETERS 72

5.1 Principal of operation 72

5.2 Specimen configurations 74

5.3 Time-frequency analysis of *S*-parameters 75

5.4 Detecting damage severity based on the reflection *S*-parameters 78

5.5 Detecting damage severity using the transmission S_{21} parameter 83

5.6 Conclusions 85

CHAPTER 6 CONCLUDING REMARKS 87

6.1 Effects of adhesive thickness on the EMI signature and pitch-catch signal 87

6.2 Detecting damage of a composite lap joint using S-parameters 87

6.3 Detecting severity of delamination in an aluminum lap joint using S-parameters 88

CHAPTER 7 FUTURE WORKS 89

7.1 Preliminary results 89

REFERENCES 91

APPENDIX A DERIVATION OF PULSE-ECHO AND PITCH-CATCH SIGNAL FROM S-PARAMETERS 105

LIST OF FIGURES

Figure 2.1 (a) An aluminum structure instrumented with a PWAS actuator at the center and a PWAS sensor at 100 mm from the actuator; (b) fixture for installing PWAS transducers on the structure..... 19

Figure 2.2 Impedance and admittance constituents of the PWAS actuators bonded with different bonding thicknesses; (a) real part of impedance, (b) imaginary part of impedance, (c) real part of admittance (i.e. conductance), and (d) imaginary part of admittance (i.e. susceptance). 22

Figure 2.3 Flow diagram for time-frequency analysis of broadband ultrasound pitch-catch signal. 23

Figure 2.4 (a) Broadband ultrasound pitch-catch signal acquired from specimen #2 and (b) its time-frequency representation (the amplitude is in dB scale). 24

Figure 2.5 Simulation model of a thin slender structure instrumented with a PWAS actuator; (a) dividing the instrumented specimen into piecewise homogenous sections; (b) coupling of the PWAS and structure through shear stresses at the PWAS-adhesive layer and adhesive layer-structure interfaces. 27

Figure 2.6 Comparison of group velocities between theory and simulation. 33

Figure 2.7 Effect of shear transfer constant α on the PWAS resonances when the structure undergoes longitudinal deformations; (a) & (b) admittance spectra for $\alpha = 0.01$ and $\alpha = 1.0$; (c) & (d) corresponding spectrogram; (e) relationship between resonant frequencies and α. 34

Figure 2.8 Effect of shear transfer constant α on the PWAS resonances when the structure undergoes flexural deformations; (a) & (b) admittance spectra for $\alpha = 0.01$ and $\alpha = 1.0$; (c) relationship between resonant frequencies and α. 36

Figure 2.9 Effect of shear transfer parameter α on the amplitudes of the PWAS resonances; (a) longitudinal mode; (b) flexural mode. 37

Figure 2.10 (a) & (b) Effects of h_a/G_a on PWAS admittances for longitudinal and flexural modes, respectively; (c) & (d) variations of resonant frequencies with h_a/G_a for longitudinal and flexural modes, respectively. 38

Figure 2.11 Comparisons between measured and simulated PWAS conductance and susceptance; (a & b) specimen #1, (c & d) specimen #2, and (e & f) specimen #3. 41

Figure 3.1 Simulation model of a thin slender structure instrumented with two PWAS actuators and a sensor where the instrumented specimen is divided into piecewise homogenous sections. 46

Figure 3.2 (a) Coupling of the PWAS and structure through shear stresses at the PWAS-adhesive layer and adhesive layer-structure interfaces. (b) Enlarged view of an infinitesimal element associated with all the forces acting upon it. 48

Figure 3.3 Comparison between the measured and simulated pitch-catch signals at 55 kHz; (a) the longitudinal mode pitch-catch signal; and (b) the flexural mode pitch-catch signal. 52

Figure 3.4 Effects of the adhesive thickness on the simulated pitch-catch signals; (a) amplitude-frequency relationship – longitudinal mode; (b) amplitude-frequency relationship – flexural mode; (c) change of resonance amplitude with adhesive thickness – longitudinal mode; (d) change of resonance amplitude with adhesive thickness – flexural mode; (e) change of resonance

frequency with adhesive thickness – longitudinal mode; (f) change of resonance frequency with adhesive thickness – flexural mode. 53

Figure 3.5 Effects of shear transfer parameter α on the simulated pitch-catch signal: (a) longitudinal mode; (b) flexural mode. 55

Figure 3.6 (a) A specimen instrumented with PWAS actuators and a PWAS sensor; (b) side view of the PWAS actuators bonded on the top and bottom surfaces of the structure..... 56

Figure 3.7 Effects of the adhesive thickness on the pitch-catch signal; (a) longitudinal mode-measurements, (b) flexural mode-measurement, (c) longitudinal mode-simulation, and (d) flexural mode-simulation. The shear transfer parameter and the shear modulus of the adhesive layer were adjusted to achieve better matches between the simulation and measurement..... 57

Figure 4.1 A composite lap joint instrumented with a PWAS #1 at 50 mm away from the lap joint free end and a PWAS #2 at 60 mm away from the lap joint free end; the inserted zoomed picture shows the simulated damage of the lap joint adhesive layer. 63

Figure 4.2 Comparison between the damaged and undamaged signals: (a) S21 parameters; (b) time-frequency representation of S21 parameter without damage; (c) narrowband pitch-catch signals at 300 kHz; (d) narrowband pitch-catch signals at 225 kHz..... 65

Figure 4.3 Time-frequency-amplitude plots: (a) amplitude difference between the 1 mm damaged and undamaged signals; (b) amplitude difference between the 3 mm damaged and undamaged signals. 67

Figure 4.4 (a) Comparison of S11 parameter between the damaged and undamaged lap joints and narrowband ultrasound pulse-echo responses: (b) 225 kHz; and (c) 300 kHz. 68

Figure 4.5 Comparison of admittance constituents between the damaged and undamaged lap joint composites: (a) conductance; and (b) susceptance. Comparison of narrowband pitch catch signals between the damaged and undamaged composites: (c) 225 kHz; and (d) 300 kHz. 69
Figure 5.1 Interaction between the Lamb wave and the lap joint. A part of the Lamb wave generated by PWaT #1 is reflected at the edges of the lap joint and detected by PWaT #1 as the echo signals while the other part transmits through the lap joint and is received by the PWaT #2 as the pitch-catch signal. 72
Figure 5.2 (a) Configuration of a lap joint specimen with detailed dimensions; (b) experimental set up: lap joint structure instrumented with two piezoelectric wafer active transducers; one at the left and the other at the right side of the lap joint. The transducers are connected to a vector network analyzer for simultaneous acquisition of the reflection and transmission S-parameters. 74
Figure 5.3 S-parameters of the undamaged specimen; (a) frequency-domain S_{11} parameter and time-frequency-amplitude plots of (b) S_{11}, (c) S_{22}, and (d) S_{21} parameters..... 75
Figure 5.4 Effects of delamination on the S_{11} parameters; (a) comparison of the S_{11} parameters before and after the introduction of the delamination; (b) amplitude difference of the time-domain pulse-echo signals between the undamaged specimen and the specimen with a 10 mm delamination; and (c) amplitude difference of the time-domain pulse-echo signals between the undamaged specimen and the specimen with a 15 mm delamination. 79
Figure 5.5 Time-domain pulse-echo signals extracted from the S_{11} parameter using an 8.5 cycle tone-burst signal centered at 220 kHz; (a) the pulse-echo signal contains the excitation, resonant, and echo signals; and (b) the amplitude envelopes of the time domain pulse-echo signals calculated using Hilbert-Huang transformation. 81

Figure 5.6 Effects of delamination on (a) S_{22} parameter; and (b) the amplitude envelopes of the time domain pulse-echo signals extracted from the S_{22} parameters using an 8.5 cycle 220 kHz tone-burst signal. 83

Figure 5.7 (a) Comparison of the S_{21} parameters before and after the introduction of delamination; (a) the amplitude difference of the time domain pitch-catch signal between the undamaged specimen and the specimen with a 10 mm delamination; and (c) the amplitude difference of the time domain pitch-catch signal between the undamaged specimen and the specimen with a 15 mm delamination. 84

Figure 7.1 (a) Comparison of 220 kHz pitch-catch time domain signal between undamaged and damaged specimens, and (b) phase shift vs. the lap joint delamination length. 90

LIST OF TABLES

Table 2.1 Adhesive thicknesses and actuator resonant frequencies of three different specimens.21

Table 2.2 Geometric dimensions and material constants of the structure used for wave speed calculation. 24

Table 2.3 Geometric dimensions and material constants of the structure and PWAS used in the simulation. 40

Table 2.4 Bonding layer parameters that matched simulation with measurements. 43

Table 3.1 Geometric dimensions and material constants of the structure and PWAS used in the simulation. 51

Table 3.2 The measured adhesive thicknesses of three different specimens. 56

Table 3.3 Adhesive layer parameters that provide better match between the simulations and measurements. 60

Table 5.1 Geometric dimensions and material constants of the structure used for wave speed calculation. 77

CHAPTER 1

INTRODUCTION

The civil, mechanical, and aircraft structures deteriorate over time due to the aging of materials, cyclic loading, overloading, climatic conditions, poor maintenance, etc. Degradation of the structures can eventually cause catastrophic failure, which poses a threat to public safety and economy. In order to maintain reliability, safety, and efficient usage of structures, structures are monitored using several sensors: piezoelectric sensor, ultrasonic sensor, acoustic emission sensor, fiber optic sensor, strain gauge, etc. Lately, structural health monitoring using piezoelectric sensors has emerged as one of the most popular techniques due to their low cost, light weight, low profile, large coverage area, and high frequency bandwidth. This technique utilizes the direct and converse piezoelectric effects. The direct piezoelectric effect involves deposition of charge in the piezo terminals due to the applied mechanical load whereas the converse effect is associated with the electromechanical conversion; converting applied electrical voltage at the piezo terminals into the mechanical deformation of the piezo. The two most popular structural health monitoring (SHM) techniques based on the piezoelectric transducer are: (I) EMI based SHM; and pitch-catch based SHM.

1.1 Literature review on EMI based SHM

In the past two decades, electromechanical impedance (EMI) based SHM has attracted many attentions (Park et al. 2003, Park, Yun & Inman 2008, Giurgiutiu 2008). This technique is based on the premise that the mechanical impedance of the structure and the electrical impedance of

the PWAS are coupled. As such, damage developed in the structure alters its mechanical impedance, which in turn changes the electrical impedance of the bonded PWAS. The change in the PWAS EMI, therefore, is considered as an indication of damage presence in the structures. Damage development in the structure, on the other hand, is not the only factor that influences the PWAS EMI. For example, the adhesive layer could have a strong influence on the EMI of a bonded PWAS (Yang, Lim & Soh 2008a, Qing et al. 2006, Moharana, Bhalla 2012, Huang, Song & Wang 2010).The EMI changes contributed by the adhesive condition could be misidentified as being caused by structural damage, leading to false alarms. In order to differentiate these two types of EMI changes, fundamental understandings on the physical connections between the adhesive layer and the PWAS EMI are needed.

The adhesive layer provides intimate coupling between the PWAS and the structure, and thus, its effects on the EMI of the bonded PWAS can be investigated based on the strain transfer from the PWAS to the structure. Simulation models, both analytical and finite element (FE) models, have been developed to study the coupling between the PWAS actuator and the host structure via the adhesive layer. In general, the published analytical models can be classified into two categories, i.e. the shear lag models and the impedance models. The shear lag parameter was first introduced by (Crawley, Lius 1987) to represent the difference in the strains of the PWAS and the host structure, i.e. the shear lag. Following their original work, a great deal of efforts has been provided for investigating the strain transfer from the PWAS to the structure along the length of the PWAS (Crawley, Anderson 1990, Lin, Rogers 1994, Park, Walz & Chopra 1996, Rabinovitch, Vinson 2002, Sirohi, Chopra 2000, Nguyen, Pietrzko & Buetikofer 2004). Initially, these models were developed mainly for vibration control of the structures. Since the frequency

of interests was much lower than the resonance of the PWAS actuator, the mechanical dynamics of the PWAS was ignored. Both the structure and the PWAS actuator were modeled using static governing equations. Later on, the shear lag parameter was directly adopted in the dynamic governing equation of the structure to calculate the PWAS EMI at ultrasound frequencies (Yan et al. 2007, Zhang et al. 2011, Tinoco, Serpa 2011). In these models, the PWAS actuator was assumed to deform along the longitudinal direction only while the host structure was either modeled as a Timoshenko beam (Yan et al. 2007, Zhang et al. 2011) or as an extensional bar (Tinoco, Serpa 2011). One of the shortcomings of the shear lag model is that the shear lag parameter is a compound function of the material and geometric properties of the PWAS, the adhesive layer, and the host structure as well as a constant α that depends on the assumed strain distribution. The connection between the constant α and the adhesive layer is not clear. Therefore, it is difficult to fully characterize the effect of the adhesive layer using the shear lag parameter alone.

The impedance model was first proposed by (Liang, Sun & Rogers 1994) using the concept of mechanical impedance. The dynamic characteristics of the structure were represented by a 1D spring-mass-damper system. The mechanical impedance of the structure was applied directly as the boundary condition of the PWAS and thus ignored the adhesive layer. (Giurgiutiu, Zagrai 2005) developed a 1D impedance model for a circular PWAS bonded on an infinitely large plate. Again, the adhesive layer was not considered. (Xu, Liu 2002) was the first one to incorporate the adhesive layer into the impedance model by representing the adhesive layer as 1D spring-mass-damper system and placing the adhesive layer in series with the structure. They introduced a coupling parameter that is determined by the dynamic stiffness of the structure and the adhesive

layer. This coupling parameter accounts for the amount of coupling between the PWAS and the structure through the adhesive layer. Unfortunately, the explicit relationship between the coupling parameter and the physical properties of the adhesive layer, e.g. its thickness and elastic modulus, was not established. (Dugnani 2009) modeled the dynamic behavior of the adhesive under a disk-shape PWAS using a 1D impedance model. Later on, (Bhalla, Soh 2004) formulated a 2D semi-analytical model using the concept of mechanical impedance where the excitation force was derived by applying the static force equilibrium condition on an infinitesimal PWAS element. They also incorporated the shear lag parameter into their model. The mechanical impedance of the structure was evaluated using a finite element model.

Even though the analytical models described above can provide some qualitative explanations of the adhesive layer effects on the EMI signature of the PWAS, the correlation between the simulated and measured EMI curves was rather poor (Yang, Lim & Soh 2008b). Attributing the discrepancies between the measured and simulated EMIs to the shortcomings of the analytical models, researchers resorted to hybrid spectral element methods (Ha, Chang 2010) or three-dimensional (3D) FE models (Annamdas, Soh 2007, Moharana, Bhalla 2012, Yang, Lim & Soh 2008a, Gresil et al. 2012, Giurgiutiu et al. 2012, Makkonen et al. 2001, Liu, Giurgiutiu 2011, Lim, Soh 2014) in an attempt to achieve more realistic simulation results. The 3D FE simulation displayed some of the resonant peaks that were not present in the analytical simulations. This indicates that the deformations of the PWAS and/or the structure were multi-mode in nature and the single-mode analytical models developed so far were not able to capture the multi-mode characteristics of the PWAS EMI signature. Unfortunately, numerical simulations are very computationally expensive and inaccurate especially for high frequency dynamic analysis (Gresil

et al. 2012). Since some of the input parameters, such as the shear modulus and mechanical loss coefficient of the adhesive layer, are usually unknown, tuning these parameters by trial-and-error to match the simulation results with experiment is extremely time-consuming and impractical.

The thickness and elastic modulus of the adhesive layer are the most commonly investigated parameters in evaluating the effects of the adhesive layer on the PWAS EMI signature. These two parameters were investigated independently by all published work so far. For example, the shear lag model indicated that a lower shear modulus and thicker adhesive layer reduces the shear transfer between the PZT and host structure. Similarly, (Bhalla, Soh 2004) suggested using an adhesive with a high shear modulus and the smallest thickness to minimize the influence of the adhesive layer. These observations agree with our discovery that the adhesive effect can be represented using a lumped parameter (i.e. the thickness-modulus ratio) instead of two separate parameters. In addition to the adhesive thickness and elastic modulus, the mechanical damping of the adhesive layer was also investigated at limited cases (Bhalla, Soh 2004, Moharana, Bhalla 2012). It was discovered that the mechanical damping does not have a significant influence on the PWAS EMI. In a more physics-based formulation, (Jin, Wang 2011) adopted a viscoelasticity model for the adhesive layer, in which the shear modulus of the adhesive layer has an imaginary part that is linearly proportional to the ultrasound frequency and the coefficient of viscosity. Again, the influence of the coefficient of viscosity was found to be not as significant as that of the adhesive thickness.

1.2 Proposed EMI based analytical model

In this work, we performed both experimental and analytical studies to investigate the effects of the adhesive layer on the EMI signature of the bonded PWAS. First, we experimentally demonstrated that the adhesive layer thickness has a strong influence on the PWAS EMI by bonding the PWASs on a slender structure with three different adhesive thicknesses. Time-frequency analysis of the broadband pitch-catch signal indicated that the dominant PWAS resonances are associated with both the longitudinal and flexural vibrations of the structure. Subsequently, a multi-mode analytical model that accounts for both structural vibrational modes was established by introducing a shear transfer parameter. Based on the formulation of the multi-mode analytical model, we discovered that the adhesive layer can be represented by two parameters, namely the shear transfer parameter and the thickness-shear modulus ratio. Parametric studies were carried out to study the effects of these two parameters on the PWAS EMI. The understandings gained from the parametric studies helped us in adjusting the adhesive layer parameters to match the simulated PWAS EMI curves with the experiment measurements.

1.3 Literature review on pitch-catch based SHM

Lamb waves are guided elastic waves that are confined by two parallel boundaries and can be highly sensitive to cracks, inclusions, and disbonds (Lamb 1917). As such, Lamb waves play an important role for SHM and nondestructive evaluation (NDE) of materials (Raghavan, Cesnik 2007, Giurgiutiu 2008). Lamb waves can be excited either using packaged ultrasonic transducers (Lowe, Cawley 1994, Rus, Wooh & Gallego 2004, Worlton 1956, Giurgiutiu 2005) or piezoelectric wafer transducers (Giurgiutiu 2005). Packaged ultrasonic transducers are too bulky

to be permanently installed on structures for in-situ SHM. On the other hand, piezoelectric wafer transducers have drawn immense attentions from researchers due to their low cost, lightweight, and small profile (Giurgiutiu 2005). As a common practice, piezoelectric wafer transducers are bonded on the structures using adhesive. The adhesive layer provides a mechanical coupling that transfers the deformation of the piezoelectric wafer transducer to the structure and vice versa. Even though the adhesive layer effects on the electromechanical impedance (EMI) signal demonstrates that adhesive thickness is a prominent design parameter (Islam, Huang 2014b, Bhalla, Soh 2004, Dugnani 2009, Xu, Liu 2002), the effects of the adhesive layer on the ultrasound pitch-catch signals have not been explored extensively. (Qing et al. 2006) investigated the effects of the adhesive layer on the Lamb wave signal using six different adhesive thicknesses and three different adhesive stiffness for the excitation frequencies of 50, 300, and 500 kHz. Their experimental results demonstrated that the amplitude of the ultrasound pitch-catch signal is greatly affected by the changes in the thickness and shear modulus of the adhesive layer. In addition, they discovered that the specimen with thin adhesive thickness has a higher pitch-catch amplitude at low frequency, e.g. 50 kHz, but lower pitch-catch amplitude at a higher frequency, e.g. 500 kHz, compared to the one with thicker adhesive thickness. (Park et al. 2006) performed an experimental study to assess the integrity of the bonding layer using circular PWASs bonded on a large thin plate. Based on their experimental study, the degraded bonding layer changes the phase, amplitude, and shape of the pitch-catch signal. However, they did not perform parametric studies of the bonding layer effects on the pitch-catch signal.

In addition to experimental studies, analytical and numerical simulation models have to be developed to study the effects of the adhesive layer on the pitch-catch signal. (Crawley, Lius

1987) presented a one-dimensional (1D) static elastic model of the adhesive layer that couples the displacement of the piezoelectric wafer actuator to the structure through shear deformation. Their model leads to a classical shear lag solution with a shear lag parameter that is a function of the adhesive layer properties, the actuator-structure stiffness ratio, and an unknown constant depending on the assumed beam strain distribution. (Santoni-Bottai, Giurgiutiu 2012) extended the 1D shear lag model presented by (Crawley, Lius 1987) to two-dimensional (2D) structures with N generic guided-wave modes. The shear-lag effect of the adhesive layer was represented by an aggregate number that expresses the participation of the various wave modes. Their work, however, was focused on determining the shear-lag transfer parameter to achieve an improved Lamb-wave tuning model. As such, the optimization of the adhesive layer to achieve more efficient excitation of lamb waves was not discussed. (Willberg, Duczek & Gabbert 2013) attempted to optimize the Lamb wave generation by performing parametric studies on the actuator length as well as the shear modulus and thickness of the adhesive layer using Finite Element (FE) simulation. They demonstrated that the amplitude of the pitch-catch signal is influenced by the excitation frequency as well as the adhesive layer thickness. They simulated the 2D plane strain condition using quadrilateral linear and reduced integration elements. In order to capture the wave propagation using linear elements accurately, the length of the discretized elements must be less than one-twentieth of the wavelength of the excited elastic waves and the time step must be less than one-twentieth of the wave period (Shen, Giurgiutiu 2014). Due to the fine spatial and time discretization, simulating wave propagations using FE is very expensive in terms of both computational time and computer resources (Moser, Jacobs & Qu 1999). (Ha, Chang 2010) implemented a hybrid spectral element method (SEM) in order to

study the adhesive layer effects on the Lamb wave sensing signal. SEM adopts non-linear and linear interpolation functions for simulating in-plane and out-of-plane wave propagation, respectively. The higher order interpolation function can capture the wave propagation signal with larger elements and thus reduces the simulation time significantly. Despite SEM takes much less computational time compared to the FE models (e.g. the SEM takes 43 min to simulate Lamb wave propagation at 100 kHz, whereas the FEM takes 452 min for a given computer configuration), the simulation time of SEM is still expensive compared to the analytical model.

1.4 Proposed GW based pitch-catch analytical model

Extending the EMI analytical model, we developed an efficient analytical model that can simulate the Lamb wave pitch-catch signals generated by a bonded piezoelectric wafer actuator. Parametric studies on the adhesive layer properties indicated that there exists an adhesive thickness at which the longitudinal and flexural mode pitch-catch signals can be maximized. These predictions were validated by measurements. In addition, we were able to achieve better matches between the simulations and measurements by adjusting the adhesive layer parameters, e.g. the shear transfer parameter and shear modulus. The simulation model is highly efficient compared to SEM and FEM since it takes less than one minute to simulate the Lamb wave propagation for a given frequency.

1.5 Combining the pitch-catch and pulse-echo methods to detect composite lap joint damage

Adhesively bonded lap joint structures have been widely used in metallic and composite structures as well as in repairing civil structures. It can extend the service life, reduce the total

weight of the structure, and homogeneously transfer stresses in comparison to the mechanical joints such as rivets, screws, and bolts (Higgins 2000, Wu et al. 2008, Campilho, De Moura & Domingues 2005). Besides the abundant use of lap joints in metallic structures, the use of the composite lap joint has been increased lately. However, failures are frequently initiated at the lap joint adhesive layer because of the high stress concentration at the free ends of the lap joint region and the lower strength of the adhesive material compared to the adherends (Her 1999a, Campilho, De Moura & Domingues 2005). Therefore, frequent inspections of the lap joint regions are needed to ensure safe operations of these structures.

Guided wave based structural health monitoring (SHM) technique has been widely used for nondestructive evaluation (NDE) of structural integrity (Raghavan, Cesnik 2007). Guided waves are either concentrated near the boundaries or confined between two parallel boundaries (Viktorov 1967). The guided wave that is concentrated near the boundaries is called Rayleigh wave, i.e. surface wave, and is very sensitive to the surface defects. The guided wave that is constrained by the two boundaries is called Lamb wave and is very sensitive to cracks, inclusions, and disbonds. The Lamb wave consists of longitudinal and flexural deformations of the structure (Lamb 1917), which can be excited either using packaged ultrasonic transducers (Lowe, Cawley 1994, Rus, Wooh & Gallego 2004, Worlton 1956) or PWAS transducers (Giurgiutiu 2005). Packaged ultrasonic transducers are too bulky to be permanently installed onboard for in-situ SHM. On the other hand, PWAS transducers have drawn immense attention from researchers due to their low cost, lightweight, and small profile (Giurgiutiu 2005).

The Lamb waves are utilized for damage detection of the structure using several methods: pitch-catch; pulse-echo; and electromechanical impedance (EMI) methods. In the pitch-catch method,

the Lamb wave signal excited by a PWAS actuator travels through the damaged area and is received by a PWAS sensor. As such, it requires at least a signal generator for excitation and an oscilloscope to monitor the received signal. The pitch-catch technique is especially implemented to detect damage over a large distance by comparing the received sensing signals between the damaged and undamaged structures (Dalton, Cawley & Lowe 2001, Giurgiutiu 2005, Giurgiutiu, Bao & Zhao 2003, Alleyne, Cawley 1992). Usually, the pitch-catch signal was measured at a particular excitation frequency that provides the maximum response, also called a *sweet spot*. In comparison, a broadband technique that requires the acquisition of broadband pitch-catch response could take a few hours or more (Giurgiutiu, Bao & Zhao 2003). Even though the pitch-catch method can detect the presence of damage, it cannot detect the location of the damage unless a dense transducer network is used (Raghavan, Cesnik 2007). On the other hand, the pulse-echo method implements a single PWAS transducer to excite the Lamb waves and receive the echo signal reflected at the boundaries and/or the damage. The damage location can be detected provided that the reflections from the boundaries are identified using the known wave speeds. The damage location is identified either by filtering out the reflections or subtracting pulse-echo signal from the baseline measurements (Cuc, Giurgiutiu 2004, Giurgiutiu, Bao & Zhao 2003, Raghavan, Cesnik 2007). The EMI technique utilizes the EMI of the PWAS transducer for SHM. The damage alters the mechanical impedance of the structure which in turn changes the EMI of the PWAS transducer. Conventionally, the EMI method is suitable for local damage detection and is implemented using an impedance analyzer (Cawley 1984, Giurgiutiu, Reynolds & Rogers 1999, Cuc, Giurgiutiu 2004, V. Giurgiutiu 2007). It is worth noting that

these three ultrasound inspection techniques are usually implemented separately using different instruments. Therefore, it is not possible to acquire all the three measurements simultaneously.

1.6 Proposed S-parameters to detect severity of composite lap joint damage

We introduced the S-parameters for the damage detection of the composite lap joint adhesive layer. As a broadband measurement, the S-parameters can be acquired in a few seconds using a compact instrument. Moreover, the ultrasound pitch-catch, pulse-echo, and EMI signals can be derived from the S-parameters simultaneously using signal processing algorithms (Huang, Bednorz 2014). Based on the time-frequency analysis of these signals, we discovered that the influences of the lap joint damage on the ultrasound signals are time and frequency dependent.

1.7 Combining pitch-catch and pulse-echo methods to detect aluminum lap joint delamination

Over the past century, adhesively bonded lap joint structures have been widely used in aerospace, mechanical, and civil structures (Adams, Comyn & Wake 1997, Metzinger, Guess 1996, da Silva, Lucas Filipe Martins, Öchsner 2008). Adhesively bonded lap joint extends the service life, and reduces the total weight of the structure. Capable of homogeneously transferring stresses in comparison to mechanical joints such as bolts, rivets, and screws (Higgins 2000, Wu et al. 2008, Campilho, De Moura & Domingues 2005), adhesive lap joints also offer more fatigue strength than riveted/bolted joints (Adams, Comyn & Wake 1997, Higgins 2000). In addition, the adhesive joint does not introduce stress concentration in the contact area between the fastener and the structure, which reduces the residual strength of the lap joints (Campilho, De Moura & Domingues 2005). However, cracks are frequently initiated at the lap joint adhesive

layer because of the high stress concentration at the free ends of the lap joint section and lower strength of the adhesive material compared to the adherends (Her 1999b, Campilho, De Moura & Domingues 2005). Therefore, there is a growing demand in monitoring the health of the lap joints to ensure the safe operation of the structures.

Extensive researches have been done by many researchers to monitor the integrity of structures using Lamb waves (Raghavan, Cesnik 2007, Viktorov 1967, Su, Ye & Lu 2006). Lamb waves are bounded by the top and bottom surfaces of plate-like structures and propagate parallel to the surfaces. Depending on the frequency-thickness product, multiple Lamb wave modes could be generated simultaneously which results in a Lamb wave signal that is too complex to be useful for damage detection (Lowe, Challis & Chan 2000, Puthillath et al. 2008, Song et al. 2003). Therefore, it is advised to use excitation frequencies at which a minimum number of modes are excited in the structures. Ideally, only the first order symmetric (S0) and/or the anti-symmetric (A0) modes should be excited. These two first order modes correspond to the longitudinal and flexural modes of the structure (Lamb 1917), which can be excited by bonding a piezoelectric wafer transducer (PWaT) on the structure (Giurgiutiu 2005).

The three common techniques for Lamb wave based SHM schemes are the pulse-echo, pitch-catch, and electromechanical impedance (EMI) methods. The pulse-echo method utilizes a single PWaT to excite the Lamb waves in the structure and receive the echoes reflected from the damage. Using the pulse-echo signal, both the presence and severity of damage can be identified from the Lamb wave amplitude change (Giurgiutiu, Bao & Zhao 2003, Loveday, Long & Burger 2013, Yang, Qiao 2005). (Loveday, Long & Burger 2013) demonstrated the feasibility of

detecting damage in the rail tracks up to a distance of over 500 meters. (Cuc 2002, Shen, Giurgiutiu 2014) identified the location of a crack in the lap joint structure using the arrival of a new wave in the pulse-echo signal. For pulse-echo technique, (Giurgiutiu, Cuc 2005) argued that the longitudinal mode is better than the flexural mode in detecting damage because the longitudinal mode is less dispersive and has less attenuation. While many researchers have used a specific excitation frequency for the pulse-echo based damage detection, nobody has demonstrated a systematic approach on how to select the excitation frequency to achieve optimal damage detection.

In the pitch-catch method, Lamb wave excited by a PWaT travels through the damaged area and is received by another PWaT. As such, it requires at least a signal generator for excitation and an oscilloscope to monitor the received signal. The presence of damage or the damage severity was detected from the amplitude change of the pitch-catch signal (Dalton, Cawley & Lowe 2001, Giurgiutiu 2005, Giurgiutiu, Bao & Zhao 2003, Alleyne, Cawley 1992, Lee, Staszewski 2003, Yu et al. 2012, Song, Huang & Hu 2012, Crider II 2007, Bhuiyan, Shen & Giurgiutiu 2016). Usually, the pitch-catch signal was measured at a particular excitation frequency that provides the maximum response, also called a *sweet* spot (Giurgiutiu 2005). To find the *sweet* spot, acquiring the broadband pitch-catch response is required which may take a few hours or more (Giurgiutiu, Bao & Zhao 2003, Islam, Huang 2016). Even though extensive researches have been done to detect the damage in the structure using a Lamb wave pitch-catch signal, few researchers have investigated using this method for the detection of lap joint damage in metallic structures. (Ihn, Chang 2002) monitored the fatigue crack growth in aluminum lap joint by defining a damage index as the ratio of the pitch-catch signals between the damaged and undamaged

specimens (Cuc 2002, Quaegebeur et al. 2012) and (Mal et al. 1996) identified the lap joint damage of the metallic structure from the amplitude attenuation of the pitch-catch signal. Based on the same principle, (Matt, Bartoli & Lanza di Scalea 2005) detected the lap joint damage of composite structures. Despite a large number of research articles have been published on detecting the presence of damage using the pitch-catch signal, detecting the damage severity using the pitch-catch signal, however, is extremely rare. This might due to the fact that the amplitude of a pitch-catch signal may not be proportional to the damage severity during the entire duration of the signal, i.e. the amplitude may increase or decrease at different time spans depending on the size of the damage (Lee, Staszewski 2003). Similar to the pulse-echo method, all the researchers selected a specific excitation frequency for the pitch-catch method but no discussion was made why a particular frequency was selected.

The EMI SHM technique is based on the premise that damage alters the mechanical impedance of the structure which in turn changes the EMI signature of a PWaT bonded on the structure. Conventionally, the EMI method is considered to be more suitable for local damage detection, and is implemented using an impedance analyzer (Giurgiutiu, Reynolds & Rogers 1999, Cuc, Giurgiutiu 2004, Giurgiutiu 2008, Park et al. 2003). (Giurgiutiu, Reynolds & Rogers 1999) was the first one who investigated using EMI signal to monitor a spot welded single lap joint. (Gulizzi, Rizzo & Milazzo 2015) studied the EMI signal to monitor the strength of an adhesively bonded lap joint structure. (Ritdumrongkul et al. 2003) demonstrated how the EMI signal can detect the tightening or loosening of a bolted joint. (Park, Inman 2007, Park, Yun & Inman 2008) detected cracks in the metallic and concrete structure. EMI-based damage detection, when performed in the frequency domain, can only provide the indication of damage presence but not

the physical details of the damage such as damage size or location. Recently, (Zahedi, Huang 2017, Islam, Huang 2015) discovered that the EMI signature is essentially the frequency-domain representation of the pulse-echo signal. Performing time-frequency analysis of the EMI signature can thus enable physical-based damage detection.

1.8 Proposed S-parameters to detect severity of aluminum lap joint delamination

This paper investigates the scattering parameters, i.e. the S-parameters, for detecting the delamination in a lap joint that connects two aluminum beams. S-parameters are commonly used in microwave engineering for device and network characterization. However, its introduction for ultrasound-based SHM was only proposed recently by (Huang, Bednorz 2014). Treating a structure instrumented with two PWaTs as a two-port network, (Huang, Bednorz 2014) demonstrated that the reflection and transmission S-parameters represent the broadband pulse-echo and pitch-catch responses of the system, respectively. Contrary to conventional SHM schemes that only acquire the pulse-echo or pitch-catch signal, the S-parameters can be acquired simultaneously using a single instrument. Extracting the pulse-echo and pitch-catch signals from the S-parameters can thus enable better correlations between these two types of signal. In addition, time-frequency analysis of the broadband S-parameters also facilitates the identification of PWaT resonances and the Lamb wave modes that are associated with each resonance (Zahedi, Huang 2017). While (Huang, Bednorz 2014) demonstrated that the time domain response of the system with any excitation signal can be extracted from the S-parameters using digital signal processing algorithm, the specimen they studied did not have any damage. As a result, the effects

of damage on the S-parameters were not discussed. In this paper, we investigate correlating the reflection and transmission S-parameters for lap joint damage detection. We hypothesize that the frequency at which the damage cannot influence the resonant phase amplitude is the best one to detect the damage severity. Based on our hypothesis, 220 kHz resonance was selected to detect the damage severity. The lap joint damage severity was identified using the amplitude difference of 220 kHz resonance time domain pitch-catch and pulse-echo signals between undamaged and damaged specimens. In addition, a new technique, i.e. phase shift, was implemented to detect the damage severity. Using the phase shift of pitch-catch signals between undamaged and damaged specimens, the damage length of the lap joint structure was also estimated.

1.9 Research goals and approaches

The goals of this research are: I. to investigate the effects of the adhesive layer on the PWAS EMI; II. to optimize the adhesive layer thickness for Lamb wave signal; III. to detect the damage severity of lap joints in aluminum and composite structures using S-parameters.

An EMI based analytical model was established to perform parametric study on the effects of the adhesive layer shear modulus-thickness ratio and the shear transfer parameter on the EMI signature. Three specimens were instrumented by bonding PWASs with three different adhesive thicknesses based on the parametric study. The simulated EMI was matched with the measured ones by adjusting the material properties of shear modulus and shear transfer constant. Thus, the unknown shear modulus of the adhesive layer was estimated. The detailed study of EMI analytical simulation is discussed in chapter 2.

Chapter 3 discusses how the EMI analytical model was extended to establish the pitch-catch analytical model. The simulation prediction of an optimized adhesive thickness which provides the maximum pitch-catch signal amplitude for a given structure is demonstrated. The simulation prediction was validated using measurements.

Chapter 4 discusses the implementation of S-parameters to detect the damage severity of a composite lap joint structure. It was shown that the frequency domain EMI signature and S11 parameter are similar to the time-domain pulse-echo signal. Based on the time domain signal of pulse-echo and pitch-catch signal derived from S11 and S21, respectively, we have identified the damage severity of a composite lap joint structure using the amplitude change of the pulse-echo and pitch-catch signal.

Chapter 5 demonstrates the implementation of the S-parameters to detect the damage severity of an aluminum lap joint structure. In this work, we proposed a new hypothesis to select the best excitation frequency to detect the damage severity using the pulse-echo and pitch-catch signals; we have also introduced a new parameter, i.e. the phase shift, to detect the severity of damage. Based on the phase shift, the lap joint delamination length was detected.

CHAPTER 2

EFFECTS OF ADHESIVE THICKNESS ON THE PWAS EMI SIGNATURE

2.1 Specimen configurations, transducer installation, and admittance measurements

A picture of an instrumented specimen is shown in Figure 2.1(a). A thin, slender, aluminum structure with a length of 500 mm, a width of 10 mm, and a thickness of 1.55 mm was instrumented with two PWAS transducers (PI Ceramic, PIC 151, 10 mm in length and width, 0.2 mm in thickness); the PWAS actuator was located at the center of the structure while the PWAS sensor was located at a distance of 100 mm from the actuator. Both transducers

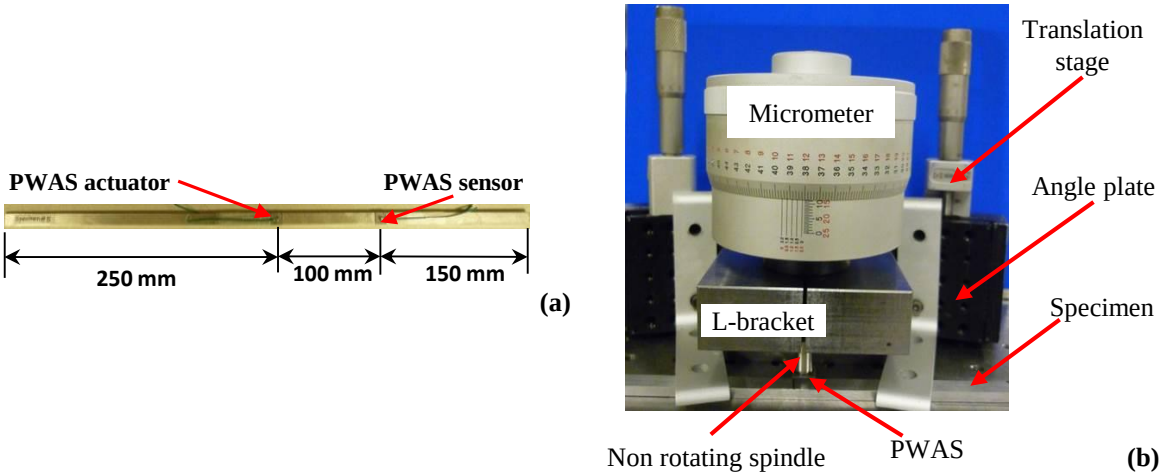

Figure 2.1 (a) An aluminum structure instrumented with a PWAS actuator at the center and a PWAS sensor at 100 mm from the actuator; (b) fixture for installing PWAS transducers on the structure.

were bonded on the structure using gel type superglue (Loctite 136407) as the adhesive material. In order to control the adhesive thickness precisely, a fixture using a micrometer head with a non-rotating spindle (Mitutoyo 253-202, accuracy +/- 0.001 mm) was implemented. As shown in Figure 2.1(b), the micrometer head was supported by a rigid L-bracket mounted on an optical table. Two manual translation stages were installed at either side of the L-bracket, on which angle plates were attached for clamping the specimen on the optical table. The PWAS transducer was attached at the tip of the spindle using a double sided tape. The reference position was first established by lowering the PWAS transducer to touch the specimen surface. The transducer was then moved upward so that the adhesive material can be applied on the specimen. Subsequently, the PWAS transducer was lowered to a position that gives the desired adhesive thickness. The spindle was detached from the PWAS after the adhesive was cured in about 30 min. After soldering the electric wires on the PWAS transducers, the side view of the instrumented specimens was imaged using a microscope. The adhesive thicknesses of the bonded PWAS transducers were calculated from the pixel counts of the adhesive layer using the thickness of the PWAS as the scaling reference.

It is worth noting that previous publications suggested using as thin adhesive thickness as possible for maximum excitation of the ultrasound waves (Nguyen, Pietrzko & Buetikofer 2004, Bhalla, Soh 2004). However, our recent work discovered that the maximum ultrasound signal was excited when the bonding layer thickness is around the same as the PWAS thickness for the specimen shown in Figure 2.1(a) (Islam, Huang 2014a). Therefore, the adhesive thicknesses selected for this study is centered around the PWAS thickness, i.e. 0.1 mm, 0.2 mm, and 0.3 mm. As shown in Table 2.1, the measured adhesive thicknesses for specimen #2 and #3 agreed well

Table 2.1 Adhesive thicknesses and actuator resonant frequencies of three different specimens.

Specimens	Thickness (mm)		Actuator Resonant Frequency (kHz)		
	Actuator	Sensor	1st	2nd	3rd
#1	0.118	0.110	80	234	411
#2	0.205	0.203	81	230	338
#3	0.298	0.299	81	218	320

with the selected values. The measured adhesive thicknesses for specimen #1, however, are slightly larger than the selected values. For specimen #1, it was a little challenging to detect the exact location of the specimen edge. This might have contributed to the discrepancies between the measured and desired adhesive thicknesses. Nonetheless, the small discrepancies should not have large effects on the observed EMI responses of the bonded PWAS actuators discussed below. The impedances of the bonded PWAS actuators were measured using a Vector Network Analyzer (Rohde & Schwarz, ZVL32) with a frequency resolution of 1.0 kHz. The real and imaginary part of the impedance and admittance for the three specimens are shown in figure 2.2(a)-2.2(d). Both the impedance and admittance components demonstrated that the adhesive thickness has a strong influence on the spectral locations and amplitudes of the resonant peaks, especially for the resonances at higher frequencies. In comparison to the impedance constituents, the admittance counterparts display more distinct resonances. Therefore, only the admittance constituents of the actuators will be investigated herein. The first three distinct resonant frequencies of the actuators were measured from the conductance curves and given in Table 2.1. The 1st resonant frequency was almost identical for all three specimens. However, the 2nd and 3rd resonant frequencies shifted significantly with the adhesive thickness, indicating that the high frequency resonances are more sensitive to the adhesive condition. This observation agrees with

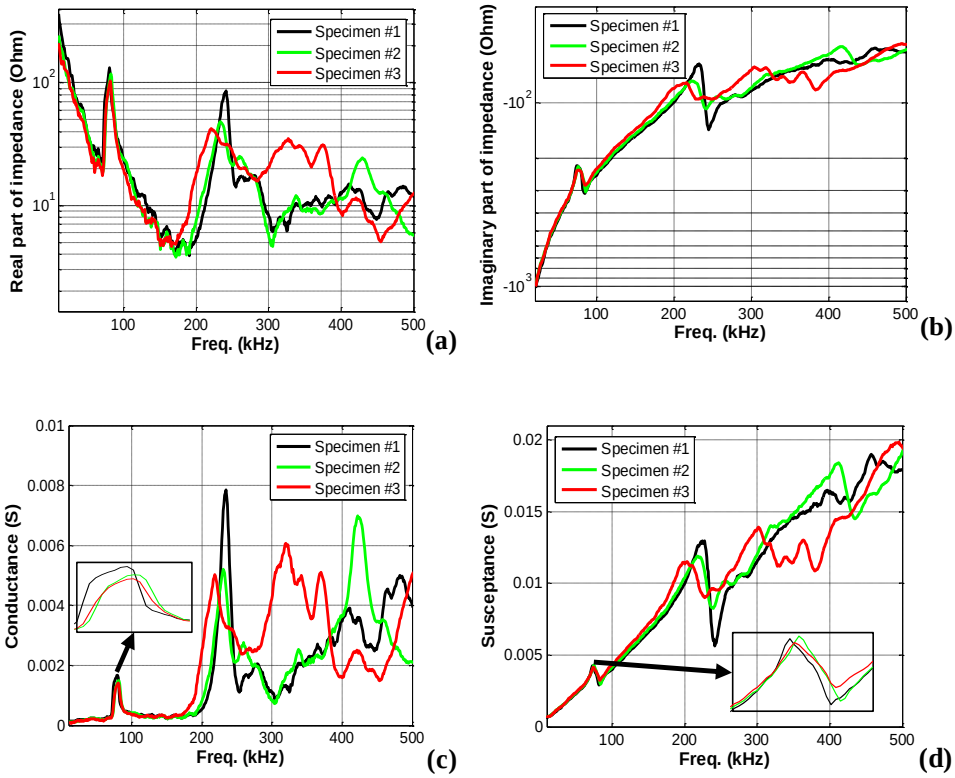

Figure 2.2 Impedance and admittance constituents of the PWAS actuators bonded with different bonding thicknesses; (a) real part of impedance, (b) imaginary part of impedance, (c) real part of admittance (i.e. conductance), and (d) imaginary part of admittance (i.e. susceptance).

other researchers' observation that the EMI and ultrasound responses of the PWAS actuator are more sensitive to the adhesive conditions at high frequencies (Qing *et al* 2006, Moharana and Bhalla 2012, Khodaei *et al* 2013), which is most likely due to the short wavelengths of the ultrasound waves at these frequencies.

2.2 Ultrasound mode identification

Since the three resonant peaks observed in figure 2.2 could be related to different ultrasound modes, the ultrasound modes associated with these resonances have to be identified first in order

to develop a physics-based analytical model. Considering that the wave speeds of the ultrasound modes are different, we can determine the ultrasound modes from their time-of-flight (TOF) by performing the time-frequency analysis of the broadband ultrasound pitch-catch signal (Oppenheim, Schafer & Buck 1989). The flow-diagram of the time-frequency analysis is illustrated in Figure 2.3.

First, broadband ultrasound waves were excited by supplying a sinc signal to the ultrasound actuator. As long as the bandwidth of the sinc signal is sufficiently larger than the frequency bandwidth of interest, we can consider the sensing signal received by the PWAS sensor as the impulse response of the ultrasound pitch-catch system. The transfer function *H(f)* that characterizes the input-output relationship of the ultrasound pitch-catch system can then be calculated by performing Fast Fourier Transformation (FFT) on the received broadband pitch-catch signal. Once the transfer function *H(f)* is determined, the response of the system to a narrow-band excitation, such as a 5.5 cycle tone-burst signal, can be calculated by multiplying the spectrum of the excitation signal *I(f)* with the transfer function *H(f)*. Applying the Inverse Fast Fourier Transformation (IFFT) to the resulting signal, i.e. $O(f) = H(f)^* I(f)$, produces the

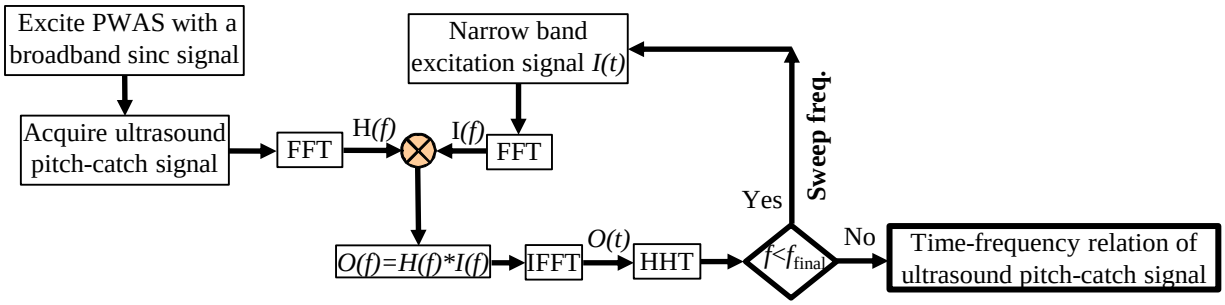

Figure 2.3 Flow diagram for time-frequency analysis of broadband ultrasound pitch-catch signal.

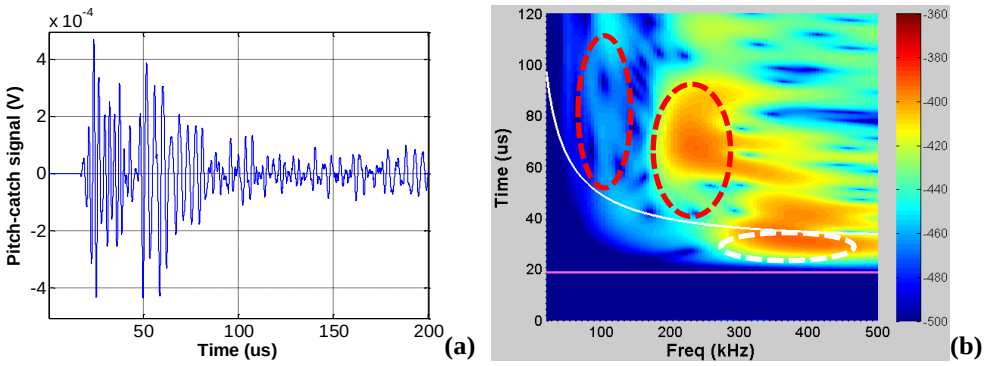

Figure 2.4 (a) Broadband ultrasound pitch-catch signal acquired from specimen #2 and (b) its time-frequency representation (the amplitude is in dB scale).

time-domain ultrasound pitch-catch signal *O(t)* that is excited by the narrowband tone-burst signal *I(t)*. Varying the center frequency of the tone-burst excitation signal *I(t)* will therefore result in a series of narrow band pitch-catch signals. The envelopes of these narrow band pitch-catch signals *O(t)* were obtained using the Hilbert-Huang Transformation (HHT). Thus, the time-frequency representation of the system response can be constructed by plotting the envelope of the narrow band pitch-catch signals in a 3D plot, in which the x-axis is the center frequency of the excitation signals *I(t)*, the y-axis is the time scale of the pitch-catch signals *O(t)*, and the z-axis is the envelope amplitude of the pitch-catch signals *O(t)*.

The broadband pitch-catch signal acquired from specimen #2 is represented in time-domain in

Table 2.2 Geometric dimensions and material constants of the structure used for wave speed calculation.

W (m)	h (m)	I (m^4)	A (m^2)	E (GPa)	ν	ρ (kg/m^3)	k_s
$10X10^{-3}$	$1.55X10^{-3}$	$3.1X10^{-12}$	$1.55X10^{-5}$	68.95	0.3	2715	$\pi^2/12$

Figure 2.4(a) and in time-frequency domain in Figure 2.4(b). The time-domain representation alone does not explicitly reveal any information about the resonant frequencies of the PWAS. On the other hand, the time-frequency representation clearly shows that there are three dominant resonances whose frequencies match with the frequencies identified from the actuator admittance curve shown in figure 2.2. It must be noted that the amplitude of the pitch-catch signal envelope is presented in dB unit along the z-axis of Figure 2.4(b) for better distinction of the resonances. The pitch-catch signal envelope was obtained through the conversion from the time domain signal to the frequency domain signal and vice versa. During these conversions, the amplitude of the signal was not preserved. Thus, the amplitude given in Figure 2.4(b) is not the actual magnitude of the signal but the relative amplitude, which is sufficient for identifying the modes. The structural modes associated with these resonances can be determined by calculating their wave speeds from their TOFs and the travel distance.

Based on the classical structural dynamics theory, the theoretical wave speed for the longitudinal mode of an aluminum bar is independent of frequency and can be calculated as $\sqrt{E/\left(1-\nu^2\right)/\rho}$, where E is the Young's modulus, υ is the Poisson's ratio, and ρ is the density. On the other hand, the theoretical wave speed for the flexural mode of a Timoshenko beam is frequency dependent and can be calculated using the fourth order differential governing equation given in (Rao 2007). Using the parameter values given in Table 2.2, the TOF for a longitudinal wave traveling a distance of 100 mm is calculated to be 18.9 μs, as marked by the horizontal magenta line in Figure 2.4(b). Based on this TOF, the resonance at 338 kHz, i.e. the one circled in the white ellipse, is identified as the longitudinal mode. On the other hand, the TOF for the flexural wave

is represented by the white solid line. Clearly, the resonances at 81 and 230 kHz, i.e. the two marked by the red ellipses, are associated with the flexural mode. Therefore, a multi-mode analytical model that incorporates both vibration modes of the structure has to be developed in order to account for these two different PWAS resonance types.

Based on the time-frequency analysis, the resonance at 338 kHz is identified as the longitudinal mode. On the other hand, the resonances at 81 and 230 kHz are associated with the flexural mode. Therefore, a multi-mode analytical model that incorporates both vibration modes of the structure has to be developed in order to account for these two different PWAS resonance types.

2.3 Multi-mode admittance analytical model of bonded PWAS

A multi-mode analytical model for calculating the EMI of a PWAS actuator bonded on a slender structure is developed in this study. The longitudinal and flexural modes of the structure excited by the PWAS actuator were formulated separately and superimposed together, assuming that these two vibration modes are not coupled (Annamdas, Soh 2007, Pao, Keh & Howard 1999).

The analytical simulation model of a thin slender structure instrumented with a PWAS actuator is shown in Figure 2.5(a). The structure is sectioned along the edges of the PWAS so that two types of homogeneous sections, i.e. the one with a PWAS bonded on the top surface (i.e. the PWAS-structure section) and the one without a PWAS (i.e. the structure section) can be modeled using separate governing equations. The PWAS-structure section consists of three components: the PWAS, the adhesive layer, and the structure. The deformations of the PWAS and the structure are assumed to be coupled through the shear stresses at the PWAS-adhesive interface and the adhesive-structure interface, as shown in Figure 2.5(b). The shear stress along the PWAS-

adhesive layer interface τ_p can be calculated from the axial displacements of the PWAS and the structure (Crawley, Lius 1987) as

$$\tau_p(x,t) = G_a\gamma_a(x,t) = G_a\left[\frac{u_p(x,t)-u_s(x,t)}{h_a}\right]. \tag{2.1}$$

where G_a and h_a are the shear modulus and thickness of the adhesive layer. Therefore, equation (2.1) represents the coupling between the axial displacement of the PWAS u_p and the axial displacement of the structure u_s. To account for the shear lag effect of the adhesive layer, we introduced a shear transfer parameter α, which is defined as the ratio between the shear stress at the bottom and top surface of the adhesive layer, i.e.

$$\tau_s(x,t) = \alpha\tau_p(x,t). \tag{2.2}$$

Therefore, $\alpha = 1$ represents a perfect coupling between the PWAS and the structure while $\alpha = 0$ simulates no coupling between these two components. The governing equation for a PWAS operating in the longitudinal mode with the shear stress τ_p distributed on its bottom surface is given as

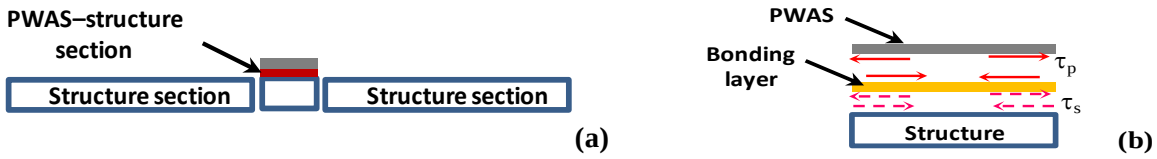

Figure 2.5 Simulation model of a thin slender structure instrumented with a PWAS actuator; (a) dividing the instrumented specimen into piecewise homogenous sections; (b) coupling of the PWAS and structure through shear stresses at the PWAS-adhesive layer and adhesive layer-structure interfaces.

$$E_p \frac{\partial^2 u_p(x,t)}{\partial x^2} - \frac{\tau_p(x,t)}{h_p} = \rho_p \frac{\partial^2 u_p(x,t)}{\partial t^2}, \tag{2.3}$$

where E_p, ρ_p, and h_p are the Young's modulus, density, and thickness of the PWAS. Similarly, the governing equation for the longitudinal mode of the structure with the shear stress τ_s applied on the top surface, is given as

$$E_s \frac{\partial^2 u_s(x,t)}{\partial x^2} + \frac{\tau_s(x,t)}{h_s} = \rho_s \frac{\partial^2 u_s(x,t)}{\partial t^2}. \tag{2.4}$$

Again, E_s, ρ_s, h_s are the Young's modulus, density, and thickness of the structure. Expressing $u_p(x, t)$, $u_s(x, t)$ and $\tau(x, t)$ as time-harmonic functions with an angular frequency ω, i.e.

$$u_p(x,t) = \bar{u}_p(x)e^{i\omega t}, u_s(x,t) = \bar{u}_s(x)e^{i\omega t}, \tau(x,t) = \bar{\tau}(x)e^{i\omega t}, \tag{2.5}$$

and combining equation (2.1) and (2.3) result in

$$\bar{u}_s = C_1 \frac{\partial^2 \bar{u}_p}{\partial x^2} + C_2 \bar{u}_p, \quad C_1 = -\frac{E_p h_a h_p}{G_a}, \quad \text{and} \quad C_2 = 1 - \frac{\rho_p \omega^2 h_a h_p}{G_a}. \tag{2.6}$$

Substituting equations (2.2) and (2.6) into equation (2.4), we obtain a fourth order differential equation that governs the displacement response of the PWAS, i.e.

$$\frac{\mathrm{d}^4 \bar{u}_p}{\mathrm{d}x^4} + A\frac{\mathrm{d}^2 \bar{u}_p}{\mathrm{d}x^2} + B\bar{u}_p = 0, \tag{2.7}$$

in which

$$A = \frac{C_2}{C_1} + \frac{1}{E_s}(\rho_s \omega^2 - \frac{\alpha G_a}{h_a h_s}) \text{ and } B = \frac{C_2}{C_1 E_s}(\rho_s \omega^2 - \frac{\alpha G_a}{h_a h_s}) + \frac{\alpha G_a}{E_s h_a h_s C_1}. \tag{2.8}$$

The solution of this 4th order differential equation is

$$\bar{u}_p = a_1 e^{\beta_1 x} + a_2 e^{\beta_2 x} + d_1 e^{-\beta_1 x} + d_2 e^{-\beta_2 x}, \tag{2.9}$$

where β_i (i =1, 2) are the characteristic roots of equation (2.7) while a_i and d_i are the unknown constants that have to be determined from the PWAS boundary conditions and the continuity conditions at the section interfaces. Substituting equation (2.9) into equation (2.6), the displacement of the structure can be derived as

$$\bar{u}_s = a_1\gamma_1 e^{\beta_1 x} + a_2\gamma_2 e^{\beta_2 x} + d_1\gamma_1 e^{-\beta_1 x} + d_2\gamma_2 e^{-\beta_2 x}, \tag{2.10}$$

where $\gamma_i = C_1\beta_i^2 + C_2$, ($i$=1, 2). For the structure sections that do not have a PWAS, the classical equation of an extensional bar undergoing longitudinal deformations, i.e.

$$E_s \frac{\partial^2 \bar{u}_s}{\partial x^2} = \rho_s \frac{\partial^2 \bar{u}_s}{\partial t^2} \tag{2.11}$$

still applies and its solution can be expressed as

$$\bar{u}_s = a_1 e^{k_1 x} + d_1 e^{-k_1 x}, \tag{2.12}$$

where $k_1 = i\omega\sqrt{\rho / E}$ and $\omega = 2\pi f$. Again, a_1 and d_1 are the unknown constants that have to be determined from the boundary and continuity conditions.

The unknown constants a_i and d_i in equation (2.9), (2.10), and (2.12) are determined by applying the boundary conditions of the structure and the PWAS as well as the continuity conditions at the section interfaces. Assuming both ends of the structure are free, the boundary conditions at the two free ends of the structure are expressed as

$$\sigma_L = \sigma_R = E_s \frac{d\bar{u}_s(x)}{dx} = 0. \tag{2.13}$$

The continuity conditions at the section interfaces can be defined as

$$\sigma(x^+) = \sigma(x^-) = E_s \frac{d\bar{u}_s(x)}{dx}, \bar{u}_s(x^+) = \bar{u}_s(x^-), \tag{2.14}$$

where x^+ and x^- denote the left and the right side of the interface, respectively. Applying the traction-free boundary conditions at the left and right end of the PWAS lead to the relationship between the PWAS displacement and the applied electric voltage $V = \bar{V}e^{i\omega t}$ (Crawley, Lius 1987)Crawley and Lius 1987), i.e.

$$\bar{\varepsilon}_p = \frac{d\bar{u}_p}{dx} = \frac{d_{31}\bar{V}}{h_p}. \tag{2.15}$$

Substituting equations (2.9), (2.10), and (2.12) into equations (2.13)-(2.15) results in a set of linear equations that can be solved for the unknown constants a_i and d_i. To overcome the numerical instability and inaccuracy at high frequencies, the reverberation matrix method (RMM) described in (Pao, Keh & Howard 1999, Howard, Pao 1998a) can be adopted to solve the resulting simultaneous equations.

The flexural vibration of the structure excited by a PWAS actuator can be formulated in a similar fashion. The governing equation of a Timoshenko beam with shear stresses applied only on the top surface can be derived following the Hamilton method (Rao 2007), which results in

$$\begin{aligned} &-E_s I_s \frac{\partial^2 \phi}{\partial x^2} - k_s A_s G_s \left(\frac{\partial w}{\partial x} - \phi \right) + \tau_s(x) \frac{h_s}{2} = -\rho_s I_s \frac{\partial^2 \phi}{\partial t^2} \text{ and} \\ &\mathrm{k}_s A_s G_s \left(\frac{\partial^2 w}{\partial x^2} - \frac{\partial \phi}{\partial x} \right) = \rho_s A_s \frac{\partial^2 w}{\partial t^2}. \end{aligned} \tag{2.16}$$

Compared to the differential equations given in (Yan et al. 2007), the shear stress term is divided by 2 since the PWAS is only bonded on one side of the structure while the PWASs were bonded symmetrically on the top and bottom surfaces of the structure in Yan's work. When the structure undergoes both longitudinal and flexural deformations, the axial displacement of the PWAS can

be calculated by superimposing these two displacements, assuming the system is linear (Annamdas, Soh 2007, Pao, Keh & Howard 1999), i.e.

$$\bar{u}_p = \bar{u}_p^{(l)} + \bar{u}_p^{(f)}, \tag{2.17}$$

where $\bar{u}_p^{(l)}$ and $\bar{u}_p^{(f)}$ are the axial deformation of the PWAS under longitudinal and flexural deformation of the structure, respectively. Once the displacement of the PWAS is known, the electric current passing through the PWAS can be calculated by integrating the electrical displacement D_1 over the entire PWAS surface (Ikeda 1990), i.e.

$$I = j\omega \iint D_1 dA = j\omega \iint \left[(\bar{\varepsilon}_{33}^T - d_{31}^2 \bar{E}_p) \frac{\bar{V}}{h_p} + d_{31} \bar{E}_p \varepsilon_p \right] dxdy, \tag{2.18}$$

where $\bar{\varepsilon}_{33}^T = \varepsilon_{33}^T (1 - i\delta)$ is the complex dielectric constant of the PWAS, d_{31} is the piezoelectric charge constant, and $\bar{E}_p = E_p(1 + i\eta)$ is the complex Young's modulus of the PWAS. δ and η represent the dielectric and mechanical loss factors of the PWAS, respectively. The admittance of the PWAS can then be calculated by solving the integration, i.e.

$$Y = \frac{I}{V} = i\omega w_p l_p \frac{(\bar{\varepsilon}_{33}^T - d_{31}^2 \bar{E}_p)}{h_p} + i\omega w_p d_{31} \bar{E}_p \left[\bar{u}_p(l/2) - \bar{u}_p(-l/2) \right], \tag{2.19}$$

where w_p, l_p, and h_p are the width, length, and thickness of the PWAS. $\bar{u}_p(l/2)$ and $\bar{u}_p(-l/2)$ are the axial displacements of the PWAS at its left and right edge, which can be calculated from the equation (2.17).

2.4 Analytical model validation

The analytical model was validated by comparing the simulated group velocities of the longitudinal and flexural waves with those of the theoretical predictions. Pitch-catch simulation model as demonstrated in section 3.1 has been utilized to validate both the admittance and the pitch-catch models. The group velocities of the simulated waves were computed based on their TOF while the theoretical group velocities were calculated based on the equations given in section 2.2. As shown in figure 2.6, the simulated and theoretical group velocities matched very well for frequencies ranging from 10 to 500 kHz.

2.5 Multi-mode analytical model of bonded PWAS

2.5.1 Parametric studies on the adhesive effect

Based on the analytical formulations described in section 2.3, it is self-evident that the admittance of the bonded PWAS is contributed by the geometry and material constants of the adhesive layer through equation (2.1) and (2.2). Among the three parameters of the adhesive layer (i.e. the shear transfer parameter α, the shear modulus G_a, and the adhesive layer thickness h_a), G_a and h_a always appear together as a lumped term h_a/G_a. Therefore, we can represent the adhesive layer effects using two independent parameters α and h_a/G_a. Parametric studies of their effects on the EMI of the bonded PWAS can then be conveniently carried out.

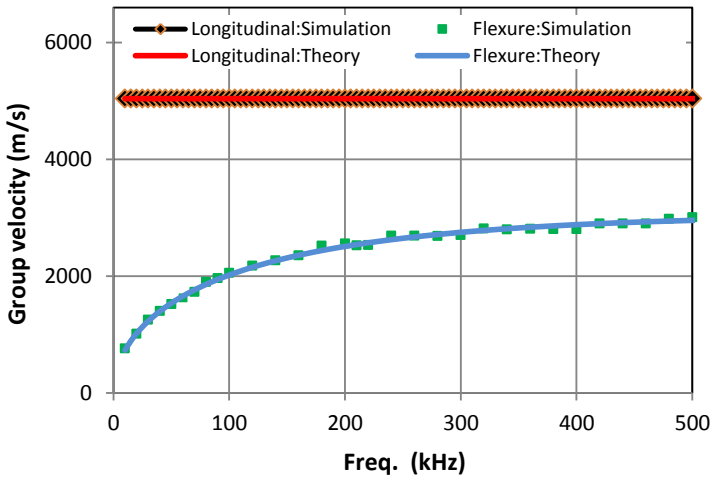

Figure 2.6 Comparison of group velocities between theory and simulation.

First, the effects of α on the PWAS admittance under longitudinal deformations of the structure were studied. Figure 2.7(a) and 2.7(b) show the simulated admittances of the PWAS with α = 0.01 and 1.0, respectively. The thickness-shear modulus ratio h_a/G_a was kept at 0.4 mm/GPa for both cases. For α = 0.01, the PWAS admittance curve displays two dominant resonances: one at 245 kHz and the other at 463 kHz. For α =1.0, the PWAS admittance has a similar resonance at 463 kHz. However, at around 245 kHz, the PWAS admittance curve consists of multiple small peaks instead of one dominant peak. Representing the admittance in time-frequency domain may help to explain the observed admittance differences. Following a procedure similar to that described in section 2.2, the time-frequency relationship of the PWAS admittance for α = 0.01 is obtained and shown in figure 2.7(c). The two resonances appear in red-light blue color. The PWAS "*rings*" after the application of the main bang, i.e. it continues to produce a signal at the resonant frequencies long after the main bang has stopped. The amplitude of the "*ringing*" attenuates with time with the high frequency resonances having higher attenuation rates. In

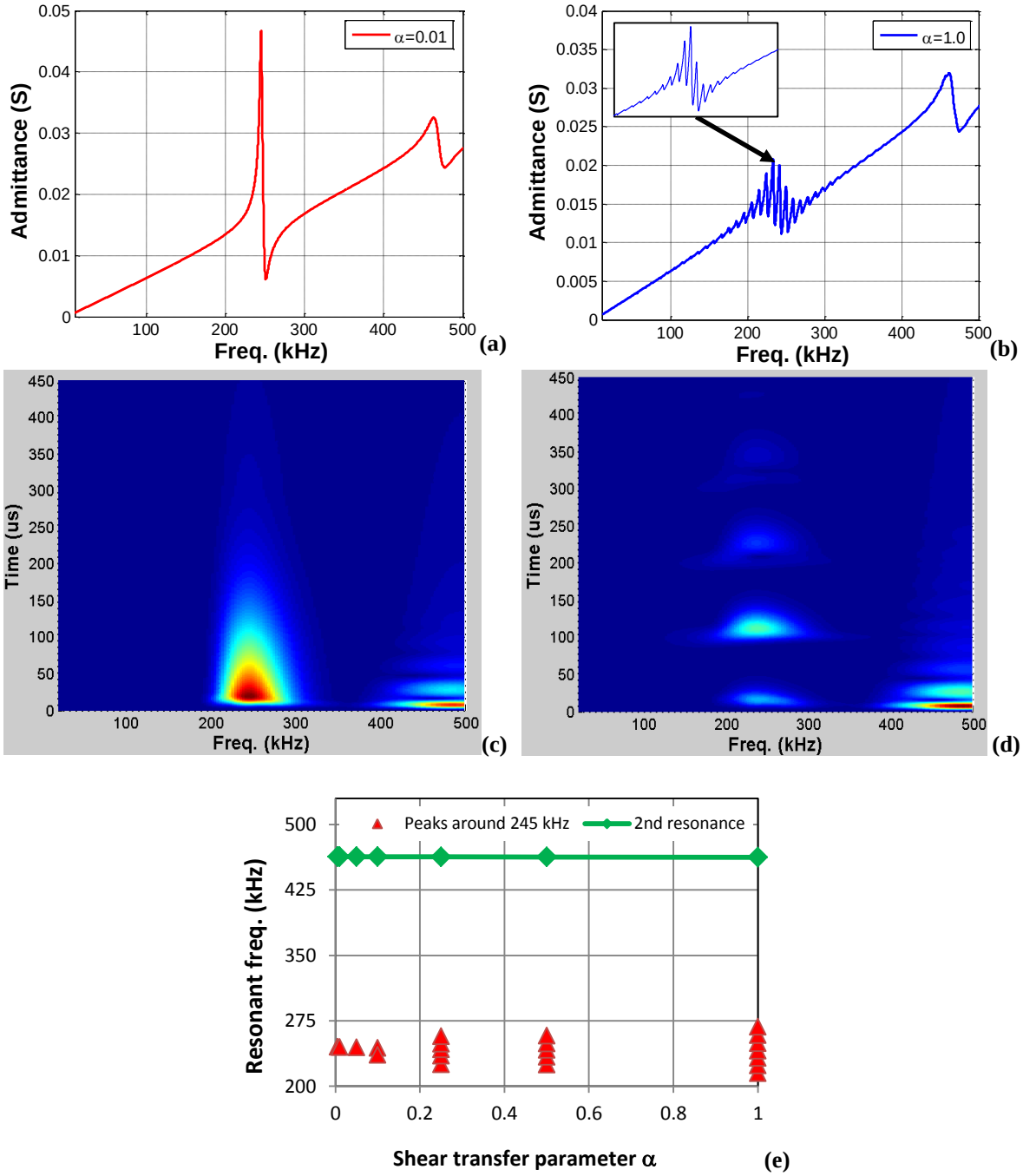

Figure 2.7 Effect of shear transfer constant α on the PWAS resonances when the structure undergoes longitudinal deformations; (a) & (b) admittance spectra for $\alpha = 0.01$ and $\alpha = 1.0$; (c) & (d) corresponding spectrogram; (e) relationship between resonant frequencies and α.

contrast, the PWAS responses for α = 1.0 are very different at 245 kHz as shown in figure 2.7(d). The resonance appears as periodic waves instead of attenuating steadily as that for α = 0.01. This explains why the admittance curve displayed multiple small peaks around this frequency. Based on the longitudinal group velocity, these periodic waves are due to the reflections from the ends of the structure. For example, the TOF of the second wave is 94.6 μs. For a wave speed of 5282.8 m/s, the travel distance is calculated to be 0.5 m, which matches the round-trip distance from the actuator to the end of the structure. According to equation (2.2), α measures how well the shear stresses are transferred from the PWAS to the structure. α = 0.01 means only 1.0% of the shear stress is transferred from the PWAS to the structure. At such a low shear transfer, most of the mechanical energy is not coupled to the structure. Therefore, the ultrasound waves may have dissipated before getting reflected back to the PWAS. On the other hand, α = 1.0 means that the shear stress is completely coupled to the structure. As a result, strong ultrasound waves are excited in the structure, which results in multiple reflections that are eventually coupled back to the PWAS. In return, the PWAS produces a current output that has periodic wave packets in the time domain and appears as multiple small "resonances" in the admittance spectra shown in figure 2.7(b).

To investigate further the effect of α on the resonant frequencies, the peak frequencies of the PWAS admittance curves with different α values are plotted in figure 2.7(e). For α < 0.1, the PWAS admittance has only one dominant resonance at 245 kHz. The number of resonant peaks increased to two when α was increased to 0.1 and increased to 5 when α was increased to 0.25. In addition, the center frequency was reduced from 245 kHz to 243 kHz when α was increased to

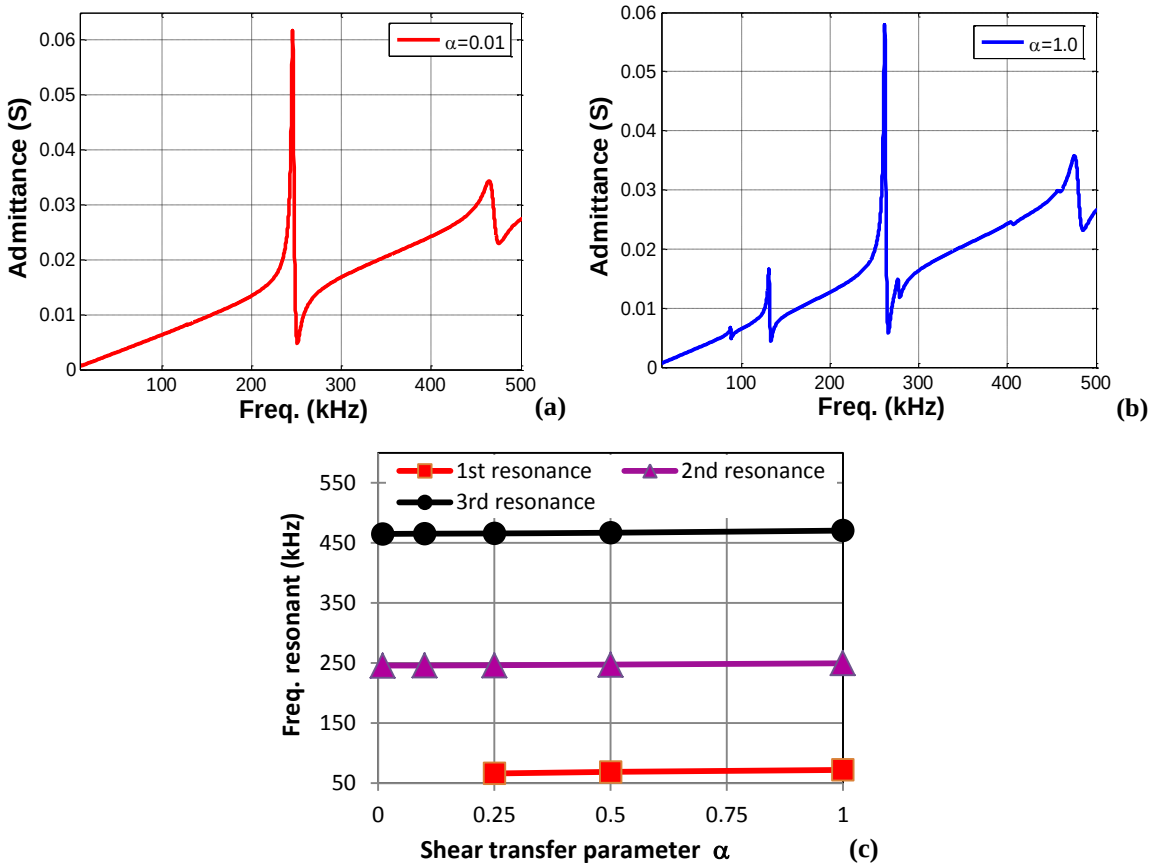

Figure 2.8 Effect of shear transfer constant α on the PWAS resonances when the structure undergoes flexural deformations; (a) & (b) admittance spectra for α = 0.01 and α = 1.0; (c) relationship between resonant frequencies and α.

0.25. The number of resonant peaks remained constant when α was increased to 0.5. However, the center frequency was reduced to 241.6 kHz. At α = 1.0, the total number of frequency peaks are seven. These frequency peaks appear to be centered around 241 kHz. On the other hand, α does not seem to have any effect on the second resonance at 463 kHz.

When the structure deforms in the flexural mode, the PWAS admittance shows similar responses as the longitudinal mode for α = 0.01, as shown in figure 2.8(a). However, for α = 1, the PWAS

admittance displays one additional resonance at 78.8 kHz that is not visible for the longitudinal mode (see figure 2.7(b)). A similar resonance at 81 kHz was also observed in the experiment measurements shown in figure 2.2(a) and 2.2(b). Unlike the longitudinal mode, all the PWAS resonances only have one single dominant frequency peak. The changes of the resonance frequencies with α are shown in figure 2.8(c). The first resonance peak, i.e. the one at 78.8 kHz, appears only when α is larger than 0.25 while the other resonant peaks are present for all α values. When α is small, increasing α increases the resonance frequencies slightly. For large α values, however, the effect of α on the resonance frequency is almost negligible.

The effects of α on the amplitudes of the resonant peaks for both the longitudinal and flexural modes are compared in figure 2.9. When the structure deforms in the longitudinal modes, the amplitude of the 1st resonance reduces steadily with α but the amplitude of the 2nd resonance peak remains constant, as shown in figure 2.9(a). For the flexural modes, the amplitudes of the

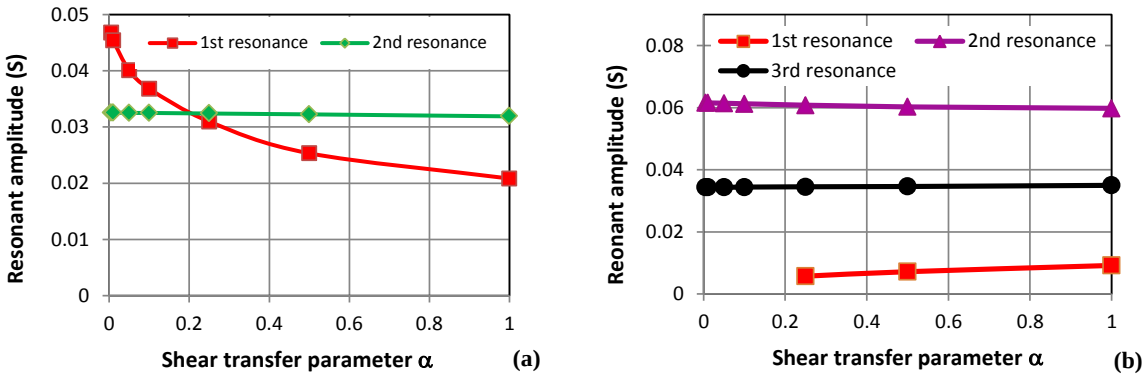

Figure 2.9 Effect of shear transfer parameter α on the amplitudes of the PWAS resonances; (a) longitudinal mode; (b) flexural mode.

1st and 3rd resonant peaks do not change much with α (see figure 2.9(b)). On the other hand, the amplitude of the 2nd resonance increases slightly with α.

The influences of the thickness-shear modulus ratio h_a/G_a on the PWAS admittance are shown in figure 2.10. Since the measured admittances did not display multiple small peaks around the dominant resonances, $\alpha = 0.01$ is chosen for the longitudinal mode. On the other hand, $\alpha = 0.01$

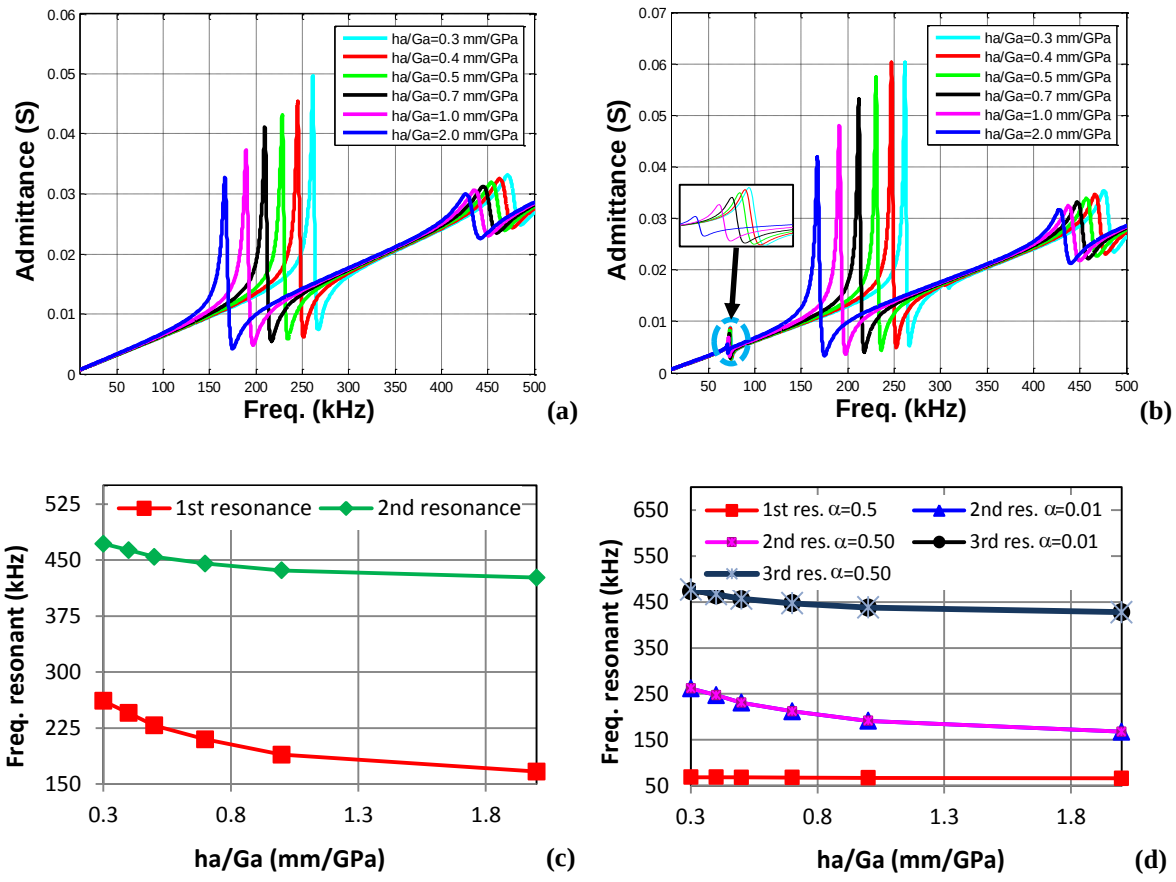

Figure 2.10 (a) & (b) Effects of h_a/G_a on PWAS admittances for longitudinal and flexural modes, respectively; (c) & (d) variations of resonant frequencies with h_a/G_a for longitudinal and flexural modes, respectively.

and 0.5 were selected for the flexural mode to evaluate whether the h_a/G_a effect varies with α. As shown in figure 2.10(a) and 2.10(b), the amplitudes of all resonant peaks decrease with increasing h_a/G_a. For the longitudinal modes, the resonant frequency decrease is more significant for the 1st resonance than for the 2nd resonance, as shown in figure 2.10(c). On the other hand, the 1st frequency of the flexural mode do not change much with h_a/G_a but the 2nd and 3rd resonant frequencies reduce with h_a/G_a. In addition, the effects of h_a/G_a on these two resonances seem to be independent of α.

2.5.2 Matching simulated admittances with measurements

The parametric studies discussed above provide insights for us to adjust the unknown adhesive layer parameters, i.e. the shear transfer parameter α and the shear modulus G_a, to match the simulated admittances with the measurements. The geometric dimensions as well as the material properties of the aluminum structure and the PWAS used for all three specimens are given in Table 2.3. The measured adhesive thicknesses of these three specimens are given in table 1 and were used for the simulations. The Young's modulus E and density ρ of the aluminum alloy 6061-T6 were adopted for the structure. The density ρ and the piezoelectric charge constant d31 of the PWAS were taken directly from the data sheet provided by the PWAS manufacturer (Ceramic 2003). Based on equation (2.19), the Young's modulus Ep of the PWAS has a strong influence on the resonant frequency while the dielectric constant ε^T_{33} and the dielectric loss parameter δ contribute to the capacitance of the PWAS that is responsible for the slope of the admittance curve (Ikeda 1990, Giurgiutiu 2008). Considering that the values given by the manufacturer are for reference only and could have a standard tolerance as high as $\pm$20% (APC

Table 2.3 Geometric dimensions and material constants of the structure and PWAS used in the simulation.

	L (mm)	W (mm)	H (mm)	E (GPa)	ρ (kg/m^3)	η	d_{31} (m/V)	ε^T_{33} (F/m)
Structure	500	10	1.55	68.95	2715	0.01		
PWAS	10	10	0.2	6.2	7800	0.03	-2.1X10^{-10}	4.0X10-8

x/x* : x corresponds to specimen #1 and x* corresponds to specimens #2 and #3.

2014), these three parameters were adjusted to achieve better matches between the simulated and measured admittances. This approach has also been adopted by Annamdas and Soh 2007 and Lim and Soh 2014. The PWAS Young's modulus that produces better matches for the 1st resonant frequency of the flexural mode is Ep = 62 GPa, which is about 7.5% lower than the value of 67 GPa given in the data sheet. The dielectric constant ε^T_{33} and the dielectric loss parameter δ, however, are quite different from those values provided by the manufacturer. This is consistent with the results presented in (Giurgiutiu, 2008), in which the slopes of the simulated admittance curves are quite different from the measured admittances even though the resonant frequencies matched very well. The structural loss constant δ for the structure and the PWAS was taken from Yan et al (2007). After the material properties of the structure and the PWAS were selected, the adhesive layer parameters were adjusted manually to match the resonant frequencies of the simulated and measured admittance curves. Figure 2.11 shows the comparisons between the simulated conductance and susceptance with their experimental counterparts. For all specimens, the multi-mode simulation model was able to capture almost all the dominate resonances, which were missed by the single-mode analytical model published previously (Yang, Lim & Soh 2008a). The shear transfer parameter α and the shear modulus G_a

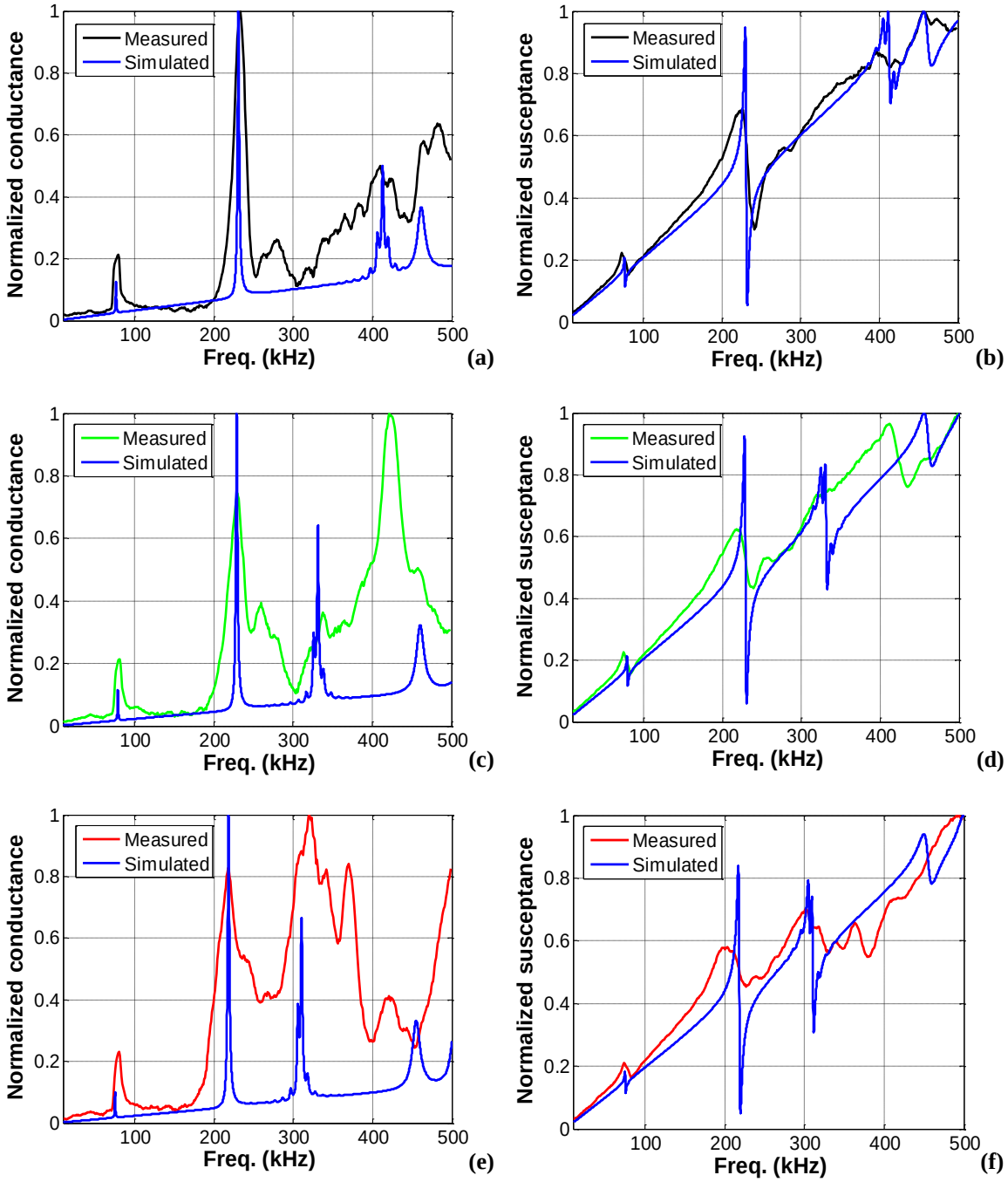

Figure 2.11 Comparisons between measured and simulated PWAS conductance and susceptance; (a & b) specimen #1, (c & d) specimen #2, and (e & f) specimen #3.

that were used to produce the simulation curves in figure 2.11 are listed in Table 2.4. It is worth

noting that two sets of parameters, one set for the longitudinal mode and the other for the flexural mode, have to be used. Since the measured admittances did not show multiple small peaks around the low frequency resonances, a very low α value, i.e. α = 0.05, is assumed for the longitudinal mode of all three specimens. On the other hand, the measured admittance curve showed a small resonant peak at around 81 kHz. Therefore, for the flexural mode, α was chosen to be 0.5 for the first specimen, 0.45 for the second specimen and 0.4 for third specimens. The smaller value of α in the longitudinal mode validates the fact that it is more difficult to excite the longitudinal mode than the flexural mode. Since the shear modulus of the adhesive layer has relatively large influences on the resonant frequencies, it has to be adjusted differently for each specimen to account for the differences in the measured resonant frequencies. In addition, the shear moduli for the two structural modes have to be different to produce the dominant resonances shown in figure 2.1. For all three specimens, the shear modulus G_a for the longitudinal mode is at least twice as high as that for the flexural mode. This could be due to the nonlinear stress-strain behavior of the adhesive material (Christensen 1982). Since the shear strain experienced by the adhesive layer when the structure is under longitudinal vibration is approximately five times more than that of the flexural mode, the shear modulus differences listed in table 3 may be reasonable. The shear modulus estimated here is in the range of 0.1 to 2.5 GPa which matches with those investigated by others (Civjan, Margetis & Reddick 1969, Rabinovitch, Vinson 2002, Sadek 1987). In all the specimens, we were able to match at least three resonant frequencies between the simulated and measured admittances. However, the analytical model was not able to match one small resonance that lies between the second and third resonances for all specimens, which indicates that the simulation model may still miss some

Table 2.4 Bonding layer parameters that matched simulation with measurements.

Specimen	Shear transfer parameter α	Shear modulus G_a (GPa)
#1	0.05/0.5*	1.0/0.24*
#2	0.05/0.45*	1.1/0.39*
#3	0.05/0.4*	1.4/0.5*

#/#*: # is for the longitudinal mode and #* is for the flexural mode.

of the deformation modes of the structure or the PWAS. Since only the longitudinal mode of the PWAS was included in the simulation, the missing resonances could be contributed by the thickness, shear, or flexural mode of the PWAS. According to previous investigations (Yamada, Sakamura & Nakamura 2001, Cao, Zhu & Jiang 1998, Lee, Liu & Ballato 1999), the resonances of the thickness and shear modes of the PWAS have frequencies higher than 2 MHz. Therefore, we suspect that the missing resonance is most likely due to the flexural mode of the PWAS (Huang, Pamphile & Derriso 2008). In the future, the flexural mode of the PWAS should be added to the analytical model.

In this paper, we only focused on adjusting α and G_a to match the PWAS resonant frequencies. The amplitudes of the simulated and measured resonances, especially at high frequencies, still have a large discrepancy. Since the PWAS mechanical loss parameter η has a more significant influence on the resonance amplitude than the adhesive layer parameters, we may need to adopt a frequency-dependent mechanical loss parameters η to achieve better matches of the resonance amplitudes (Yang, Lim & Soh 2008a). In addition, we may achieve better matches if a frequency dependent shear modulus was implemented for the adhesive layer (Zhang et al. 2011, Jin, Wang & Zuo 2009).

2.6 Conclusions

The effects of the adhesive layer on the PWAS admittance bonded on a thin slender structure were investigated experimentally and analytically. We demonstrated that the time-frequency analysis of the broadband ultrasound pitch-catch signal and the PWAS admittance was very helpful in identifying the structural vibration modes associated with the PWAS resonances as well as explaining some of the observed admittance features. The derivation of the multi-mode analytical solution indicated that the effect of the adhesive layer is governed by two parameters, i.e. the shear transfer parameter and the thickness-shear modulus ratio. Parametric studies revealed that the effects of these two parameters depend on the structural vibration modes as well as the resonance orders. Based on the insights gained from the parametric studies, we were able to adjust these two parameters to match the dominate resonance frequencies between the simulated and measurement admittances. In the future, the flexural mode of the PWAS should be incorporated into the analytical model in order to capture the small discrepancies between the simulated and measured PWAS EMIs. In addition, the shear transfer parameter α was assumed to be constant at all locations of the adhesive layer. Due to the nonlinear behavior of the adhesive layer, the displacement dependency of the shear transfer parameter α should be investigated in more details. Since the adhesive parameters were manually adjusted in this study, a parameter identification algorithm may facilitate more accurate determination of the adhesive parameters from the experiment measurements.

CHAPTER 3

EFFECTS OF ADHESIVE THICKNESS ON THE LAMB WAVE PITCH-CATCH SIGNAL USING BONDED PIEZOELECTRIC WAFER TRANSDUCER

3.1 Multi-mode pitch-catch analytical model

Figure 3.1 shows the schematic of an analytical model simulating Lamb waves generated by PWASs instrumented on a slender structure. To excite pure longitudinal and flexural modes, two PWAS actuators are bonded on the top and bottom surfaces of the structure while the sensor is bonded on the top surface of the structure only. The actuators are located at the center of the structure while the sensor is located at a distance of 100 mm to the right of the actuators. As such, the structure is sectioned along the edges of the PWAS resulting three different types of sections: the one with two PWAS actuators bonded on the structure (i.e. the actuator-structure section), the one with a PWAS sensor bonded on the structure (i.e. the sensor-structure section), and the ones without a PWAS (i.e. the structure sections). To simulate the longitudinal vibration of the structure excited by the two PWAS actuators, the schematic of the actuator-structure section loaded with the PWAS-adhesive interfacial shear stress, i.e. τ_p and adhesive-structure interfacial shear stress, i.e. τ_s is shown in Figure 3.2(a). The free body diagram of an infinitesimal element Δx taken from that specimen is shown in Figure 3.2(b), where $P(x,t)$ and $P(x+\Delta x,t)$ are the axial force at the left and right end of the Δx element, and *f(x,t)* is the force

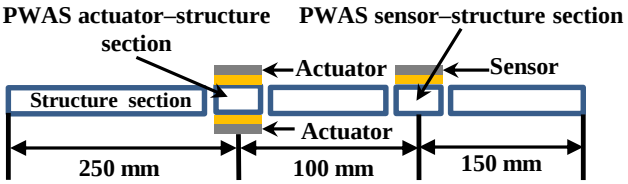

Figure 3.1 Simulation model of a thin slender structure instrumented with two PWAS actuators and a sensor where the instrumented specimen is divided into piecewise homogenous sections.

per unit length acting on the top and bottom surface of the structure. *f(x,t)* is derived from the adhesive-structure interfacial shear stress τ_s using the expression $f(x,t) = \tau_s(x,t) * W_s$, where W_s is the width of the structure. Applying Newton's second law of motion on the infinitesimal element Δx, we get

$$P(x+\Delta x,t) - P(x,t) + 2f(x,t)\Delta x = \rho_s A_s \Delta x \frac{\partial^2 u_s(x,t)}{\partial t^2}. \tag{3.1}$$

Equation (3.1) can further be simplified by applying Taylor's series expansion up to the second term, i.e.

$$\frac{\partial P(x,t)}{\partial x} + 2f(x,t) = \rho_s A_s \frac{\partial^2 u_s(x,t)}{\partial t^2}. \tag{3.2}$$

Using Hooke's law, the relationship between the axial force and the structural displacement can be established, i.e. $P(x,t) = A_s E_s \frac{\partial u_s(x,t)}{\partial x}$, where A_s and E_s are the cross-sectional area and Young's modulus of the structure. By substituting $P(x,t) = A_s E_s \frac{\partial u_s(x,t)}{\partial t}$ into the equation (3.2), we have

$$A_s E_s \frac{\partial^2 u_s(x,t)}{\partial x^2} + 2f(x,t) = \rho_s A_s \frac{\partial^2 u_s(x,t)}{\partial t^2}. \tag{3.3}$$

Substituting shear force per unit length *f(x,t)* by the shear stress τ_s using the expression $f(x,t) = \tau_s(\mathrm{x,t}) * W_s$ into the equation (3.3) results

$$E_s \frac{\partial^2 u_s(x,t)}{\partial x^2} + \frac{2\tau_s(x,t)}{h_s} = \rho_s \frac{\partial^2 u_s(x,t)}{\partial t^2}, \tag{3.4}$$

where h_s is the height of the structure. Similarly, the governing equation for the PWAS actuator can be derived as

$$E_p \frac{\partial^2 u_p(x,t)}{\partial x^2} - \frac{\tau_p(x,t)}{h_p} = \rho_p \frac{\partial^2 u_p(x,t)}{\partial t^2}, \tag{3.5}$$

where E_p, ρ_p, and h_p are the Young's modulus, density, and thickness of the PWAS while τ_p is the shear stress acting at the interface between the PWAS and the bonding layer. The PWAS-adhesive interfacial shear stress τ_p can be calculated from the axial displacements of the PWAS and the structure (Crawley, Lius 1987) as

$$\tau_p(x,t) = G_a \gamma_a(x,t) = G_a \left[\frac{u_p(x,t) - u_s(x,t)}{h_a} \right], \tag{3.6}$$

where G_a and h_a are the shear modulus and thickness of the adhesive layer. Therefore, equation (3.6) represents the coupling between the axial displacement of the PWAS u_p and the axial displacement of the structure u_s. To account for the shear lag effect of the adhesive layer, we introduce a shear transfer parameter α, which is defined as the ratio between the shear stresses at the bottom and top surfaces of the adhesive layer, i.e.

$$\tau_s(x,t) = \alpha \tau_p(x,t). \tag{3.7}$$

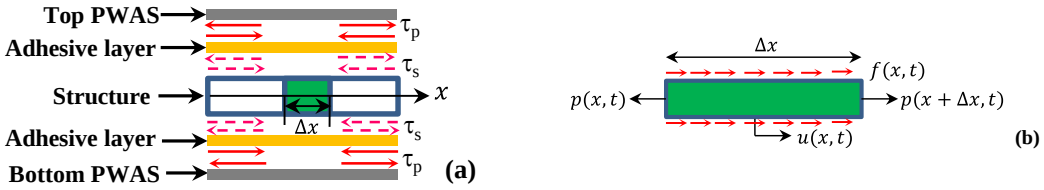

Figure 3.2 (a) Coupling of the PWAS and structure through shear stresses at the PWAS-adhesive layer and adhesive layer-structure interfaces. (b) Enlarged view of an infinitesimal element associated with all the forces acting upon it.

Therefore, $\alpha = 1$ represents a perfect coupling between the PWAS and the structure while $\alpha = 0$ simulates no coupling between these two components. Combining equation (3.4) through (3.7), we obtain a fourth order differential equation that governs the displacement response of the bonded PWAS, i.e.

$$\frac{\mathrm{d}^4 \bar{u}_p}{\mathrm{d}x^4} + A\frac{\mathrm{d}^2 \bar{u}_p}{\mathrm{d}x^2} + B\bar{u}_p = 0, \tag{3.8}$$

in which

$$A = \frac{C_2}{C_1} + \frac{1}{E_s}(\rho_s \omega^2 - \frac{\alpha G_a}{h_a h_s}),\ B = \frac{C_2}{C_1 E_s}(\rho_s \omega^2 - \frac{\alpha G_a}{h_a h_s}) + \frac{\alpha G_a}{E_s h_a h_s C_1},$$
$$C_1 = -\frac{E_p h_a h_p}{G_a}, \quad \text{and} \quad C_2 = 1 - \frac{\rho_p \omega^2 h_a h_p}{G_a}. \tag{3.9}$$

As such, the displacement of the PWAS actuators can be expressed as

$$\bar{u}_p = a_1 e^{\beta_1 x} + a_2 e^{\beta_2 x} + d_1 e^{-\beta_1 x} + d_2 e^{-\beta_2 x}, \tag{3.10}$$

while the displacement of the structure can be expressed as

$$\bar{u}_s = a_1\gamma_1 e^{\beta_1 x} + a_2\gamma_2 e^{\beta_2 x} + d_1\gamma_1 e^{-\beta_1 x} + d_2\gamma_2 e^{-\beta_2 x}, \tag{3.11}$$

where β_i (i =1, 2) are the characteristic roots of the governing equation for actuator-structure section and gamma is expressed as $\gamma_i = C_1\beta_i^2 + C_2$, a_i and d_i are the unknown constants. Similarly, the governing equations of the structure section and sensor-structure section can be found in (Islam, Huang 2014b). The unknown constants in equation (3.10) and (3.11) as well as the unknown constants from the structure and sensor-structure sections can be determined by applying the boundary and/or continuity conditions for each section, as explained in (Islam, Huang 2014b).

Once the displacement of the PWAS is computed using the RMM (Reverberation Matrix Method) technique (Islam, Huang 2014b, Howard, Pao 1998b), the electric voltage acquired through the PWAS sensor can be calculated by integrating the electrical displacement D_1 over the entire PWAS surface (Ikeda 1990), i.e.

$$V = I * R = j\omega R\iint D_1 dA = j\omega R\iint d_{31}\bar{E}_p\varepsilon_p dxdy, \tag{3.12}$$

where d_{31} is the piezoelectric charge constant, $\bar{E}_p = E_p(1+i\eta)$ is the complex Young's modulus of the PWAS, and R is the resistance across the PWAS sensor terminal. Integrating equation (3.12), we obtain the net voltage acquired through the PWAS sensor, i.e.

$$V = i\omega w_p d_{31}\bar{E}_p\left[\bar{u}_p(l/2) - \bar{u}_p(-l/2)\right]R, \tag{3.13}$$

where w_p is the width of the PWAS sensor. $\bar{u}_p(l/2)$ and $\bar{u}_p(-l/2)$ are the axial displacements of the PWAS sensor at its left and right edge, which can be calculated using equation (3.10).

The flexural vibration of the structure excited by the two PWAS actuators can be formulated in a similar fashion. The Timoshenko beam governing equation of the actuator-structure section with shear stresses applied on the top and bottom surfaces can be derived following the Hamilton method (Rao 2007), which results in,

$$\begin{aligned} &-E_s I_s \frac{\partial^2 \phi}{\partial x^2} - k_s A_s G_s \left(\frac{\partial w}{\partial x} - \phi \right) + \tau_s(x) h_s = -\rho_s I_s \frac{\partial^2 \phi}{\partial t^2} \text{ and} \\ &\mathrm{k}_s A_s G_s \left(\frac{\partial^2 w}{\partial x^2} - \frac{\partial \phi}{\partial x} \right) = \rho_s A_s \frac{\partial^2 w}{\partial t^2}. \end{aligned} \tag{3.14}$$

The governing equation for the sensor-structure and structure sections is given in (Islam, Huang 2014b). By applying the boundary and continuity conditions and following the similar procedure as demonstrated above, the pitch-catch voltage signal of the PWAS sensor can then be calculated for the flexural vibration of the structure.

3.2 Parametric studies of adhesive thickness

Parametric studies of the adhesive thickness were carried out to investigate the effects of adhesive thickness on the Lamb wave signals. The geometric dimensions as well as the material properties of the aluminum structure and the PWAS used for the simulation studies are given in Table 3.1. The Young's modulus E and density ρ of the aluminum alloy 6061-T6 were adopted for the structure. The density ρ, piezoelectric charge constant d_{31}, dielectric constant ε_{33}^{T}, and the dielectric loss parameter δ of the PWAS were taken directly from the data sheet provided by the manufacturer (Ceramic 2003). Based on equation (3.13), the Young's modulus E_{p} of the PWAS has a strong influence on the resonance frequency. Considering that the values given by the manufacturer are for reference only and could have a standard tolerance as high as $\pm 20\%$ (APC

Table 3.1 Geometric dimensions and material constants of the structure and PWAS used in the simulation.

	L (mm)	W (mm)	H (mm)	E (GPa)	ρ (kg/m^3)	η	d_{31} (m/V)	ε^T_{33} (F/m)	δ
Structure	500	10	1.55	68.95	2715	0.01			
PWAS	10	10	0.2	72	7800	0.03	-2.1X10^{-10}	2.14X10^{-8}	0.01

2015), the Young's modulus of the PWAS was adjusted to achieve better matches between the simulated and measured pitch-catch signals. The PWAS Young's modulus of E_p = 72 GPa was selected such that it produces better matches for the 1st resonance frequency of the longitudinal mode. This value is about 7.5% more than the value of 67 GPa given in the data sheet. The structural loss constant η for the structure and the PWAS was taken from (Yan et al. 2007). The simulation model is validated first by comparing the simulation results with measurements. As shown in Figure 3.3, the first arrival of the simulated pitch-catch signals, i.e. the tone-burst wave packet that arrives first, agreed well with the measurements for both the longitudinal and flexural modes. Therefore, the peak to peak amplitude of the first arrival was considered throughout this study.

The adhesive layer is represented in the simulation model using three parameters, namely the shear transfer parameter α, the adhesive thickness h_a, and the shear modulus G_a. However, the last two parameters always appear as a compound parameter h_a/G_a, as evidenced by equation (3.6). Therefore, we can perform parametric studies on the effects of the adhesive layer by fixing G_a and varying α and h_a. We excited the PWAS actuator with a 5.5 cycle Hanning windowed tone-burst signal having an amplitude of 2.0 V. Figure 3.4(a) and Figure 3.4 (b) show the effects

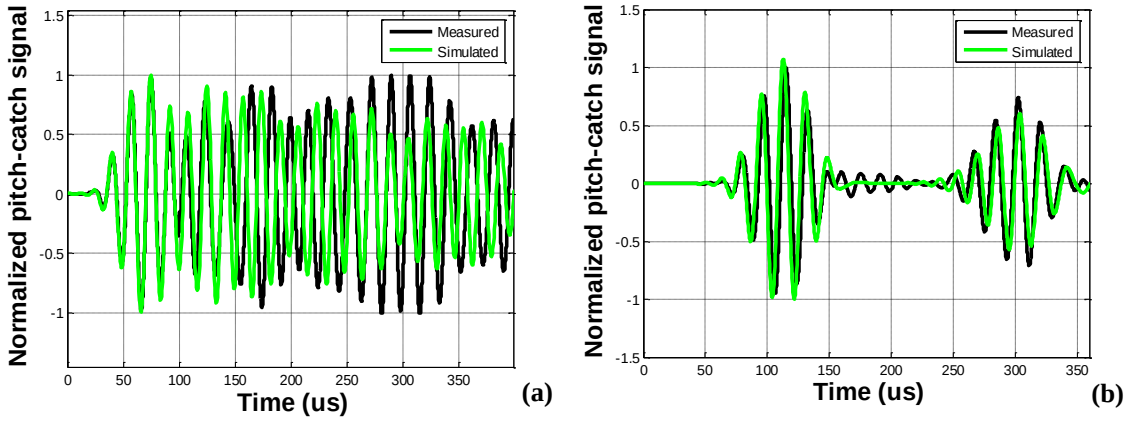

Figure 3.3 Comparison between the measured and simulated pitch-catch signals at 55 kHz; (a) the longitudinal mode pitch-catch signal; and (b) the flexural mode pitch-catch signal.

of adhesive thickness on the longitudinal and flexural mode pitch-catch signals, respectively. For a specific adhesive thickness, the peak to peak amplitudes of the first arrivals were acquired for each excitation frequency ranging from 20 to 500 kHz and are plotted in Figure 3.4(a) and Figure 3.4(b). This procedure is repeated for the various adhesive to PWAS thickness ratios where the adhesive thickness h_a was normalized by the PWAS thickness h_p. For both longitudinal and flexural modes, the shear transfer parameter and the shear modulus of the adhesive layer were assumed to be 1.0 and 0.5 GPa, respectively. As shown in Figure 3.4(a) and Figure 3.4(b), the longitudinal mode pitch-catch signal displays one resonance whereas the flexural mode pitch-catch signal displays two resonance frequencies; one at low frequency, i.e. around 80 kHz; and the other at high frequencies, i.e. more than 200 kHz. The adhesive thickness influences both the resonance frequencies and their amplitudes.

To investigate how the adhesive thickness influences the amplitude of the pitch-catch signals, the resonance amplitudes of the pitch-catch signals were plotted against their corresponding

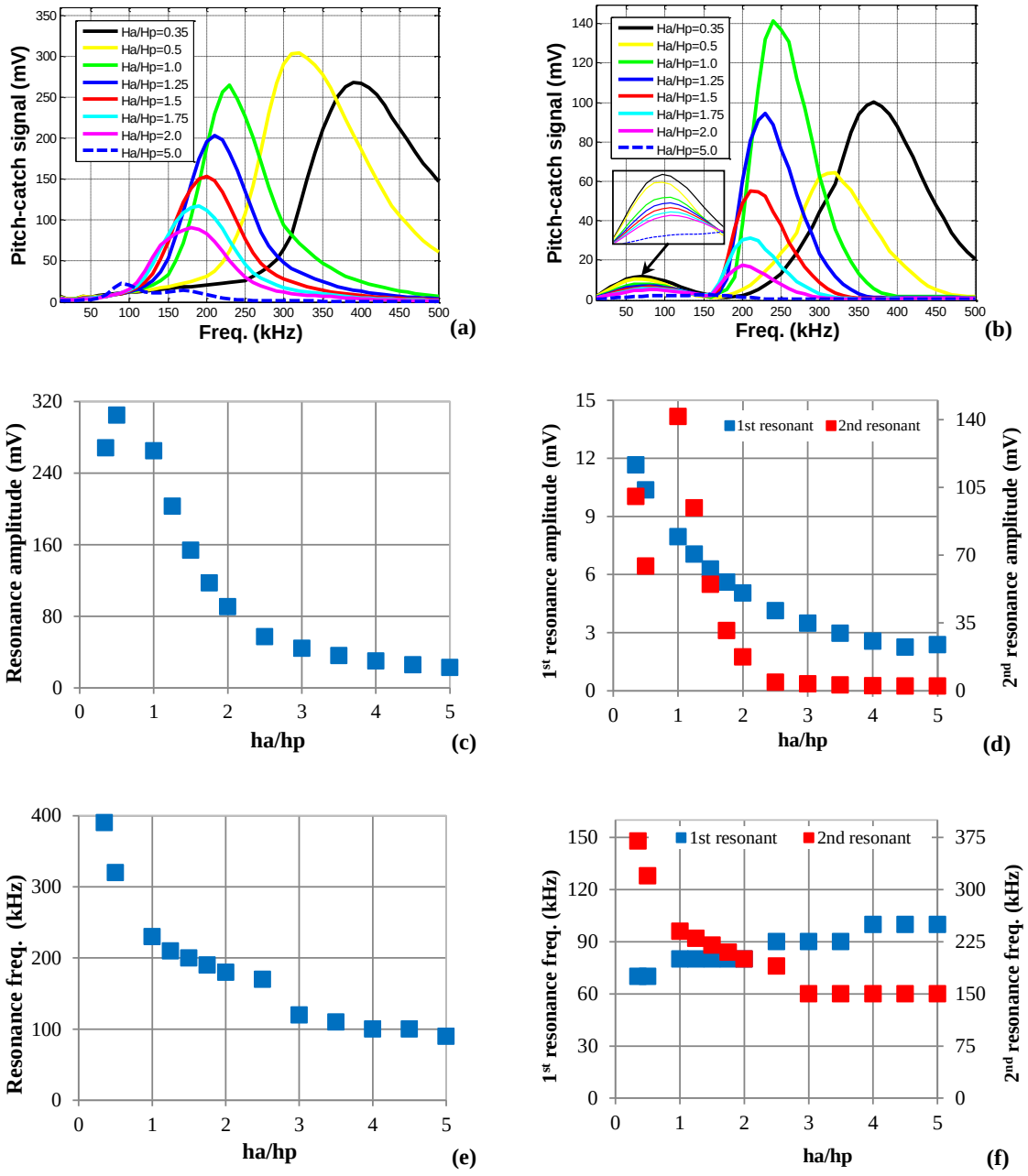

Figure 3.4 Effects of the adhesive thickness on the simulated pitch-catch signals; (a) amplitude-frequency relationship – longitudinal mode; (b) amplitude-frequency relationship – flexural mode; (c) change of resonance amplitude with adhesive thickness – longitudinal mode; (d) change of resonance amplitude with adhesive thickness – flexural mode; (e) change of resonance frequency with adhesive thickness – longitudinal mode; (f) change of resonance frequency with adhesive

adhesive thicknesses in Figure 3.4(c) and Figure 3.4(d). Contrary to common belief that the adhesive layer should be as thin as possible to generate maximal excitations, the simulation predicts that there is an optimal adhesive thickness for the first resonance of the longitudinal mode and the second resonance of the flexural mode. For example, the resonance amplitude of the first longitudinal mode increases with the adhesive thickness for $h_a/h_p < 0.5$ but decreases with the adhesive thickness for $h_a/h_p > 0.5$, as shown in Figure 3.4(c). The amplitude of the second flexural mode has a similar trend except that the amplitude increase for $h_a/h_p < 1.0$ is not monotonic (i.e. the $h_a/h_p = 0.35$ case has a higher amplitude than the $h_a/h_p = 0.5$ case), as shown in Figure 3.4(d). The resonance amplitude of the first flexural mode, however, decreases monotonously with the adhesive thickness. Therefore, the common belief of keeping the adhesive layer as thin as possible may only be applicable for the first resonance of the flexural mode. The resonance frequencies of the pitch-catch signals are plotted against their respective adhesive thicknesses in Figure 3.4(e) and Figure 3.4(f). For both the first longitudinal resonance and the second flexural resonances, the resonance frequencies decrease monotonously with the increase of adhesive thickness, which agrees with previous findings (Islam, Huang 2014b, Ha, Chang 2010). The first resonance of the flexural mode again has a different behavior as the other two resonances. Its resonance frequency increases with the adhesive thickness and the rate of change is much smaller than those of the other two resonances.

In order to investigate how the shear transfer parameter α influences the pitch-catch signal, a parametric study was carried out and the results are shown in Figure 3.5(a) and Figure 3.5(b) for longitudinal and flexural modes, respectively. In this study, the adhesive thickness was assumed to be $h_a/h_p = 1.0$ and the shear modulus of the adhesive layer was assumed to be 0.5 GPa for both

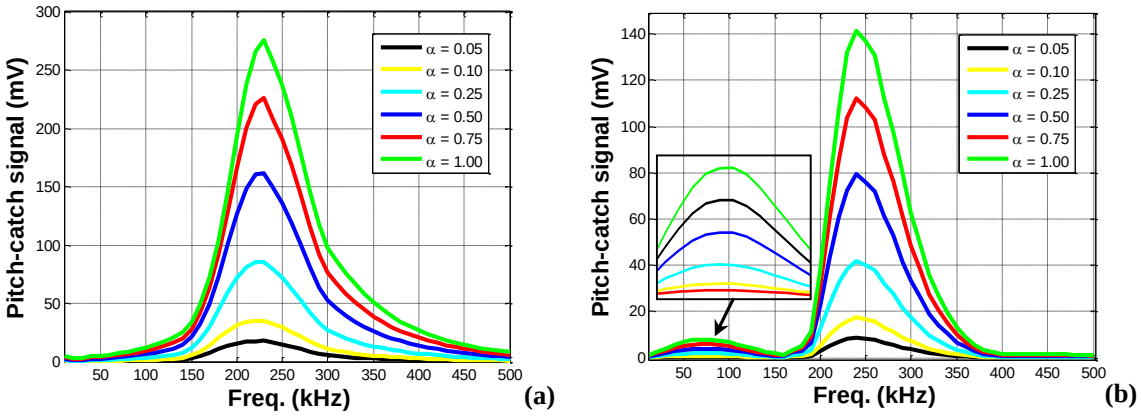

Figure 3.5 Effects of shear transfer parameter α on the simulated pitch-catch signal: (a) longitudinal mode; (b) flexural mode.

modes. $\alpha = 0$ represents zero coupling between the PWAS and the structure while $\alpha = 1$ means the deformation of the PWAS is transferred to the structure without any loss. Not surprisingly, the amplitudes of both modes increased with the shear transfer parameter. On the other hand, the shears transfer parameter α does not have any influence on the resonance frequencies.

3.3 Experimental Validation

We performed a set of experiments to validate the results obtained from the parametric studies. The experimental validation was focused on the adhesive thickness only since it can be controlled precisely (Islam, Huang 2014b). An instrumented specimen that matches the simulation model is shown in Figure 3.6(a). The side view of the actuators-structure section is shown in Figure 3.6 (b). The PWAS transducers (PIC 151, (PI Ceramic 2003) were bonded on the structure using gel type superglue (Loctite 136407) as the adhesive material. Prior to bonding the PWAS transducers on the structure, the impedances of the PWAS transducers were measured to ensure that they have consistent responses. Based on the aforementioned parametric studies,

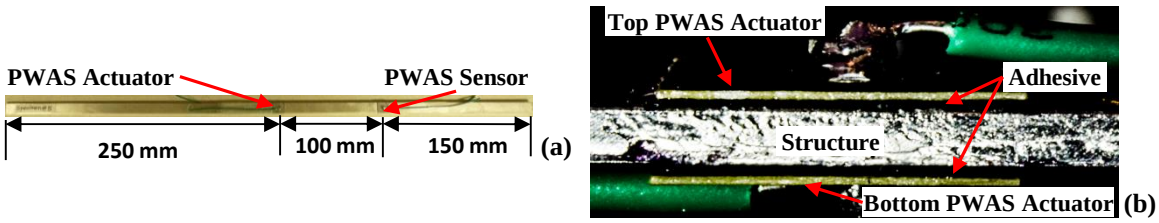

Figure 3.6 (a) A specimen instrumented with PWAS actuators and a PWAS sensor; (b) side view of the PWAS actuators bonded on the top and bottom surfaces of the structure.

the amplitudes of the first longitudinal resonance and the second flexural resonance have maximum values when the adhesive thickness is around the same as the PWAS thickness. Therefore, we have selected the adhesive thicknesses for the samples to be h_a/h_p = 0.35, 1.0, and 1.5, which correspond to adhesive thicknesses of 0.07 mm, 0.2 mm, and 0.3 mm. As shown in table 2, the measured adhesive thicknesses for all the specimens are within 6% of the target adhesive thickness.

To excite the structure with the pure longitudinal vibration, the top and bottom PWAS actuators were excited by a 5.5 cycle Hanning windowed tone-burst signal with a peak to peak amplitude of 2.0 V. The peak to peak amplitude of the first arrival at a given frequency was recorded using an oscilloscope (LeCroy, SDA 760 Zi/0). The peak to peak amplitudes of the pitch-catch signals

Table 3.2 The measured adhesive thicknesses of three different specimens.

Specimens	Thickness (mm)		
	Top Actuator	Bottom Actuator	Sensor
#1	0.074	0.069	0.072
#2	0.205	0.201	0.221
#3	0.297	0.303	0.305

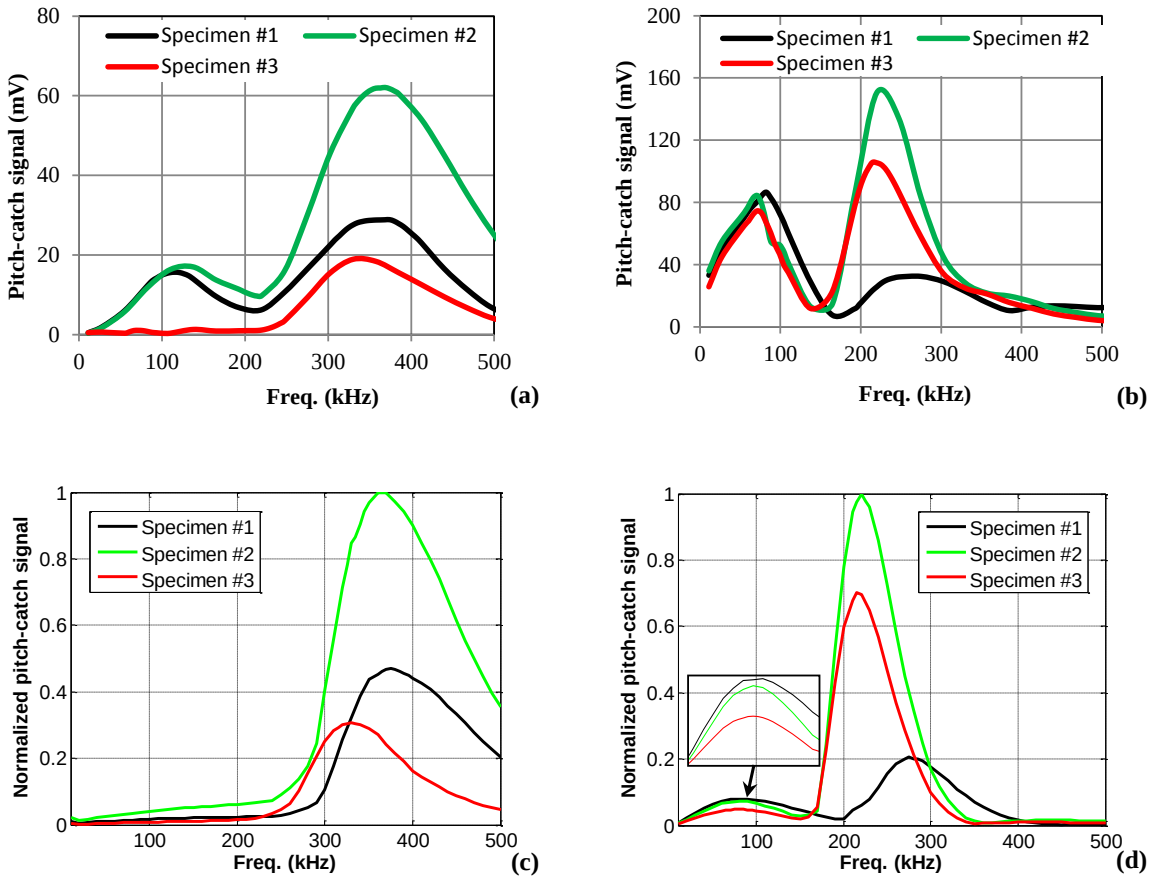

Figure 3.7 Effects of the adhesive thickness on the pitch-catch signal; (a) longitudinal mode-measurements, (b) flexural mode-measurement, (c) longitudinal mode-simulation, and (d) flexural mode-simulation. The shear transfer parameter and the shear modulus of the adhesive layer were adjusted to achieve better matches between the simulation and measurement.

are plotted with respect to the excitation frequencies in Figure 3.7(a). For the longitudinal mode, the resonance frequency reduced from 374 kHz to 368.5 kHz when the adhesive thickness was increased from $h_a/h_p = 0.35$ to $h_a/h_p = 1.0$. Increasing the adhesive thickness further to $h_a/h_p = 1.5$ resulted a much larger frequency drop of about 38.5 kHz, i.e. from 368.5 kHz to 330 kHz. As for the resonance amplitude, specimen #2 produced the largest amplitude of 62.1 mV while

specimen #1 and #3 produces smaller amplitudes of 28.9 mV and 18.9 mV, respectively. Overall, the experimental measurements matched with the simulation predictions quantitatively. However, we did observe one discrepancy between the simulations and measurements. The simulations only displayed one resonance while the measurements had two resonances, albeit the resonances at around 100 kHz have much smaller amplitudes than the ones at around 350 kHz. This discrepancy might be due to the fact that the conditions for the two actuators are not perfectly matched (e.g. the adhesive layer thicknesses are slightly different). As a result, the first flexural mode may be inadvertently excited due to the non-ideal match between these two actuators.

To generate flexural mode pitch-catch signals only, the top and bottom PWAS actuators were excited using 5.5 cycle Hanning windowed tone-burst signals having equal but opposite magnitudes. Figure 3.7(b) shows the flexural mode pitch-catch signals obtained from the three specimens. The flexural mode pitch-catch signal displays two resonances; one just above 200 kHz and the other just below 100 kHz. The frequency of the second resonance reduces with the increase of the adhesive thickness and its amplitude was the largest for specimen #2, which again quantitatively matches with the simulation prediction shown in Figure 3.4(c) and Figure 3.7(d). The frequency of the first resonance, however, decreases with the increase in thickness, which is opposite to the trend predicted by the simulation. On the other hand, the amplitude of the first resonance reduced with the increase in adhesive thickness, which agrees with the simulation predictions.

As discussed before, the simulation studies were carried out by assuming fixed values for the shear modulus and the shear transfer parameter while varying the adhesive thickness. These assumed values may contribute to the aforementioned discrepancies between the measurements and simulations. Therefore, we adjusted these two parameters to achieve better matches between the measurements and simulations. In general, the shear modulus was adjusted manually to match the resonance frequencies while the shear transfer parameter α was adjusted to match the resonance amplitude. The other material properties of the PWAS and the structure were kept the same as those used in the parametric studies. Figure 3.7(c) and Figure 3.7(d) show the simulated pitch-catch signal for the longitudinal and flexural modes, respectively. Clearly, by adjusting the shear transfer parameter α and the shear modulus G_a, we were able to improve the matches between the simulation and the measurement with respect to both the resonance frequency and amplitude. The shear transfer parameter α and the shear modulus G_a that produced the simulation curves in Figure 3.7(c) and Figure 3.7(d) are listed in Table 3.3. It is worth noting that two sets of parameters, one set for the longitudinal mode and the other for the flexural mode, were used. This is because the shear strain experienced by the adhesive layer when the structure is under longitudinal vibration is approximately five times more than that of the flexural mode. Due to the non-linear response of the adhesive material (Christensen 1982), it is reasonable that the adhesive parameters for these two modes are different. Overall, the amplitude of the measured pitch-catch resonance is smaller for the longitudinal mode than for the flexural mode. Similarly, the value of α in the longitudinal mode is smaller than that of the flexural mode as shown in Table 3.3, which means that it is more difficult to excite the longitudinal modes than the flexural modes. Because the shear modulus of the adhesive layer has relatively large influences on the

Table 3.3 Adhesive layer parameters that provide better match between the simulations and measurements.

Specimen	Shear transfer parameter α	Shear modulus G_a (GPa)
#1	0.05/0.80*	0.58/0.25*
#2	0.13/0.86*	1.50/0.35*
#3	0.03/0.59*	1.90/0.5*

#/#*: # is for the longitudinal mode and #* is for the flexural mode.

resonance frequencies, it has to be adjusted differently for each specimen to account for the differences in the measured resonance frequencies. For all three specimens, the shear modulus G_a for the longitudinal mode is at least twice as high as that for the flexural mode. The shear modulus estimated here is in the range of 0.1 to 2.5 GPa which matches with those investigated by others (Civjan, Margetis & Reddick 1969, Rabinovitch, Vinson 2002, Sadek 1987).

One discrepancy that we were not able to address by adjusting the shear modulus and shear transfer parameter is that the amplitudes of the resonances at around 100 kHz relative to the amplitudes of the resonances at high frequencies. For the longitudinal mode, the simulation predicts no resonance at around 100 kHz while the experiment results showed relative small resonances at these frequencies. We suspect that these resonances are actually flexural mode due to the fact that the excitation conditions for the bottom and top actuators are not perfectly symmetric. For the flexural modes, on the other hand, the simulation predicts the resonances at around 100 kHz but their amplitudes are much smaller in comparison with the amplitudes of the resonances at high frequencies. In contrast, the measured amplitudes of the resonances at around 100 kHz are relatively larger. This discrepancy may be contributed by the fact that we assumed the shear modulus and shear transfer parameters to be the same for all frequencies. We may be

able to achieve better matches if a frequency dependent shear modulus was implemented for the adhesive layer (Zhang et al. 2011, Jin, Wang & Zuo 2009). In addition, the simulation model assumes that the PWAS transducer deforms in the in-plane extensional mode only, the out-of-plane bending deformation of the PWAS transducer (Huang *et al* 2008) may need to be considered to achieve better agreements between the simulations and measurements.

3.4 Conclusions

The effects of the adhesive layer on the Lamb wave pitch-catch signal were investigated analytically and experimentally using PWASs bonded on thin slender structures. The analytical formulation of the longitudinal and flexural models indicated that the effect of the adhesive layer is governed by two parameters, i.e. the shear transfer parameter and the thickness-shear modulus ratio. Parametric studies based on the simulation model suggest that there exists an adhesive thickness at which the longitudinal and/or flexural mode pitch-catch signals can be maximized for a given PWAS-structure configuration and this simulation prediction was validated experimentally. The theoretical foundation for this observed phenomenon is not known yet. We suspect that it is related to the impedance matching between the PWAS transducer, the adhesive layer, and the structure. Validating this hypothesis, however, requires an accurate determination of the adhesive parameters. Based on the insights gained from the parametric studies, we were able to adjust the shear transfer parameter and the shear modulus of the adhesive layer to match the pitch-catch resonance frequencies between the simulation and measurement as well as the trend of the resonance amplitudes. In the future, a parameter-identification algorithm may be

developed to facilitate more accurate determination of the adhesive parameters from the measurements.

CHAPTER 4

S-PARAMETERS FOR ULTRASOUND INSPECTION OF COMPOSITE LAP JOINTS

4.1 Experimentation

Figure 4.1 shows the picture of a composite lap joint structure instrumented with two PWASs (PIC 151, 10 mm in length and width, 0.2 mm in thickness). The lap joint structure comprises of two adhesively bonded thin composite structures (Braided composite, www.dragonplate.com) with a length of 250 mm, a width of 10 mm, and a thickness 1.6 mm. The two thin structures were bonded using gel type superglue (Loctite 136407) and the bonding length of the lap joint is 10 mm. Among the two PWASs, PWAS #1 was bonded on the top composite structure while PWAS #2 was bonded on the bottom composite structure. For conventional ultrasound pitch-catch technique, PWAS #1 was selected as the actuator whereas the PWAS #2 was selected as the sensor. It is worth noting that one surface of the composite plate has a smooth coating while the other surface is not coated. We bonded both PWASs on the uncoated surface of the

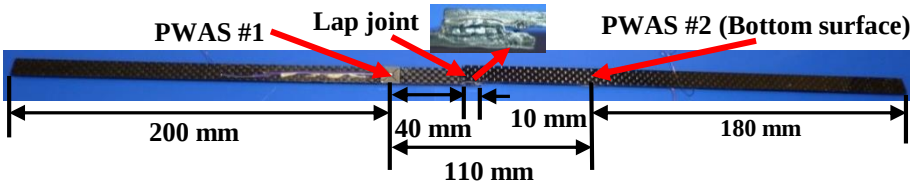

Figure 4.1 A composite lap joint instrumented with a PWAS #1 at 50 mm away from the lap joint free end and a PWAS #2 at 60 mm away from the lap joint free end; the inserted zoomed picture shows the simulated damage of the lap joint adhesive layer.

composites in order to simulate more conventional cases. Since the lap joint was created by bonding two smooth surfaces facing against each other, PWAS #2, which was bonded on the bottom surface of the bottom composite structure, is not visible in Figure 4.1. PWAS #1 was bonded at 50 mm away from the free end of the lap joint region, whereas the PWAS #2 was bonded at 60 mm away from the free end of the lap joint region. To control the damage size of the lap joint adhesive, a wire saw of 0.3 mm diameter was used to cut the adhesive layer by 1 mm and 3 mm.

In this study, we investigated damage detection of the lap joint adhesive using the S21, S11, and admittance parameters. The S-parameters, including the S21 and S11 parameters, were acquired simultaneously using a two-port vector network analyzer (VNA, Rohde & Schwarz, ZVL32) with a frequency resolution of 248 Hz ranging from 10 kHz to 500 kHz. The EMI of the PWAS #1 can then be calculated from the S-parameters using the following equation: $Y = Y_O[(1-S11)(1+S22)+S12S21]/[(1+S11)(1+S22)-S12S21]$, where Y_0 is the characteristic admittance of the VNA (Huang, Bednorz 2014).

4.2 Damage detection using S21 parameter

Figure 4.2 demonstrates the effects of the lap joint damage on the S21 parameters. As shown in Figure 4.2(a), the S21 parameter displayed a dominant resonant at 225 kHz. The lap joint damage reduced the amplitude of this resonant peak but did not shift its spectral location much. In addition, the 1 mm damage only reduced the resonant amplitude by 0.55%. The 3 mm damage, on the other hand, had a much more significant effect on the resonant amplitude; it increased the amplitude by 23.9%. In contrast, the lap joint damage caused not only amplitude

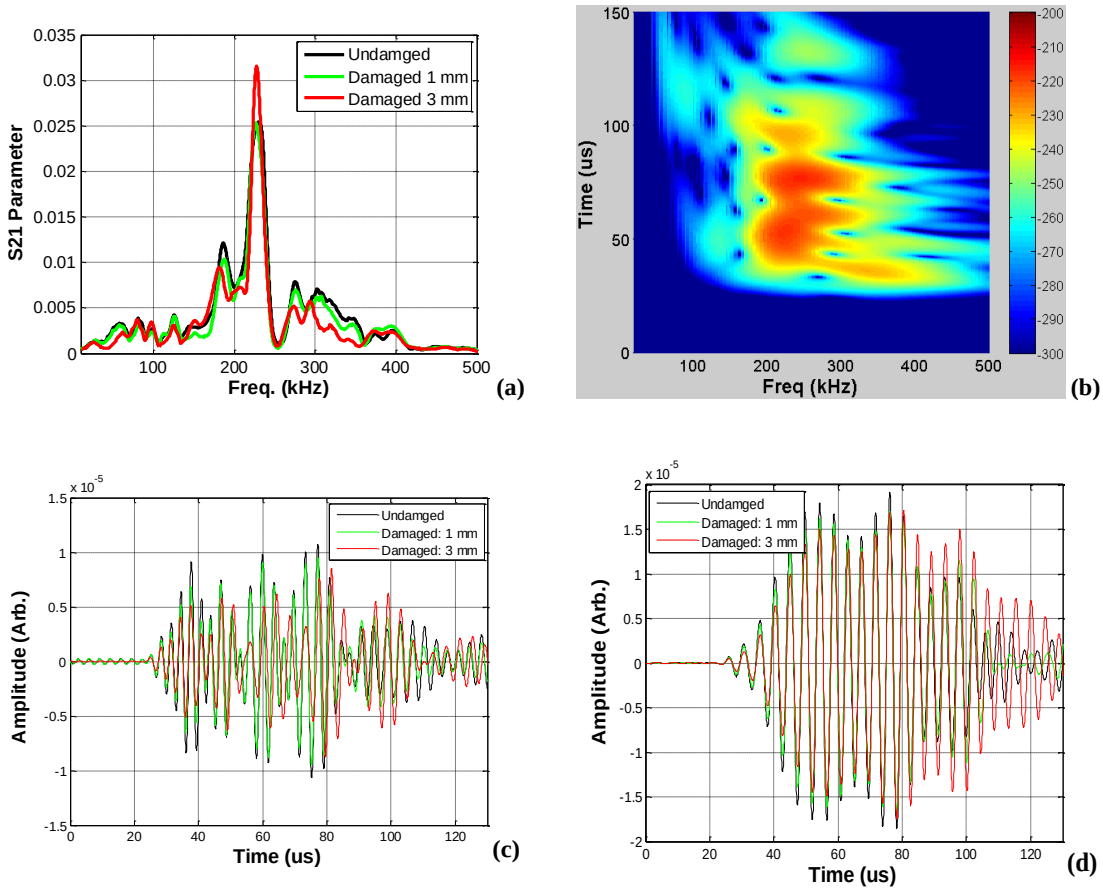

Figure 4.2 Comparison between the damaged and undamaged signals: (a) S21 parameters; (b) time-frequency representation of S21 parameter without damage; (c) narrowband pitch-catch signals at 300 kHz; (d) narrowband pitch-catch signals at 225 kHz.

reduction but also frequency shift of the small resonances, such as the resonant at 300 kHz. Since the S21 parameter also contains phase information, we can perform time-frequency analysis of the S21 parameter to investigate the damage effects in more details. By sweeping the center tone-burst excitation signal and calculating the corresponding ultrasound pitch-catch signal from the S21 parameter, the time-frequency response of the ultrasound pitch-catch system can be constructed (Huang, Bednorz 2014), as shown Figure 4.2(b). This time-frequency-amplitude

plot can be used to determine the wave speeds and the attenuation of the ultrasound signals with different frequency components. For example, we can see that the first arrival of the ultrasound pitch-catch signal has a frequency of between 300-400 kHz while the wave packet at the dominant frequency of 225 kHz appears to be slower waves. In addition, the signal between 300-400 kHz appears to attenuate much more rapidly than those signals around 225 kHz. To further investigate the effects of the damage in the time domain, the narrowband ultrasound pitch-catch signal at 300 kHz and 225 kHz were calculated from the S21 parameter and shown in Figure 4.2(c) and Figure 4.2(d), respectively. For the 300 kHz ultrasound pitch-catch signal, the first wave packet arrives at 22 us. Therefore, its wave speed can be computed to be 5500 m/s (22 us over 110 mm). This fastest wave is presumed to be the symmetric (S0) Lamb mode (Gao 2007, Su, Ye & Lu 2006). The amplitudes of the fast waves, i.e. the ones arrived between 22-70 us, reduced monotonously with the lap joint damage. The trend, however, changed for the signals appeared after 80 us. Since these later arrivals have smaller amplitudes, the amplitudes of the 300 kHz resonant shown in Figure 4.2(a) appear to be dominated by the amplitudes of the fast arriving waves. In contrast, the bulk of the 225 kHz pitch-catch signal shown in Figure 4.2(d) arrived between 40-100 us and attenuated much slower than the 300 kHz pitch-catch signal. Even though the earlier part of the signal, i.e. the ones arrived before 80 us, reduced monotonously with the lap joint damage, the later arriving waves, i.e. the ones arrived after 80 us, increased when the 3 mm lap joint damage was introduced. Since these two parts of signals have comparable amplitudes, the 225 kHz resonant peak in Figure 4.2 (a) appears to be dominated by the later arriving wavers. Based on this analysis, we can draw the conclusion that the effect of the lap joint damage on the ultrasound signals is similar in the time domain for the

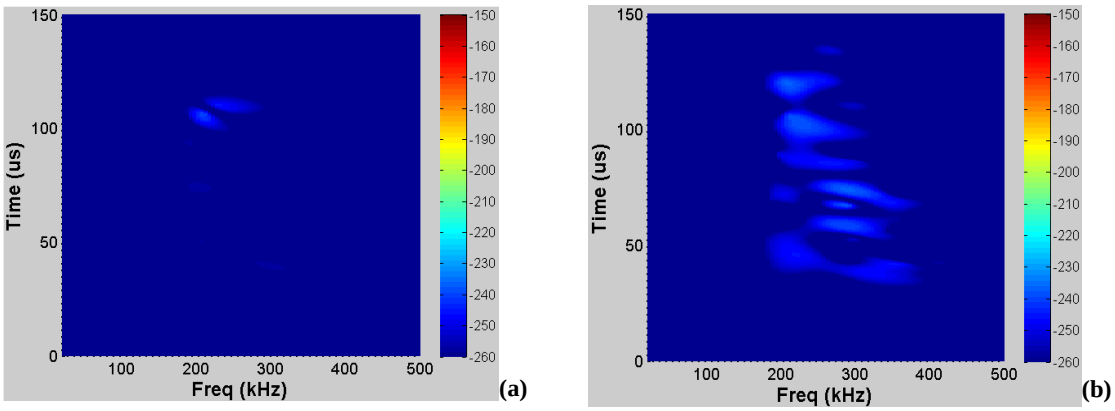

Figure 4.3 Time-frequency-amplitude plots: (a) amplitude difference between the 1 mm damaged and undamaged signals; (b) amplitude difference between the 3 mm damaged and undamaged signals.

225 kHz and 300 kHz pitch-catch signals. The different behavior of the resonants in the frequency domain is due to the different attenuation rate of these two frequency components.

Since the effect of the lap joint damage on the ultrasound signals is frequency dependent as well as time dependent, it is more appropriate to investigate the damage effect using time-frequency-amplitude plots. The differences between the S21 parameters acquired before and after the damage were represented in the time-frequency domain in Figure 4.3. For the 1 mm lap joint damage, the major difference has a frequency of around 225 kHz and occurred only after 100 us. Therefore, a narrowband ultrasound pitch-catch inspection system operating at other frequencies would have missed this small damage. The 3 mm lap joint damage, on the other hand, produced much more prevalent differences, both in frequency and in time. As a result, it should be much easier to be detected than the 1 mm damage. In both cases, the large differences between the damaged and undamaged signals were observed in the later arriving signals than the earlier ones. The physical mechanism underlying these phenomena needs future investigations.

4.3 Damage detection using S11 parameter

The S11 parameter measures the broadband pulse-echo response of the PWAS actuator in the frequency domain. Figure 4.4(a) shows the comparison of S11 parameters between the damaged and undamaged lap joints. Compared to the S21 parameter, the lap joint damage does not seem to have any significant influence on the S11 parameter. For example, the amplitude of the 225 kHz resonant only changed slightly for the damaged cases, as shown in the zoomed image. This is because the S11 parameter contains both the pulse and the echo signal. Since the pulse signal

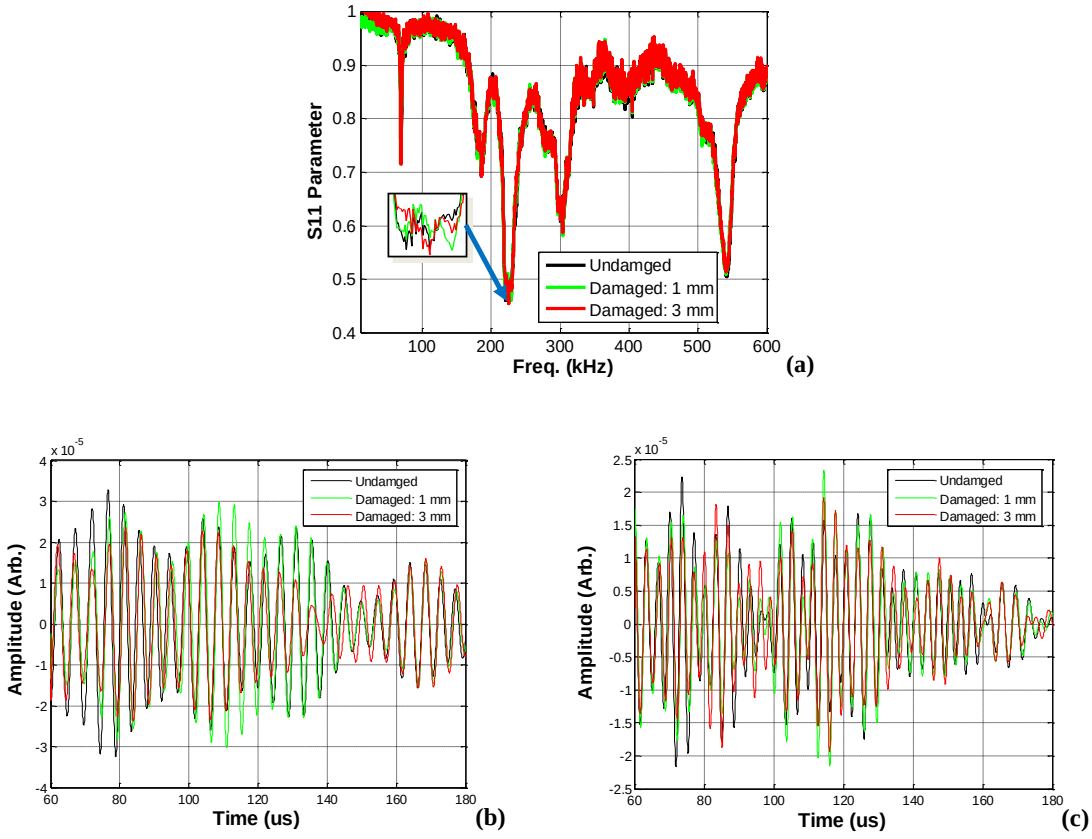

Figure 4.4 (a) Comparison of S11 parameter between the damaged and undamaged lap joints and narrowband ultrasound pulse-echo responses: (b) 225 kHz; and (c) 300 kHz.

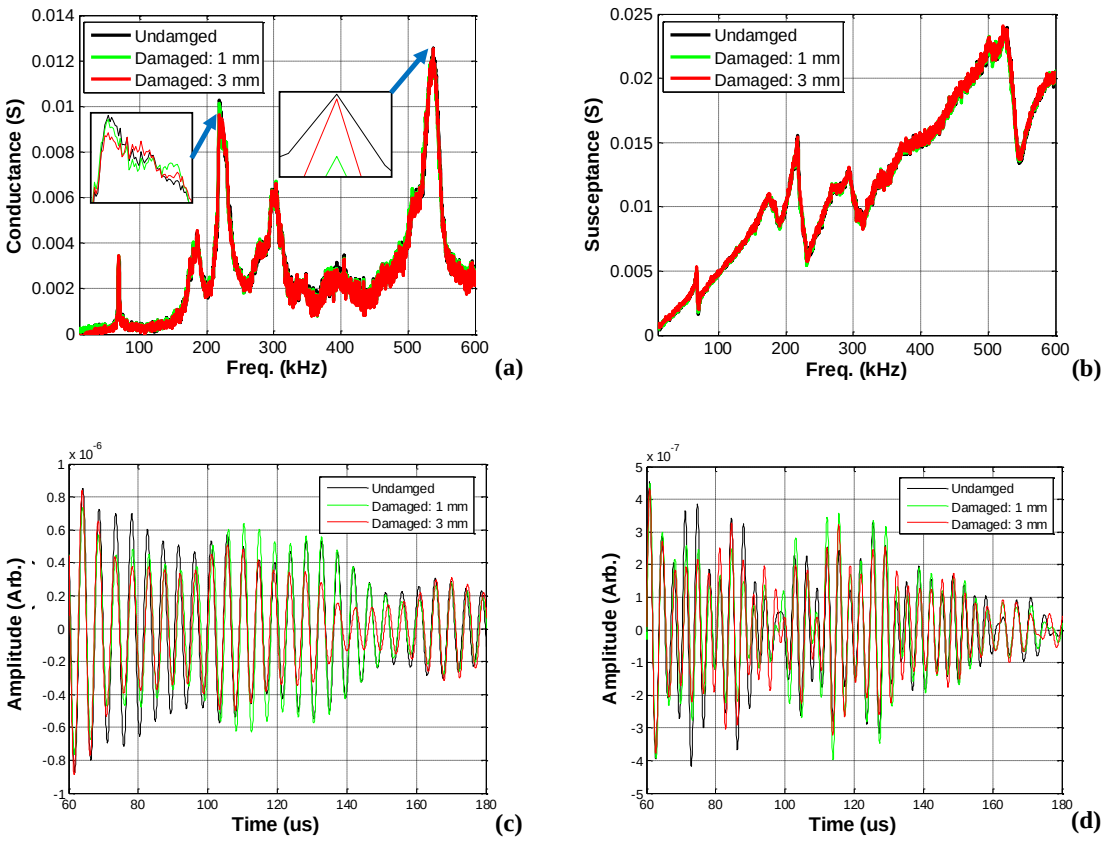

Figure 4.5 Comparison of admittance constituents between the damaged and undamaged lap joint composites: (a) conductance; and (b) susceptance. Comparison of narrowband pitch catch signals between the damaged and undamaged composites: (c) 225 kHz; and (d) 300 kHz.

is much larger than the echo signal, it dominates the S11 parameter. This also explains why the S11 parameter is insensitive to the lap joint damage because the lap joint damage only influences the echo signal. In order to reveal the damage-induced signal changes, the S11 parameter was converted to the time-domain and the pulse signal was removed by time gating. As shown in Figure 4.4(b) and Figure 4.4 (c), the echo signals at 225 kHz and 300 kHz, which were extracted from the S11 parameter by removing the pulse signal, displayed significant differences between

the damaged and undamaged cases. The damage effects on the fast arriving and slow arriving waves are different and are consistent with what we observed in the narrowband pitch-catch signal. Therefore, the S11 parameter may offer a redundant measurement to validate the S21measurement and help reduce false alarms.

4.4 EMI-based damage detection

The EMI of PWAS #1 was calculated from the S-parameters and the comparisons of conductance and susceptance between the damaged and the undamaged lap joint composites are shown in Figure 4.5(a) and Figure 4.5 (b), respectively. Both the conductance and susceptance do not show drastic changes of either amplitude or frequency with the lap joint damage. This is again misleading because the EMI data, similar to the S11 parameter, also contains the pulse signal. Therefore, it should be investigated in the time domain to reveal the damage effect. As shown in Figure 4.5(c) and Figure 4.5 (d), the 225 kHz and 300 kHz time domain signals extracted from the EMI data, with the pulse signal removed, clearly shows that the lap joint damage has a significant influence on the time-domain EMI signal. In addition, the damage effects on the EMI signal are very similar to those on the S11 parameter. More detailed investigations are needed to understand the correlations between EMI, S11, and S21 parameters, which may reveal the physical mechanisms underlying the damage effects.

4.5 Conclusions

We investigated the S-parameters for damage detection of composite lap joint. The S-parameters can be measured over a wide frequency bandwidth using a compact device. We have demonstrated that small lap joint damage can be reliably detected based on the time-frequency

analysis of the S-parameters. In addition, three different ultrasound signals, i.e. the pitch-catch, pulse-echo, and impedance signals, can be simultaneously extracted from the S-parameters. Correlating these three sets of signals may help reduce false alarm and increase detection confidence.

CHAPTER 5

DETECTING SEVERITY OF DELEMINATION IN A LAP JOINT USING S-PARAMETERS

5.1 Principal of operation

Figure 5.1 shows the diagram of a lap joint structure instrumented with two PWaTs and how the Lamb wave generated by PWaT #1 interacts with the lap joint section. When the Lamb wave encounters the left edge of the lap joint, it is partially reflected and partially transmitted (Lowe, Challis & Chan 2000, Puthillath et al. 2008, Song et al. 2003). The reflected wave re-tracks its path and is the first echo signal received by PWaT #1. Traveling in the lap joint section, the transmitted Lamb wave is coupled from the bottom structure to the top structure. Upon encountering the right edge, a part of this transmitted wave exits the lap joint and is received by PWaT #2 as the first arrival pitch-catch signal. The remaining wave is reflected and travels

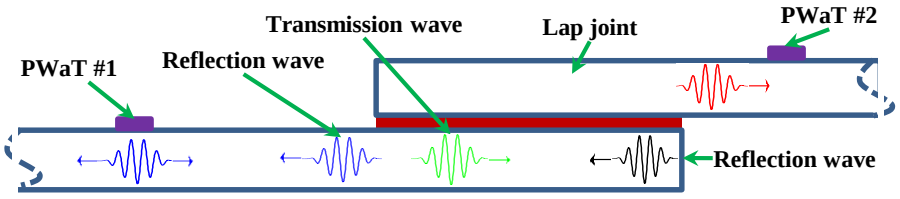

Figure 5.1 Interaction between the Lamb wave and the lap joint. A part of the Lamb wave generated by PWaT #1 is reflected at the edges of the lap joint and detected by PWaT #1 as the echo signals while the other part transmits through the lap joint and is received by the PWaT #2 as the pitch-catch signal.

back to the left edge, at which a part of the wave exits the lap joint and produces an additional echo signal received by PWaT#1. The rest of wave is again reflected back to the lap joint section. This back and forth reflection at the two edges of the lap joint can last for several rounds until the Lamb wave gradually dies out. The Lamb wave generated by PWaT #2 experiences similar process. Therefore, both PWaT #1 and PWaT #2 receive echo signals that have interacted with or traveled in the lap joint. These echo signals can thus be exploited for detecting the lap joint damage and its severity. Let us consider a case of delamination at the left edge of the lap joint. The delamination reduces the coupling distance between the bottom and top structures. As a result, less ultrasound energy is coupled from the bottom to the top structure, which leads to a reduction in the amplitude of the pitch-catch signal. In return, more energy is reflected back to PWaT #1, producing an increase in the amplitude of the echo signal. In addition, since the first echo is generated at the location where the adhesive layer joins the top and bottom structures, the delamination essentially shifts the left edge of the lap joint to the right. As a result, the time-of-the-flight of the first echo signal received by PWaT #1 should increase with the delamination length. Moreover, the delamination changes the boundary condition of the bottom structure and thus may influence the resonant characteristics of PWaT #1. In contrast, the Lamb wave generated by PWaT #2 encounters the right edge of the lap joint first and then interacts with the delamination. As a result, it is expected that the pulse-echo signal received by PWaT #2 may not be as sensitive as that received by PWaT #1. The difference between the responses of the two PWaTs, therefore, may provide information about which side of the lap joint is damaged.

5.2 Specimen configurations

Figure 5.2(a) shows the instrumented specimen in which two long slender aluminum structures were bonded together using a lap joint of 25 mm in length. The two aluminum structures have a length of 500 mm, a width of 10 mm, and a thickness of 1.6 mm. Two PWaTs (PI Ceramic, PIC 151, 10 mm in length and width, 0.2 mm in thickness) were bonded at the center of each structure. These two structures were joined using an adhesive material (Loctite 136407). The important locations on the specimen were numbered in order to demonstrate the traveling path of the Lamb wave. Delamination was introduced to the left side of the lap joint section by removing the adhesive material using a diamond wire. The diameter of the diamond wire is 0.2 mm while the lap joint adhesive thickness is 0.6 mm. Delamination lengths of 10 mm and 15 mm were introduced sequentially. As the delamination progresses, location #2 moves to the right toward location #3. To acquire the *S*-parameters, port #1 and #2 of a Vector Network Analyzer (VNA) (Rohde and Schwarz, ZNB 8) were connected to the terminals of PWaT #1 and PWaT #2, respectively, as shown in Figure 5.2(b). The *S*-parameters were acquired by sweeping the interrogation frequency from 10.0 kHz to 1.0 MHz with an increment of 248 Hz. The bandwidth

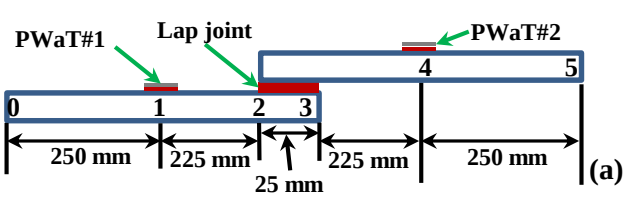

Figure 5.2 (a) Configuration of a lap joint specimen with detailed dimensions; (b) experimental set up: lap joint structure instrumented with two piezoelectric wafer active transducers; one at the left and the other at the right side of the lap joint. The transducers are connected to a vector

resolution of the VNA was selected to be 200 Hz in order to ensure the signal acquisition up to 500 μs without aliasing (Huang, Bednorz 2014).

5.3 Time-frequency analysis of *S*-parameters

Figure 5.3(a) shows the S_{11} parameter acquired before the delamination was introduced to the lap joint. The S_{11} parameter displays six resonances at 78, 220, 266, 350, 400, and 465 kHz. The small return losses at these resonances indicate that most of the electric energy supplied to PWaT #1 was converted to mechanical energy. The time-frequency-amplitude (TFA) plot, which represents the amplitude of the time domain pulse-echo signal as a function of frequency and time, was generated from the S_{11} parameter using the procedure described in appendix A and is

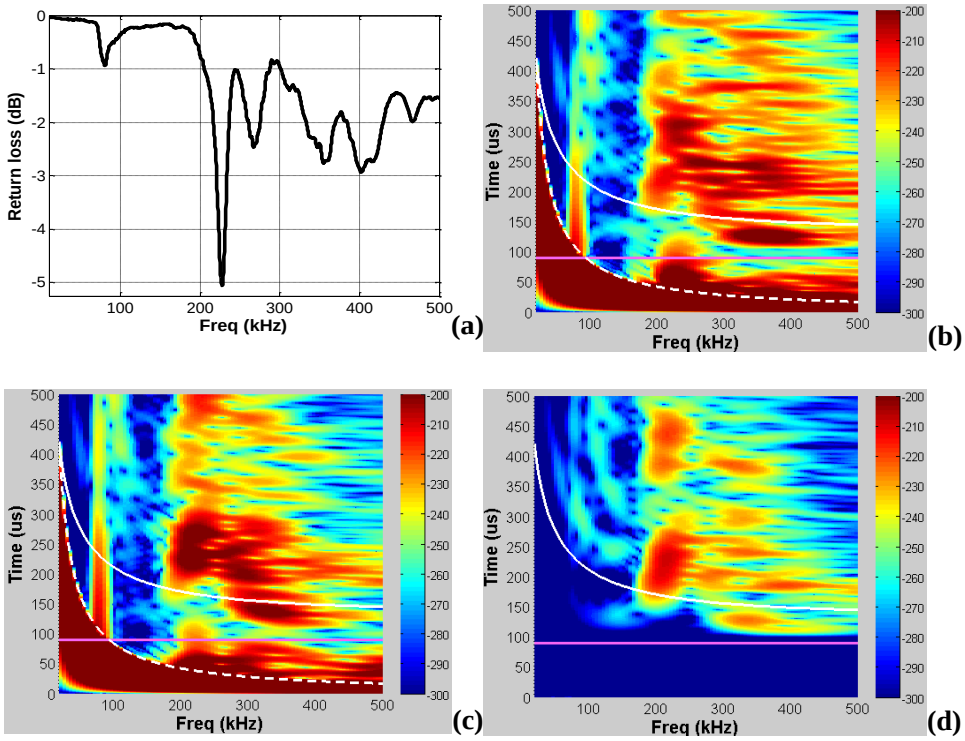

Figure 5.3 S-parameters of the undamaged specimen; (a) frequency-domain S_{11} parameter and time-frequency-amplitude plots of (b) S_{11}, (c) S_{22}, and (d) S_{21} parameters.

shown in Figure 5.3(b). A Hanning windowed 8.5 cycle tone-burst signal was used as an excitation signal to ensure that its narrow bandwidth can separate the 220 kHz resonance from the other resonances. The high electro-mechanical energy conversion at the resonances excited strong Lamb waves at the resonant frequencies. As a result, the echo signals at the resonant frequencies have large amplitudes and appear as red "blobs" in Figure 5.3 (b).

As explained in appendix A, the time domain pulse-echo signal can be divided into three different signals, i.e. the excitation, resonant, and echo signals. The end of the excitation signal is marked with a dotted white line in Figure 5.3 (b). Starting right after the end of the excitation signal, the resonant signal either exhausts before the arrival of the echo signal or persists even after the arrival of the echo signal. The arrival time of the echo signal is determined by the wave speed at a specific frequency and the distance between the transducer and the structural discontinuity that generates the echo. In our case, the first echo received by PWaT #1 is generated by the left end of the lap joint. Therefore, the round trip distance traveled by the echo signal is 450 mm. The wave speed can then be calculated by dividing the round trip distance with the arrival time of the first echo, based on which the structural modes associated with each resonance can be identified. The symmetric and ant-symmetric Lamb wave modes correspond to the longitudinal and flexural vibration modes of the structure. The theoretical speed of the longitudinal wave is independent of the frequency, which can be calculated as $\sqrt{E/(1-\nu^2)/\rho}$, where E is the Young's modulus, ν is the Poisson's ratio, and ρ is the material density. In contrast, the theoretical speed of the flexural wave in a Timoshenko beam is frequency dependent, which can be calculated using the fourth order differential governing equation given in (Rao 2007). Based

Table 5.1 Geometric dimensions and material constants of the structure used for wave speed calculation.

W (m)	h (m)	I (m^4)	A (m^2)	E (GPa)	ν	ρ (kg/m^3)	k_s
$10X10^{-3}$	$1.6X10^{-3}$	$3.4X10^{-12}$	$1.6X10^{-5}$	68.95	0.3	2715	$\pi^2/12$

on the parameter values given in table 1, the time-of-flight (TOF) of the longitudinal wave traveling a distance of 450 mm is calculated to be 89 μs, as represented by the horizontal solid magenta line in Figure 5.3 (b). On the other hand, the TOF of the flexural wave is marked by the white solid line. For the 78 kHz resonance, the resonant signal overlaps with the longitudinal echo and prevails even after the arrival of the flexural mode echo signal. Therefore, it is impossible to separate the resonant signal from the echo signals. While the resonant signals of the 220 kHz and 266 kHz resonances extend beyond the arrival time of the longitudinal echo signal, it seems that PWaT #1 only excited flexural waves at these two frequencies. As such, the resonant signal and the echo signal can be separated. While the resonances at 350, 400, and 465 kHz excited the longitudinal waves, we can still separate the resonant signal from the echo signals since the duration of the resonant signals are relatively short due to the broadband nature of these resonances.

The TFA plot of the S_{22} parameter acquired from PWaT #2 is similar to that of the S_{11} parameter, as shown in Figure 5.3 (c). Due to a small variation on the adhesive layer thickness, Figure 5.3(c) is slightly different from Figure 5.3 (b) but yields the same conclusions as those discussed above. The analysis of the Lamb wave modes is further validated by the TFA plot of the transmission S_{21} parameter shown in Figure 5.3 (d). The magenta and white lines represent the TOF of the

longitudinal and flexural waves for a travel distance of 475 mm between PWaT #1 and PWaT #2, respectively. The resonances appear in Figure 5.3 (d) are similar to those seen in Figure 5.3 (b) and Figure 5.3 (c). Based on the TOF of the S_{21} parameter resonances, the 78 and 220 kHz resonances excite the flexural modes and the resonances above 300 kHz excite both the longitudinal and flexural modes, which agrees well with our identification of Lamb wave modes using the reflection *S*-parameters, i.e. the S_{11} and S_{22} parameters.

5.4 Detecting damage severity based on the reflection *S*-parameters

The S_{11} parameters acquired before and after the introduction of the delamination are compared in Figure 5.4(a). The insets show zoomed-in views of the resonance valleys at different frequencies. The return loss at the 78 kHz resonance reduced first when a 10 mm delamination was introduced but increased as the delamination length was increased from 10 mm to 15 mm. The return loss of the 220 kHz resonance decreased monotonically with the increase of delamination length. On the other hand, the return losses at the 266, 350, 400, and 465 kHz resonances remained almost constant when the lap joint damage length was 10 mm but decreased with the further increase of the damage length to 15 mm.

In order to understand why the return losses of the resonances responded to the delamination differently, the differences between the TFA plots of the S_{11} parameter obtained from the damaged and undamaged lap joint are plotted in Figure 5.4 (b) and Figure 5.4 (c). For the 78 kHz resonance, the lap joint delamination had a strong influence on the resonant signal but did not have much influence on the echo signal. The change in the return loss of this resonance is therefore dominated by the resonant signal, which did not show a monotonous trend with respect

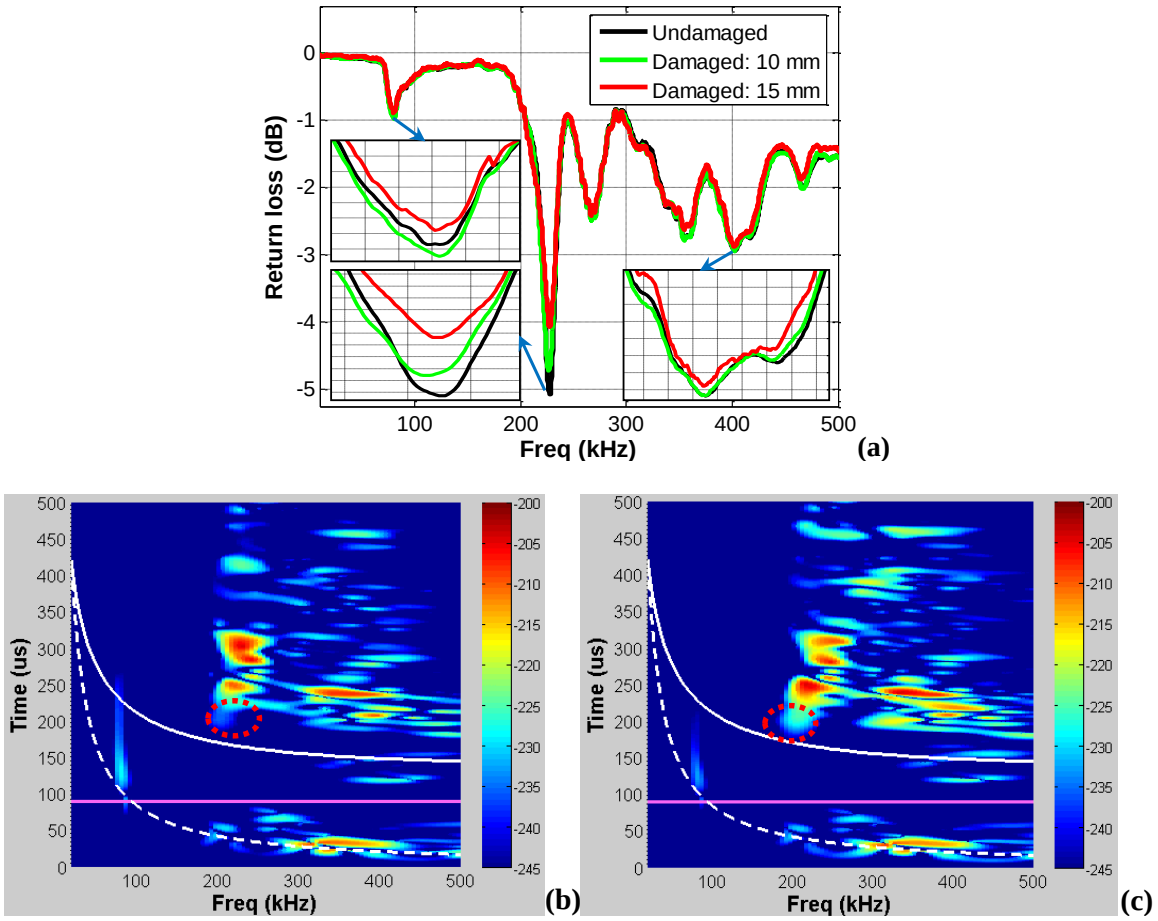

Figure 5.4 Effects of delamination on the S_{11} parameters; (a) comparison of the S_{11} parameters before and after the introduction of the delamination; (b) amplitude difference of the time-domain pulse-echo signals between the undamaged specimen and the specimen with a 10 mm delamination; and (c) amplitude difference of the time-domain pulse-echo signals between the undamaged specimen and the specimen with a 15 mm delamination.

to

the delamination length. In comparison, the influence of the delamination on the resonant signal of the 220 kHz resonance was much smaller. Consequently, the return loss change at this resonance is dominated by the flexural mode echo signal, whose amplitude increased monotonously with the delamination length, as shown in Figure 5.4 (b) and Figure 5.4 (c). For

the resonances at frequencies higher than 300 kHz, the delamination significantly affects the amplitudes of the resonant signals, especially near the end of the excitation phase. This influence, however, dies out rapidly as time progresses. At these resonances, both the longitudinal and flexural modes were excited and the corresponding echo signals responded to the delamination differently; the amplitude change of the longitudinal mode echoes was not monotonous with the increase of the delamination length while the amplitude of the first arrival flexural mode echoes increased monotonously with the delamination length. Since the return loss changes at these resonances are contributed by the resonant signal as well as the longitudinal and flexural model echo signals, they are sensitive to the delamination length but the trend is not monotonous. The TFA difference plots shown in Figure 5.4 (b) and Figure 5.4 (c), therefore, enable us to evaluate the effects of the delamination on the resonant characteristics of the PWaT as well as the resulting echo signals. Based on this analysis, we can draw the conclusion that the resonant characteristic of PWaT #1 is least sensitive to the delamination at the 220 kHz resonance. In addition, Figure 5.4 (b) and Figure 5.4 (c) also show that the longitudinal mode echo signal is sensitive to the presence of the delamination but is insensitive to the progression of the delamination. Therefore, only the 220 kHz resonance is suitable for detecting the severity of delamination since the resonant characteristics of the PWaT is insensitive to the delamination and only the flexure mode was excited at this resonance.

The effects of the delamination on the pulse-echo signal can be investigated in more details by extracting the time-domain pulse-echo signal from the S_{11} parameter using a tone-burst excitation signal centered at 220 kHz. Figure 5.5(a) shows such signals before and after the introduction of the delamination. Following the excitation signal ending at 38.6 μs, the resonating PWaT

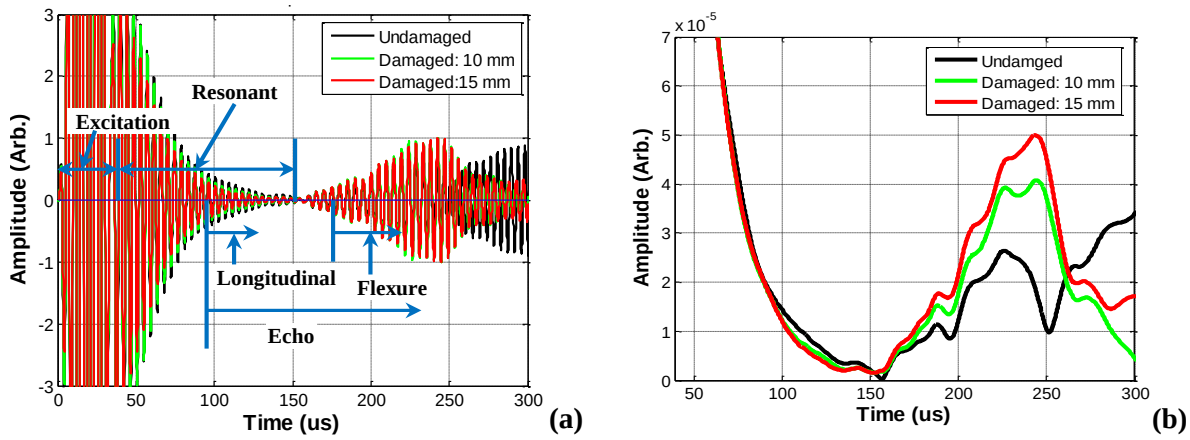

Figure 5.5 Time-domain pulse-echo signals extracted from the S_{11} parameter using an 8.5 cycle tone-burst signal centered at 220 kHz; (a) the pulse-echo signal contains the excitation, resonant, and echo signals; and (b) the amplitude envelopes of the time domain pulse-echo signals calculated using Hilbert-Huang transformation.

continued to produce an electric signal that decayed exponentially and died out at around 150 μs. The longitudinal wave echo should arrive after 89 μs. However, we did not observe any phase change around this time, indicating that the amplitude of the longitudinal mode echo signal was small and can thus be neglected. Based on the theoretical prediction, the flexural wave should arrive at 166 μs. However, the flexural wave arrived right after 150 μs because the 8.5 cycle 220 kHz tone-burst signal has frequency components up to 265 kHz, which has a higher group velocity and thus arrive earlier than the 220 kHz frequency component. The amplitudes of the time domain pulse-echo signals, calculated using the Hilbert-Huang transformation, are compared in Figure 5.5 (b). The lap joint delamination only had small influences on the resonant signals. In contrast, the amplitudes of the echo signals were influenced strongly by the delamination and increased monotonously as the delamination increased in length. In addition,

the arrival time of the "hump" between 200 μs to 250 μs appears to increase with the delamination length as well. This trend is consistent with the physics that the left edge of the lap joint shifted to the right as the delamination length increased, resulting in an increase in the round-trip distance traveled by the echo signal. It is, however, difficult to extract quantitative time information from Figure 5.5 (c) since the shape of the "hump" also changed with the delamination length.

The effects of the delamination on the S_{22} parameter are shown in Figure 5.6(a). Similar to the S_{11} parameter, the S_{22} parameter displays two resonances at 78 kHz and 220 kHz. However, the S_{22} parameter displays only a broadband resonance at 300 kHz, in contrast to the three resonances at above 300 kHz displayed by the S_{11} parameter. This difference is due to the slight difference in the adhesive thickness between the two PWaTs. As shown in Figure 5.6 (a), the amplitude of the 78 kHz resonance was not sensitive to the delamination. On the other hand, the 220 kHz resonance demonstrates a monotonic decrease of the return loss, albeit the changes were quite small. While the 300 kHz resonance was sensitive to the delamination, the return loss did not display a monotonic trend of change with respect to the delamination length. The time-frequency analysis of the S_{22} parameter yields similar results as those obtained from the S_{11} parameter and thus is not discussed here. The amplitude envelopes of the time-domain pulse-echo signal extracted from the S_{22} parameter using an 8.5 cycle tone-burst signal centered at 220 kHz are shown in Figure 5.6 (b). Compared to Figure 5.5 (b), the effect of the delamination on the time-domain pulse-echo signal extracted from the S_{22} parameter is much smaller. In addition, the shape and arrival time of the amplitude "hump" between 200 μs and 250 μs did not change much with the delamination. Based on this analysis, we can draw the conclusion that the

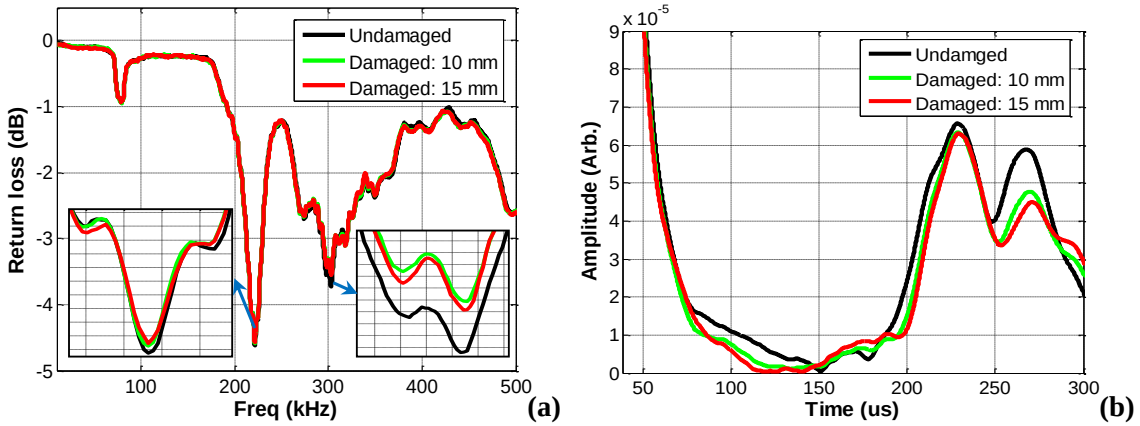

Figure 5.6 Effects of delamination on (a) S_{22} parameter; and (b) the amplitude envelopes of the time domain pulse-echo signals extracted from the S_{22} parameters using an 8.5 cycle 220 kHz tone-burst signal.

delamination was located at the side that is closer to PWaT #1, i.e. at the left side of the lap joint. In other words, acquiring the pulse-echo signals from both PWaTs enables us to determine at which side of the lap joint the damage was located.

5.5 Detecting damage severity using the transmission S_{21} parameter

The effects of the lap joint delamination on the transmission S_{21} parameter are shown in Figure 5.7. The S_{21} parameter at the 78 kHz resonance did not show a monotonic trend with the increase of the delamination length. On the other hand, the S_{21} parameter at the 220 kHz resonance reduced monotonously with the delamination length, which indicates that less ultrasound energy was transmitted from the bottom structure to the top structure and vice versa when the delamination length was increased. This explains why the reflection S_{11} parameter at this resonance increased monotonously with the delamination length. In contrast, the S_{21} parameters at the resonances above 250 kHz either increase or reduce with the delamination length and the

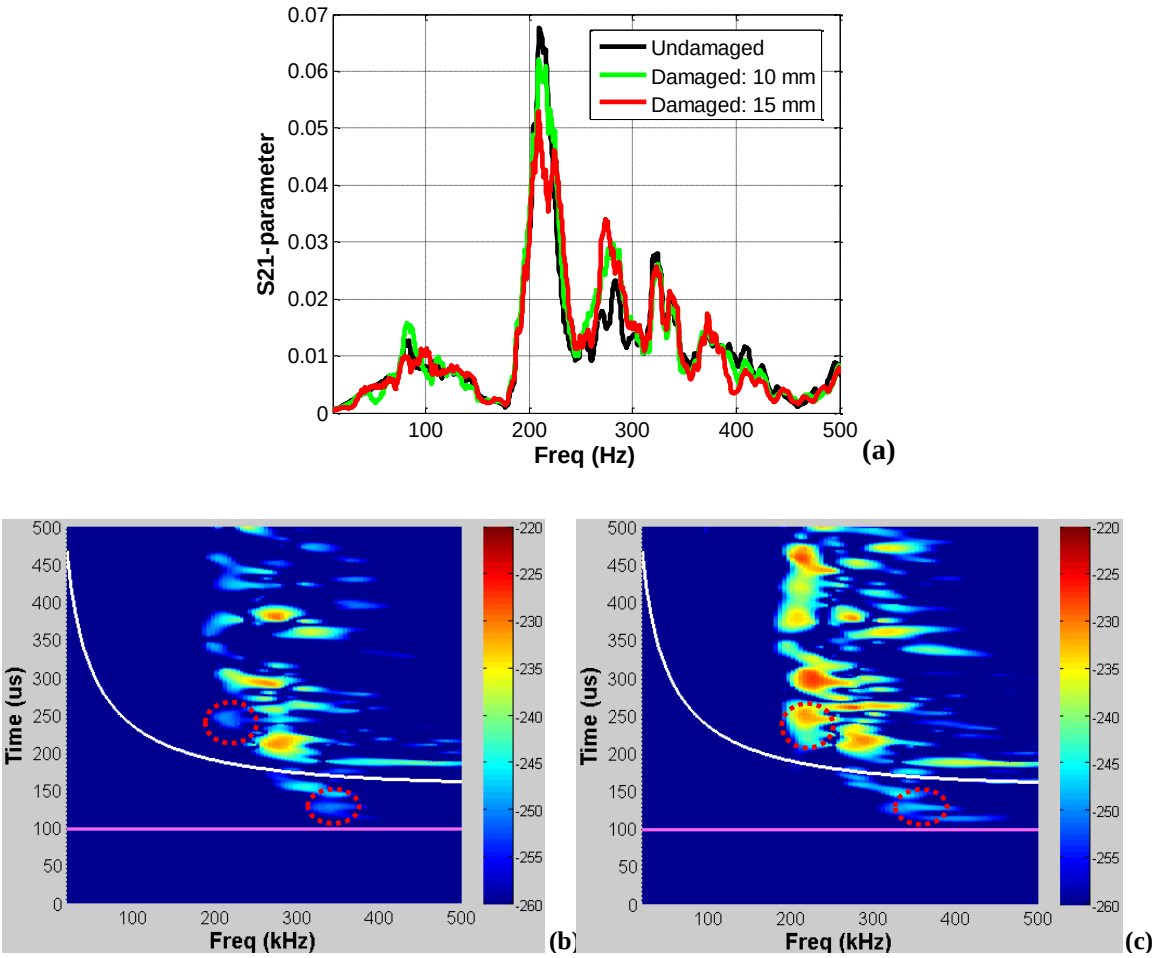

Figure 5.7 (a) Comparison of the S_{21} parameters before and after the introduction of delamination; (a) the amplitude difference of the time domain pitch-catch signal between the undamaged specimen and the specimen with a 10 mm delamination; and (c) the amplitude difference of the time domain pitch-catch signal between the undamaged specimen and the specimen with a 15 mm delamination.

changes were much smaller than that at the 220 kHz resonance. The TFA difference plots of the S_{21} parameters between the damaged and undamaged lap joints are shown in Figure 5.7 (b) and Figure 5.7 (c). The pitch-catch signal at the 78 kHz resonance is not as sensitive to the lap joint delamination as those at the other resonances. The amplitude difference of the first arrival pitch-

catch signal at the 220 kHz resonance, on the other hand, increased monotonously with the increase of the delamination length. For the resonance above 250 kHz, neither the amplitude differences of the longitudinal mode nor those of the flexural modes changed monotonously with the delamination length. We believe these non-monotonous behaviors of the pitch-catch signal are due to the effects of the delamination on the resonant characteristics of the PWaTs, which are also non-monotonous, as indicated by the resonant signals shown in Figure 5.4(b) and Figure 5.4(c). Therefore, only the pitch-catch signal at the resonance whose resonant signal is not sensitive to the delamination, e.g. the 220 kHz resonance, can provide reliable indication of the delamination severity. It is worth noting that the pitch-catch signal is directly governed by the resonance characteristics of the PWaTs but the effects of the delamination on the resonant characteristics of the PWaTs can only be evaluated from the pulse-echo signal. Therefore, correlating the S_{11} and S_{21} parameters not only provides the means to select the more suitable resonance for damage severity detection but also offers additional validations that improve the detection confidence.

5.6 Conclusions

In this paper, we demonstrated the application of the S-parameters for damage severity detection in a lap joint. Since the S-parameter represents the frequency response of a structure instrumented with two PWaTs, two time-domain Lamb wave signals, i.e. the pulse-echo and pitch-catch signals, can be calculated from the frequency domain S-parameters using a digital signal processing algorithm. Time-frequency analysis of the pulse-echo signal revealed that the resonant characteristics of the PWaTs at different resonances respond differently to the delamination and its progression. Only the resonance at which the PWaT resonant characteristics

are insensitive to the delamination is suitable for detecting the progression of the delamination. At this resonance, both the pulse-echo and pitch-catch signals display monotonous changes with the increase of the delamination length and these changes are consistent with the physics of how the Lamb wave interacts with the lap joint. Comparing the pulse-echo signals from both PWaTs facilitates determining at which side of the lap joint the delamination was located. In this study, we observed some phase shifts of the Lamb wave signal but was not able to draw any concrete conclusions.

CHAPTER 6

CONCLUDING REMARKS

6.1 Effects of adhesive thickness on the EMI signature and pitch-catch signal

The effects of the adhesive layer on the PWAS admittance and the pitch-catch signals were investigated experimentally and analytically. We demonstrated that the time-frequency analysis of the broadband ultrasound pitch-catch signal was very helpful in identifying the multi-modes structural vibrations as well as explaining some of the observed admittance features. Based on the derivation of the multi-mode analytical models, the effects of the adhesive layer are governed by two parameters, i.e. the shear transfer parameter and the thickness-shear modulus ratio. Since the adhesive thickness is constant, we adjusted the shear transfer parameter and the shear modulus of the adhesive in order to match the dominant resonance frequencies between the simulated and measured admittances. Therefore, the unknown shear modulus of the adhesive layer was estimated using this inverse technique. In addition, based on the simulated pitch-catch model, we predicted an optimized adhesive layer thickness at which the pitch-catch signal is optimum and validated the prediction using measurements.

6.2 Detecting damage of a composite lap joint using S-parameters

We implemented S-parameters for damage detection of a composite lap joint. The S-parameters were acquired over a wide frequency bandwidth using a compact instrument. We have demonstrated that small lap joint damage can be reliably detected based on the time-frequency analysis of the S-parameters. In addition, three different ultrasound signals, i.e. the pitch-catch, pulse-echo, and impedance signals, were simultaneously extracted from the S-parameters using

appropriate signal processing algorithm. The damage severity was also detected using the amplitude change of the pulse-echo and pitch-catch signal.

6.3 Detecting severity of delamination in an aluminum lap joint using S-parameters

The S-parameters were also used to detect the delamination severity of an aluminum lap joint. We discovered that the frequency at which the damage does not influence the amplitude of the resonant signal is the most suitable for detecting the damage severity. At such a frequency, the S-parameters as well as the amplitudes of the first arrival flexural mode echo signal and the flexural mode pitch-catch signal changed monotonously with the increase of the delamination length.

CHAPTER 7

FUTURE WORKS

7.1 Preliminary results

Up to this point, the lap joint delamination is detected using the amplitude change of the pitch-catch and pulse-echo signals. Since the amplitude of a signal may be influenced by many factors, we have explored an alternative method, i.e. phase shift, to detect the damage progression in a lap joint, which is known to provide a more robust damage index than the amplitude information. Figure 7.1 demonstrates the influence of the aluminum lap joint delamination on the phase shift of the pitch-catch signals. The time domain pitch-catch signal of the 220 kHz resonance extracted from the S_{21} parameters that were discussed in chapter 5 is shown in Figure 7.1(a). The inset in Figure 7.1(a) shows partially zoomed-in view of the pitch-catch signal with a time interval from 160 μs to 180 μs. We can see from this inset that the TOF of the pitch-catch signal increases with the increase of the lap joint delamination length. It is worth mentioned here that the Lamb wave group velocity is proportional to the stiffness of the structure (Rao 2007). We believe that the observed TOF increase indicates a reduction in the effective stiffness of the structure due to the delamination. Figure 7.1(b) presents the phase difference of the pitch-catch signals between the damaged and undamaged specimens versus the delamination length. Fitting the relationship with a linear trend line yields a R^2 value of 0.98. It is not clear why the phase shifts for the 12 mm and 20 mm delaminations have large deviations from the trend line. In order to understand how the delamination affects the phase of the Lamb wave signal, the analytical models developed in this work can be extended to simulate the propagation of the ultrasound

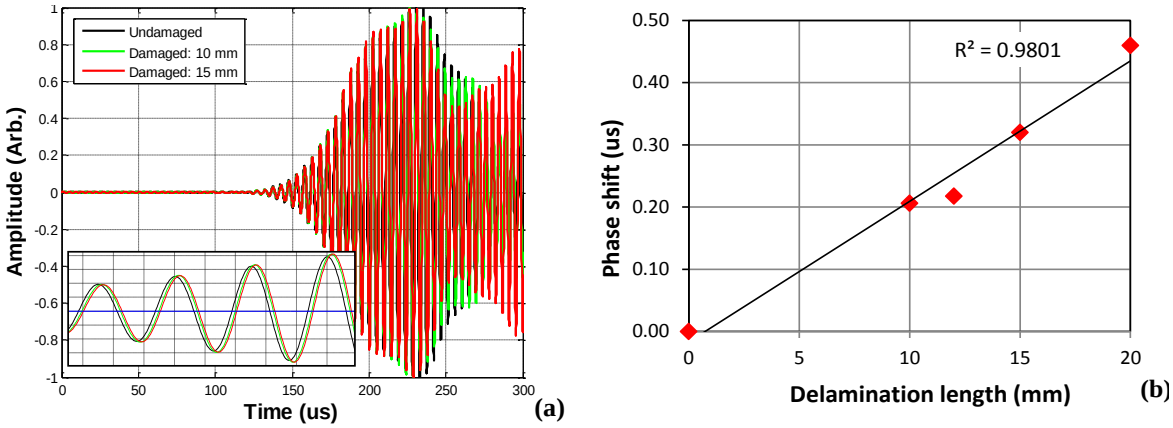

Figure 7.1 (a) Comparison of 220 kHz pitch-catch time domain signal between undamaged and damaged specimens; and (b) phase shift vs. the lap joint delamination length.

wave in lap joint structures. This simulation model may reveal the physics that explains the observed phenomena.

REFERENCES

Adams, R.D., Comyn, J. & Wake, W.C. 1997, *Structural adhesive joints in engineering*, Springer Science & Business Media.

Alleyne, D.N. & Cawley, P. 1992, "The interaction of Lamb waves with defects", *Ultrasonics, Ferroelectrics and Frequency Control, IEEE Transactions on*, vol. 39, no. 3, pp. 381-397.

Annamdas, V.G.M. & Soh, C.K. 2007, "Three-dimensional electromechanical impedance model. I: Formulation of directional sum impedance", *J. of Aero. Eng.*, vol. 20, pp. 53-62.

APC, C. 2015, "Product information catalogue", *Pennsylvania USA* *https://www.americanpiezo.com/apc-materials/physical-piezoelectric-properties.html*, .

Bhalla, S. & Soh, C.K. 2004, "Electromechanical impedance modeling for adhesively bonded piezo-transducers", *J. of. Intell. Mat. Sys. and Struct.*, vol. 15, pp. 955-971.

Bhuiyan, M.Y., Shen, Y. & Giurgiutiu, V. 2016, "Guided wave based crack detection in the rivet hole using global analytical with local fem approach", *Materials*, vol. 9, no. 7, pp. 602.

Campilho, R., De Moura, M. & Domingues, J. 2005, "Modelling single and double-lap repairs on composite materials", *Composites Science and Technology*, vol. 65, no. 13, pp. 1948-1958.

Cao, W., Zhu, S. & Jiang, B. 1998, "Analysis of shear modes in a piezoelectric vibrator", *Journal of Applied Physics*, vol. 83, no. 8, pp. 4415-4420.

Cawley, P. 1984, "The impedance method of non-destructive inspection", *NDT international*, vol. 17, no. 2, pp. 59-65.

Ceramic, P. 2003, "Product information catalogue: http://www.piceramic.de, Lindenstrasse, Germany", .

Christensen, R. 1982, *Theory of Viscoelasticity: an Introduction*, Second edition edn, Academic Press, Inc., New York, U.S.A.

Civjan, S., Margetis, P.M. & Reddick, R.L. 1969, "Properties of eta-butyl-alpha-cyanoacrylate mixtures", *Journal of dental research*, vol. 48, no. 4, pp. 536-542.

Crawley, E.F. & Lius, J.D. 1987, "Use of piezoelectric actuators as element of intelligent structures", *J. of AIAA*, vol. 25, pp. 1373-1382.

Crawley, E.F. & Anderson, E.H. 1990, "Detailed models of piezoceramic actuation of beams", *Journal of Intelligent Material Systems and Structures*, vol. 1, no. 1, pp. 4-25.

Crider II, J.S. 2007, *Damage detection using Lamb waves for structural health monitoring*, Air Force Institute of Technology.

Cuc, A. 2002, *Structural health monitoring of adhesively bonded joints with piezoelectric wafer active sensors*, University of South Carolina.

Cuc, A. & Giurgiutiu, V. 2004, "Disbond detection in adhesively bonded structures using piezoelectric wafer active sensors", *NDE for Health Monitoring and Diagnostics*International Society for Optics and Photonics, , pp. 66.

da Silva, Lucas Filipe Martins & Öchsner, A. 2008, *Modeling of adhesively bonded joints*, Springer.

Dalton, R., Cawley, P. & Lowe, M. 2001, "The potential of guided waves for monitoring large areas of metallic aircraft fuselage structure", *Journal of Nondestructive Evaluation*, vol. 20, no. 1, pp. 29-46.

Dugnani, R. 2009, "Dynamic behavior of structure-mounted disk-shape piezoelectric sensors including the adhesive layer", *Journal of Intelligent Material Systems and Structures*, vol. 20, no. 13, pp. 1553-1564.

Gao, H. 2007, *Ultrasonic guided wave mechanics for composite material structural health monitoring*, The Pennsylvania State University.

Giurgiutiu, V. 2008, *Structural Health Monitoring with Piezoelectric Wafer Active Sensors*, Elsevier, U.S.A.

Giurgiutiu, V. & Zagrai, A. 2005, "Damage detection in thin plates and aerospace structures with the electro-mechanical impedance method", *Sage Publications*, vol. 4, no. 2, pp. 99-120.

Giurgiutiu, V. 2005, "Tuned Lamb wave excitation and detection with piezoelectric wafer active sensors for structural health monitoring", *Journal of Intelligent Material Systems and Structures,* vol. 16, no. 4, pp. 291-305.

Giurgiutiu, V., Bao, J. & Zhao, W. 2003, "Piezoelectric wafer active sensor embedded ultrasonics in beams and plates", *Experimental Mechanics,* vol. 43, no. 4, pp. 428-449.

Giurgiutiu, V. & Cuc, A. 2005, "Embedded non-destructive evaluation for structural health monitoring, damage detection, and failure prevention", *Shock and Vibration Digest,* vol. 37, no. 2, pp. 83.

Giurgiutiu, V., Gresil, M., Lin, B., Cuc, A., Shen, Y. & Roman, C. 2012, "Predictive modeling of piezoelectric wafer active sensors interaction with high-frequency structural waves and vibration", *Acta Mechanica,* vol. 223, no. 8, pp. 1681-1691.

Giurgiutiu, V., Reynolds, A. & Rogers, C.A. 1999, "Experimental investigation of E/M impedance health monitoring for spot-welded structural joints", *Journal of Intelligent Material Systems and Structures,* vol. 10, no. 10, pp. 802-812.

Gresil, M., Yu, L., Giurgiutiu, V. & Sutton, M. 2012, "Predictive modeling of electromechanical impedance spectroscopy for composite materials", *Structural Health Monitoring,* vol. 11, no. 6, pp. 671-683.

Gulizzi, V., Rizzo, P. & Milazzo, A. 2015, "On the Repeatability of Electromechanical Impedance for Monitoring of Bonded Joints", *AIAA Journal,* vol. 53, no. 11, pp. 3479-3483.

Ha, S. & Chang, F. 2010, "Adhesive interface layer effects in PZT-induced Lamb wave propagation", *Smart Materials and Structures*, vol. 19, no. 2, pp. 025006.

Her, S. 1999a, "Stress analysis of adhesively-bonded lap joints", *Composite structures*, vol. 47, no. 1, pp. 673-678.

Her, S. 1999b, "Stress analysis of adhesively-bonded lap joints", *Composite structures*, vol. 47, no. 1, pp. 673-678.

Higgins, A. 2000, "Adhesive bonding of aircraft structures", *International Journal of Adhesion and Adhesives*, vol. 20, no. 5, pp. 367-376.

Howard, S.M. & Pao, Y.-. 1998a, "Analysis and experiments on stress waves in planar trusses", *J. Eng. Mech.*, vol. 124, pp. 884-891.

Howard, S.M. & Pao, Y. 1998b, "Analysis and experiments on stress waves in planar trusses", *Journal of Engineering Mechanics*, vol. 124, no. 8, pp. 884-891.

Huang, G., Song, F. & Wang, X. 2010, "Quantitative modeling of coupled piezo-elastodynamic behavior of piezoelectric actuators bonded to an elastic medium for structural health monitoring: A review", *Sensors*, vol. 10, no. 4, pp. 3681-3702.

Huang, H., Pamphile, T. & Derriso, M. 2008, "The effect of actuator bending on Lamb wave displacement fields generated by a piezoelectric patch", *Smart Materials and Structures*, vol. 17, no. 5, pp. 055012.

Huang, H. & Bednorz, T. 2014, "Introducing S-parameters for ultrasound-based structural health monitoring", *Ultrasonics, Ferroelectrics, and Frequency Control, IEEE Transactions on*, vol. 61, no. 11, pp. 1856-1863.

Ihn, J. & Chang, F. 2002, "Multicrack growth monitoring at riveted lap joints using piezoelectric patches", *NDE For Health Monitoring and Diagnostics*International Society for Optics and Photonics, Sand diego, CA, March 17,2002, pp. 29.

Ikeda, T. 1990, *Fundamentals of Piezoelectricity*, Oxford University Press, U.S.A.

Islam, M.M. & Huang, H. 2015, "S-parameters for ultrasound inspection of composite lap joints", *Society for the Advancement of Material and Process Engineering*Society for the Advancement of Material and Process Engineering, Baltimore, MD, USA, 18 May 2015 through 21 May 2015, pp. Volume 2015-January, 2015.

Islam, M.M. & Huang, H. 2014a, "Effects of adhesive thickness on the Lamb wave generation and sensing using bonded PWASs", *SPIE proceedings*In press, March 09- March 13.

Islam, M. & Huang, H. 2016, "Effects of adhesive thickness on the Lamb wave pitch-catch signal using bonded piezoelectric wafer transducers", *Smart Materials and Structures*, vol. 25, no. 8, pp. 085014.

Islam, M. & Huang, H. 2014b, "Understanding the effects of adhesive layer on the electromechanical impedance (EMI) of bonded piezoelectric wafer transducer", *Smart Materials and Structures*, vol. 23, no. 12, pp. 125037.

Jin, C., Wang, X. & Zuo, M. 2009, "The dynamic behaviour of surface-bonded piezoelectric actuators with debonded adhesive layers", *Acta Mechanica*, vol. 211, no. 3-4, pp. 215-235.

Jin, C. & Wang, X. 2011, "The effect of adhesive layers on the dynamic behavior of surface-bonded piezoelectric sensors with debonding", *Journal of Intelligent Material Systems and Structures*, vol. 22, pp. 655-70.

Lamb, H. 1917, "On waves in an elastic plate", *Proceedings of the Royal Society of London.Series A*, vol. 93, no. 648, pp. 114-128.

Lee, B. & Staszewski, W. 2003, "Modelling of Lamb waves for damage detection in metallic structures: Part II. Wave interactions with damage", *Smart Materials and Structures*, vol. 12, no. 5, pp. 815.

Lee, P., Liu, N. & Ballato, A. 1999, "Thickness vibrations of piezoelectric plates with dissipation", *Proceedings on IEEE Ultrasonics Symposium*IEEE, , pp. 869-871.

Liang, C., Sun, F.P. & Rogers, C.A. 1994, "Coupled electro-mechanical analysis of adaptive material systems-Determination of the actuator power consumption and system energy transfer", *Cent. for Intell. Mat. Sys. and Struct.*, vol. 5, pp. 12-20.

Lim, Y.Y. & Soh, C.K. 2014, "Towards more accurate numerical modeling of impedance based high frequency harmonic vibration", *Smart Materials and Structures*, vol. 23, no. 3, pp. 035017.

Lin, M.W. & Rogers, C.A. 1994, "Bonding layer effects on the actuation mechanism of an induced strain actuator/substructure system", *SPIE,* vol. 2190, pp. 658-670.

Liu, W. & Giurgiutiu, V. 2011, "Finite element modeling and simulation of piezoelectric wafer active sensors interaction with the host structure for structural health monitoring", *Proc. SPIE 6174*, pp. 6174Z-1-12.

Loveday, P.W., Long, C.S. & Burger, F.A. 2013, "Long Range Guided Wave Monitoring of Rail Track", *to appear in Review of Progress in Quantitative Nondestructive Evaluation, .*

Lowe, M. & Cawley, P. 1994, "The applicability of plate wave techniques for the inspection of adhesive and diffusion bonded joints", *Journal of Nondestructive Evaluation,* vol. 13, no. 4, pp. 185-200.

Lowe, M., Challis, R. & Chan, C. 2000, "The transmission of Lamb waves across adhesively bonded lap joints", *The Journal of the Acoustical Society of America,* vol. 107, no. 3, pp. 1333-1345.

Makkonen, T., Holappa, A., Ella, J. & Salomea, M. 2001, "Finite element simulations of thin-film composite BAW resonators", *Ultrasonics, Ferroelectrics and Frequency Control, IEEE Transactions on,* vol. 48, no. 5, pp. 1241-1258.

Mal, A.K., Chang, Z., Guo, D. & Gorman, M. 1996, "Lap-joint inspection using plate waves", *Nondestructive Evaluation Techniques for Aging Infrastructure and Manufacturing*International Society for Optics and Photonics, , pp. 128.

Matt, H., Bartoli, I. & Lanza di Scalea, F. 2005, "Ultrasonic guided wave monitoring of composite wing skin-to-spar bonded joints in aerospace structures", *The Journal of the Acoustical Society of America,* vol. 118, no. 4, pp. 2240-2252.

Metzinger, K. & Guess, T. 1996, "Analysis and testing of adhesively bonded lap joints", *Wind Energy: Energy Week,* , pp. 52.

Moharana, S. & Bhalla, S. 2012, "Numerical investigations of shear lag effect on PZT-structure interaction: review and application", *Current Science(Bangalore),* vol. 103, no. 6, pp. 685-696.

Moser, F., Jacobs, L.J. & Qu, J. 1999, "Modeling elastic wave propagation in waveguides with the finite element method", *NDT & E International,* vol. 32, no. 4, pp. 225-234.

Nguyen, C., Pietrzko, S. & Buetikofer, R. 2004, "The influence of temperature and bonding thickness on the actuation of a cantilever beam by PZT patches", *Smart Materials and Structures,* vol. 13, no. 4, pp. 851.

Oppenheim, A.V., Schafer, R.W. & Buck, J.R. 1989, *Discrete-time Signal Processing,* 3rd edn, Prentice-hall Englewood Cliffs, New Jersey, USA.

Pao, Y., Keh, D. & Howard, S.M. 1999, "Dynamic response and wave propagation in plane trusses and frames", *AIAA Journal,* vol. 37, no. 5, pp. 594-603.

Park, C., Walz, C. & Chopra, I. 1996, "Bending and torsion models of beams with induced-strain actuators", *Smart Materials and Structures,* vol. 5, no. 1, pp. 98.

Park, G. & Inman, D.J. 2007, "Structural health monitoring using piezoelectric impedance measurements", *Phil. Trans. R. Soc.*, vol. 365, pp. 373-392.

Park, G., Sohn, H., Farrar, C.R. & Inman, D.J. 2003, "Overview of piezoelectric impedance-based health monitoring and path forward", *The shock and vibration digest*, vol. 35, pp. 451-463.

Park, G., Farrar, C.R., di Scalea, F.L. & Coccia, S. 2006, "Performance assessment and validation of piezoelectric active-sensors in structural health monitoring", *Smart Materials and Structures*, vol. 15, no. 6, pp. 1673.

Park, S., Yun, C. & Inman, D. 2008, "Structural health monitoring using electro- mechanical impedance sensors", *Fatigue & Fracture of Engineering Materials & Structures*, vol. 31, no. 8, pp. 714-724.

PI Ceramic 2003, "Product information catalogue", *Lindenstrasse Germany* *http://www.piceramic.de*, .

Puthillath, P.K., Yan, F., Kannajosyula, H., Lissenden, C.J., Rose, J.L. & Xu, C. 2008, "Inspection of Adhesively Bonded Joints Using Ultrasonic Guided Waves", *17th World Conference on Nondestructive Testing*,Citeseer, Shanghai, China, Oct 25-28.

Qing, X.P., Chan, H., Beard, S.J., Ooi, T.K. & Marotta, S.A. 2006, "Effect of adhesive on the performance of piezoelectric elements used to monitor structural health", *International Journal of Adhesion and Adhesives*, vol. 26, no. 8, pp. 622-628.

Quaegebeur, N., Micheau, P., Masson, P. & Castaings, M. 2012, "Methodology for optimal configuration in structural health monitoring of composite bonded joints", *Smart Materials and Structures,* vol. 21, no. 10, pp. 105001.

Rabinovitch, O. & Vinson, J.R. 2002, "Adhesive layer effects in surface-mounted piezoelectric actuators", *Journal of Intelligent Material Systems and Structures,* vol. 13, no. 11, pp. 689-704.

Raghavan, A. & Cesnik, C.E. 2007, "Review of guided-wave structural health monitoring", *Shock and Vibration Digest,* vol. 39, no. 2, pp. 91-116.

Rao, S.S. 2007, *Vibration of Continuous System,* John Willey and Sons, Inc., U.S.A.

Ritdumrongkul, S., Abe, M., Fujino, Y. & Miyashita, T. 2003, "Quantitative health monitoring of bolted joints using a piezoceramic actuator–sensor", *Smart Materials and Structures,* vol. 13, no. 1, pp. 20.

Rus, G., Wooh, S. & Gallego, R. 2004, "Analysis and design of wedge transducers using the boundary element method", *The Journal of the Acoustical Society of America,* vol. 115, pp. 2919.

Sadek, M.M. 1987, *Industrial Applications of Adhesive Bonding,* Springer, London and New York.

Santoni-Bottai, G. & Giurgiutiu, V. 2012, "Exact shear-lag solution for guided waves tuning with piezoelectric-wafer active sensors", *AIAA Journal,* vol. 50, no. 11, pp. 2285-2294.

Shen, Y. & Giurgiutiu, V. 2014, "Predictive modeling of nonlinear wave propagation for structural health monitoring with piezoelectric wafer active sensors", *Journal of Intelligent Material Systems and Structures*, pp. 506-520.

Sirohi, J. & Chopra, I. 2000, "Fundamental understanding of piezoelectric strain sensors", *Journal of Intelligent Material Systems and Structures*, [Online], vol. 11, no. 4, pp. 246-257.

Song, F., Huang, G. & Hu, G. 2012, "Online guided wave-based debonding detection in honeycomb sandwich structures", *AIAA Journal*, vol. 50, no. 2, pp. 284-293.

Song, W., Rose, J.L., Galan, J.M. & Abascal, R. 2003, "Transmission and reflection of AO mode Lamb wave in a plate overlap", *Review of progress in quantitative nondestructive evaluation*, vol. 22, pp. 1088-1094.

Su, Z., Ye, L. & Lu, Y. 2006, "Guided Lamb waves for identification of damage in composite structures: A review", *Journal of Sound and Vibration*, vol. 295, no. 3, pp. 753-780.

Tinoco, H.A. & Serpa, A.L. 2011, "Bonding influence in the electromechanical (EM) admittance of piezoelectric sensors bonded to structures based on EMI technique", *Proc. of the XIV Int. Symp. on Dyn. Prob. of Mech.*, pp. 1-10.

V. Giurgiutiu 2007, *Structural Health Monitoring with Piezoelectric Wafer Active Sensors*, NY: academic, New York.

Viktorov, I.A. 1967, *Rayleigh and Lamb waves: physical theory and applications*, Plenum press, New York.

Willberg, C., Duczek, S. & Gabbert, U. 2013, "Increasing the scanning range of Lamb wave based SHM systems by optimizing the actuator–sensor design", *CEAS Aeronautical Journal,* , pp. 1-12.

Worlton, D. 1956, "Ultrasonic testing with Lamb waves", *Non-Destructive Testing*, vol. 15, pp. 218-222.

Wu, Z., Qing, X.P., Ghosh, K., Karbhar, V. & Chang, F. 2008, "Health monitoring of bonded composite repair in bridge rehabilitation", *Smart Materials and Structures*, vol. 17, no. 4, pp. 045014.

Xu, Y.G. & Liu, G.R. 2002, "A modified electro-mechanical impedance model of piezoelectric actuator-sensors for debonding detection of composite patches", *J. of. Intell. Mat. Sys. and Struct.,* vol. 13, no. 6, pp. 389-396.

Yamada, K., Sakamura, J. & Nakamura, K. 2001, "Equivalent network representation for thickness vibration modes in piezoelectric plates with a linearly graded parameter", *IEEE,* vol. 48, no. 2, pp. 613-616.

Yan, W., Lim, C.W., Cai, J.B. & Chen, W.Q. 2007, "An electromechanical impedance approach for quantitative damage detection in Timoshenko beams with piezoelectric patches", *Smart Materials and Structures*, vol. 16, pp. 1390-1400.

Yang, M. & Qiao, P. 2005, "Modeling and experimental detection of damage in various materials using the pulse-echo method and piezoelectric sensors/actuators", *Smart Materials and Structures*, vol. 14, no. 6, pp. 1083.

Yang, Y., Lim, Y.Y. & Soh, C.K. 2008a, "Practical issues related to the application of the electromechanical impedance technique in the structural health monitoring of civil structures:II. Numerical verification", *Smart mat. and struct.*, vol. 17, pp. 035009 (12pp).

Yang, Y., Lim, Y.Y. & Soh, C.K. 2008b, "Practical issues related to the application of the electromechanical impedance technique in the structural health monitoring of civil structures: I. Experiment", *Smart Materials and Structures*, vol. 17, no. 3, pp. 035008.

Yu, L., Giurgiutiu, V., Wang, J. & Shin, Y. 2012, "Corrosion detection with piezoelectric wafer active sensors using pitch-catch waves and cross-time–frequency analysis", *Structural Health Monitoring*, vol. 11, no. 1, pp. 83-93.

Zahedi, F. & Huang, H. 2017, "Time–frequency analysis of electro-mechanical impedance (EMI) signature for physics-based damage detections using piezoelectric wafer active sensor (PWAS)", *Smart Materials and Structures*, vol. 26, no. 5, pp. 055010.

Zhang, Y., Xu, F., Chen, J., Wu, C. & Wen, D. 2011, "Electromechanical impedance response of a cracked timoshenko beam", *Sensors*, vol. 11, no. 7, pp. 7285-7301.

APPENDIX A

DERIVATION OF PULSE-ECHO AND PITCH-CATCH SIGNAL FROM S-PARAMETERS

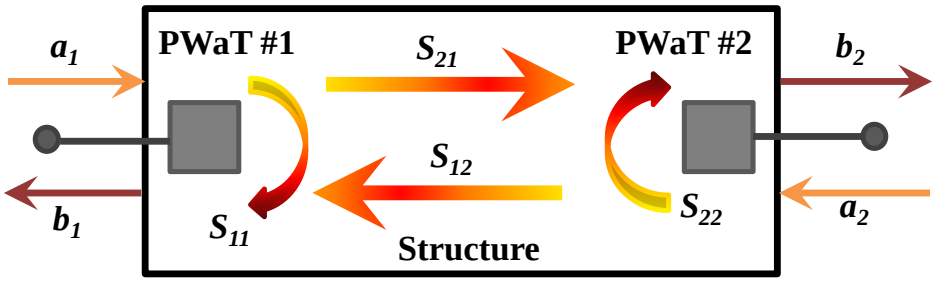

Figure A.1. *S*-parameter representation of a two port ultrasound-based structural health

The representation of the *S*-parameters for a structure instrumented with two PWaTs is shown in figure A.1. Treating such a system as a two-port linear time-invariant network, the S_{11} and S_{21} parameters can be expressed as functions of the network inputs and outputs as

$$S_{11} = \left.\frac{b_1}{a_1}\right|_{a_2 = 0} \quad \text{and} \quad S_{21} = \left.\frac{b_2}{a_1}\right|_{a_2 = 0}, \tag{A.1}$$

where a_1 and a_2 are the input signals at port #1 and #2, respectively; b_1, and b_2 are the output signals at port #1 and #2, respectively. If there is no input signal at port #2, i.e. $a_2 = 0$, b_1 is the signal reflected at port #1 and b_2 is the signal transmitted from port #1 to #2. Similarly, the S_{22} and S_{12} parameters can be defined as

$$S_{22} = \left.\frac{b_2}{a_2}\right|_{a_1 = 0} \quad \text{and} \quad S_{12} = \left.\frac{b_1}{a_2}\right|_{a_1 = 0}, \tag{A.2}$$

where b_2 is the signal reflected at port #2 and b_1 is the signal transmitted from port #2 to #1, assuming there is no input at port #1. If the inputs at both ports are not zero, the outputs of the network can be calculated from the port inputs as

$$\begin{bmatrix} b_1 \\ b_2 \end{bmatrix} = \mathbf{S} \times \begin{bmatrix} a_1 \\ a_2 \end{bmatrix}, \quad \mathbf{S} = \begin{bmatrix} S_{11} & S_{12} \\ S_{21} & S_{22} \end{bmatrix}. \tag{A.3}$$

Among the four *S*-parameter components, the S_{11} and S_{22} parameters are called the reflection *S*-parameters while $S_{21} = S_{12}$ are the transmission *S*-parameters. Acquired in the frequency domain using a VNA, the *S*-parameters represent the frequency response of the network within the measured frequency bandwidth. In our case, the S_{11} and S_{22} parameters are the frequency domain pulse-echo responses of PWaT #1 and PWaT #2, respectively. Similarly, the S_{21} parameter is the frequency domain pitch-catch response of the system when PWaT #1 is the actuator and PWaT #2 is the sensor. Reversing the roles of these two transducers produces the S_{12} parameter.

The time domain pulse-echo or pitch-catch signals, i.e. the output signal, can be calculated from the measured S-parameters and a given excitation signal (i.e. the input signal) following the procedure depicted in figure A.2. First, The spectrum of the output signal can be computed by multiplying the corresponding *S*-parameters with the spectrum of the excitation signal *I(f)* as

$$O(f) = S_{ij}(f) * I(f), \tag{A.4}$$

in which *ij = 11* and *22* produces the pulse-echo signal at PWaT #1 and #2, respectively while *ij*

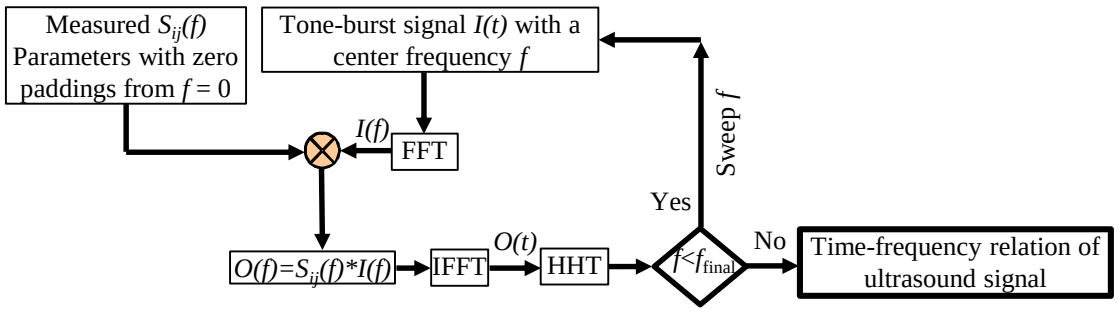

Figure A.2. Flow diagram of digital signal processing algorithm for time-frequency analysis of S-parameters.

= *21* or *12* produces the pitch-catch signal. *f* is the center frequency of the excitation signal. The Inverse Fast Fourier Transformation of this frequency domain output signal, therefore, results in the time domain output signal, i.e.

$$O(t) = IFFT\ [O(f)] = IFFT\ [S_{ij}(f) * I(f)]. \tag{A.5}$$

Furthermore, the time-frequency-amplitude relationship of the output signal can be obtained by sweeping the center frequency of the excitation signal *f* and calculating the envelope of the time-domain output signals using the Hilbert-Huang Transformation.

A typical pulse-echo signal calculated from the S_{11} or S_{22} parameters is shown in figure A.3. Based on the physical mechanism that generates the electric signal, the pulse-echo signal can be divided into three signals, namely the excitation, resonant, and echo signal. The excitation signal occupies the time span when an external voltage is applied to the PWaT terminal and thus is dominated by the supplied voltage. Due to the piezoelectric effect, the PWaT deforms accordingly, generating the Lamb wave that propagates in the structure. After the removal of the external voltage, the PWaT continues to oscillate and produces electric current if the excitation frequency is close to its resonant frequency. Therefore, the portion of the pulse-echo signal right after the end of excitation signal is contributed by the resonating PWaT and thus is directly correlated to the resonant characteristics of the PWaT. This resonant signal can last for a long time or die out quickly, depending on the bandwidth of the PWaT resonance and the proximity of the excitation frequency to the PWaT resonance frequency. At the meantime, the Lamb wave generated by the excitation signal is propagating in the structure. Structural discontinuities such as cracks, delaminations, boundaries, etc. can reflect the Lamb wave back to the PWaT, which in

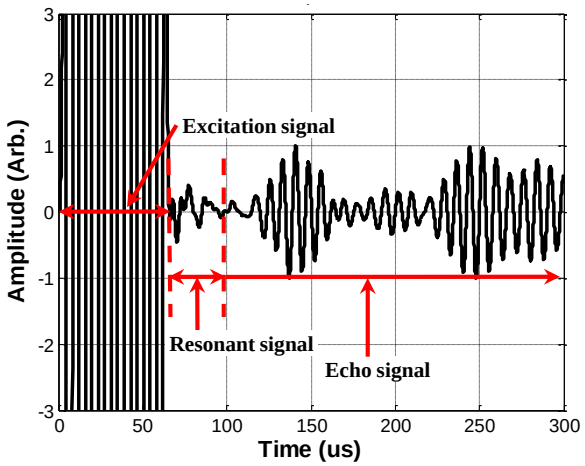

Figure A.3. A typical pulse-echo signal containing three signals, i.e. the excitation, resonant, and echo signals. The excitation signal is dominated by the supplied voltage; the resonant signal reflects the resonant characteristics of the piezoelectric wafer active transducer; and the echo turn generates the echo signal. Depending on the location of the discontinuity, the echo signal could overlap with the resonant signal, which makes detecting the arrival of the echo signal difficult. If we know the wave speed and the distance between the location of the first discontinuity and the PWaT, however, the echo signal can be identified based on the calculated time of arrival. Correspondingly, the first arrival of the pitch-catch signal is contributed by the lamb wave generated by the excitation signal. Traveling from the actuator to the sensor, this Lamb wave is influenced by any damage between these two transducers and thus is the most frequently used for damage detection. The pitch-catch signal after the first arrival has contribution from the Lamb wave generated by the resonating PWaT as well as the Lamb waves reflected or deflected by structural discontinuities. Therefore, it may be influenced by the resonant characteristics of the PWaT as well as any structural discontinuity.

For more detailed discussions on the S-parameters and their relationship to the time-domain pulse-echo and pitch-catch signals, the readers should refer to the published papers ((Huang, Bednorz 2014) and (Zahedi and Huang 2017))